Development of an IH-Type Linac for the Acceleration of High Current Heavy Ion Beams

Dissertation

zur Erlangung des Doktorgrades

der Naturwissenschaften

vorgelegt beim Fachbereich Physik

der Johann Wolfgang Goethe-Universität

in Frankfurt am Main

von

Jan Hendrik Hähnel

aus Heide (Holst.)

Frankfurt am Main 2017

D 30

Vom Fachbereich Physik der
Johann Wolfgang Goethe-Universität als Dissertation angenommen.

Dekan: Prof. Dr. Owe Philipsen
Erster Gutachter: Prof. Dr. Ulrich Ratzinger
Zweiter Gutachter: Prof. Dr. Joachim Jacoby
Datum der Disputation: 20.07.2017

Zusammenfassung

Diese Arbeit befasst sich mit der Entwicklung von Linearbeschleunigern für Schwerionen. Insbesondere werden in dieser Arbeit zwei Abschnitte des GSI Schwerionenbeschleunigers UNILAC neu entworfen um höhere Ionenströme beschleunigen zu können. In Darmstadt wird derzeit an der GSI ein neuer Beschleunigerkomplex FAIR zur Forschung mit Antiprotonen und Ionen gebaut. FAIR soll bisher unerreichte Strahlintensitäten von Antiprotonen, Protonen und Ionen bis Uran für eine Vielzahl von Experimenten zur Verfügung stellen. Um diese hohen Strahlintensitäten zu erreichen, muss der UNILAC als Injektor für das SIS18 Synchrotron einen Strom von 15 emA U^{28+} in ca. 100 µs langen Pulsen bereitstellen. Die so erreichbare Anzahl von Uranionen im SIS18 beträgt $2.7 \cdot 10^{11}$ [1]. Nach der Beschleunigung im SIS18 werden die Ionen in das neue SIS100 injiziert, um Energien von bis zu 29 GeV für Protonen und 2.7 $\frac{\text{GeV}}{\text{u}}$ für U^{28+} zu erreichen. Der bestehende UNILAC (Abbildung 0.1) kann die benötigten Ströme für FAIR ohne Aufrüstungsmaßnahmen nicht bereitstellen.

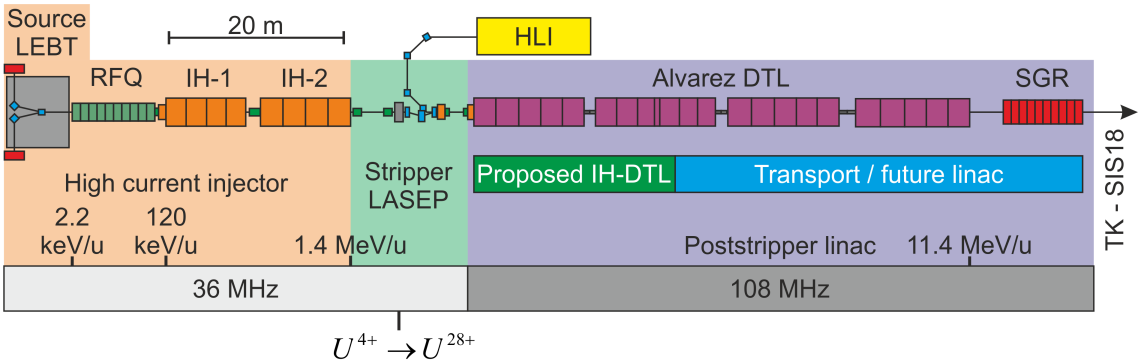

Abbildung 0.1: Schematische Darstellung des bestehenden UNILAC. Die Längenverhältnisse des neuen vorgeschlagenen Poststripper Beschleunigers und des dadurch entstehenden Freiraumes sind grün und hellblau dargestellt.

Ein Teil dieser Arbeit befasst sich mit dem Entwurf einer neuen Anpassungsstrecke MEBT für den Hochstrominjektor HSI des UNILAC (siehe Abbildung 0.2).

Die bestehende MEBT setzt sich zusammen aus einer magnetischen Quadrupol-Doublettlinse und einer sogenannten Superlinse. Die Superlinse ist ein kurzer 11-Zellen RFQ (Radiofrequenz-Quadrupol Beschleuniger), der als Buncher und als transversale Linse betrieben wird. Nach einem Upgrade der RFQ Elektroden des HSI im Jahr 2009 haben sich geänderte Strahlparameter am Ausgang des RFQ ergeben [2]. Vor allem die höhere Strahldivergenz am Ausgang des RFQ führt dazu, dass der Strahl im Falle des Hochstrombetriebs mit Uran teilweise an den Elektroden der Superlinse verloren geht, weil die Apertur nicht groß genug ist. Dies liegt daran, dass die MEBT mit der Superlinse für den ursprünglichen RFQ des HSI ausgelegt wurde [3] und nicht mehr ausreicht, um die erhöhte Strahldivergenz zu kompensieren.

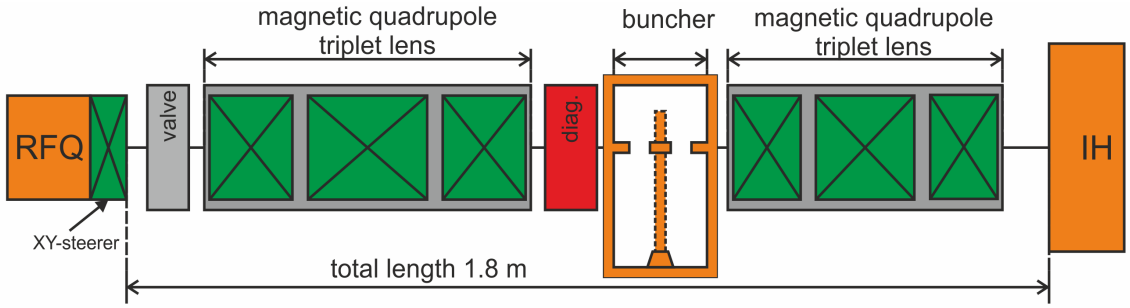

Abbildung 0.2: Schematische Darstellung der vorgeschlagenen MEBT Anpassungsstrecke für den HSI.

Die neue MEBT Sektion besteht aus zwei Quadrupol-Triplettlinsen und einer Buncher Kavität (siehe Abb. 0.2) [4]. Die Anordnung und Dimensionierung der Linsen und des Bunchers sind so optimiert, dass eine optimale Anpassung des Strahls an die IH-Struktur (Interdigitale H-Moden Struktur) gewährleistet ist. Simulationen mit der Teilchenverteilung am Ausgang des RFQ ab 2009 zeigen deutlich die Vorteile der neuen MEBT Sektion. Die Rechnungen wurden für einen Strahlstrom von 20.75 emA U^{4+} durchgeführt. Mit der neuen Anpassungsstrecke, kann die Transmission der MEBT Sektion von 90.45 % auf 99.99 % erhöht werden. Daraus resultiert eine Verbesserung der Gesamttransmission vom Beginn der MEBT-Sektion bis zum Ende des zweiten IH-Tanks von 87.6 % auf 99.39 %, wobei die verbleibenden Verluste ausschließlich auf Teilchen der RFQ Teilchenverteilung zurückzuführen sind, die deutlich weiter vom Strahlzentrum entfernt sind als die meisten Teilchen. Das Emittanzwachstum in der neuen MEBT Sektion ist kleiner als 8 % transversal und kleiner als 5 % longitudinal. Durch die optimierte Anpassung des Strahls an die IH-Struktur

kann das Emittanzwachstum der beiden IH-Tanks einschließlich der MEBT Sektion in der horizontalen Ebene von 173.4 % auf 77.6 %, in der vertikalen Ebene von 129.4 % auf 95.6 % und in der longitudinalen Ebene von 321.5 % auf 56.1 % gesenkt werden. Die erreichte horizontale Brillanz des HSI kann so mit der neuen MEBT Sektion nahezu verdoppelt werden (+93 %). Dies zeigt deutlich die Notwendigkeit einer neuen MEBT Sektion, um einen Hochstrombetrieb des UNILAC in Zukunft sicherzustellen.

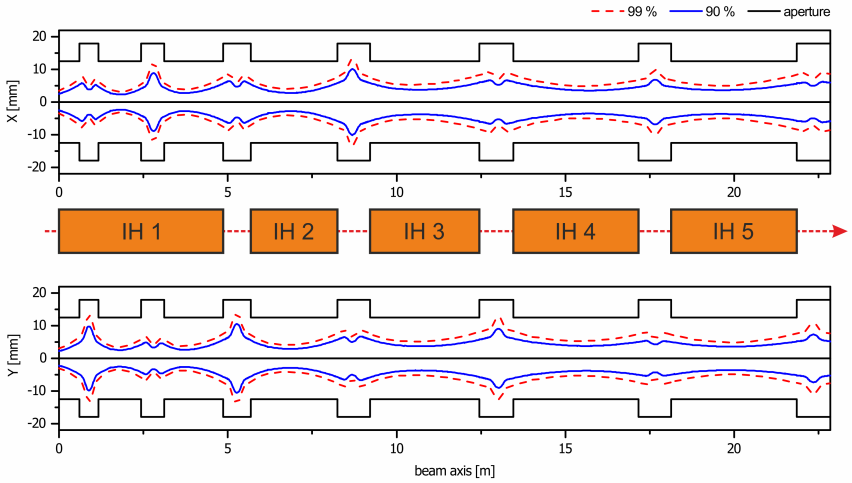

Abbildung 0.3: Transversale Strahlenveloppen des entwickelten Poststripper Linearbeschleunigers.

Der Hauptteil dieser Arbeit befasst sich mit der Entwicklung eines Linearbeschleunigers für den sogenannten Poststripper Abschnitt des UNILAC. Nachdem der U^{4+} Strahl im HSI auf 1.4 $\frac{\text{MeV}}{\text{u}}$ beschleunigt wurde, werden die Ionen in einem Gasstripper auf den Ladungszustand 28+ gebracht um eine effiziente Weiterbeschleunigung zu ermöglichen. Der U^{28+} Strahl wird dann im Poststripper Beschleuniger von 1.4 $\frac{\text{MeV}}{\text{u}}$ auf 11.4 $\frac{\text{MeV}}{\text{u}}$ beschleunigt, was 15.5 % Lichtgeschwindigkeit entspricht. Bei dieser Energie wird der Strahl in das SIS18 injiziert. Der bestehende Poststripper Beschleuniger ist ein Alvarez DTL. Die ersten beiden Alvarez Tanks des UNILAC wurden in den Siebziger Jahren gebaut. Die Tanks drei und vier in den Achtziger Jahren. Bedingt durch das hohe Alter der Alvarez Tanks kommt es vermehrt zu Ausfällen durch Wasserlecks, Vakuumlecks und Kurzschlüsse in den internen Quadrupollinsen. Zusätzlich gibt es Probleme mit Oxidation in den Kühlkanälen. Aus diesen Gründen kann ein stabiler ausfallsicherer Betrieb des UNILAC als FAIR Injektor mit dem bestehenden Poststripper Beschleuniger nicht gewährleistet werden. Ein

Austausch des Alvarez DTL ist somit notwendig. In dieser Arbeit wurde ein Linearbeschleuniger für den Poststripper Abschnitt entwickelt, der auf fünf IH-Strukturen mit Triplettfokussierung und der KONUS Strahldynamik basiert [5].

Durch die Verwendung von effizienten IH-Strukturen bei 108.408 MHz konnte die Länge des Poststripper Beschleunigers von etwa 60 m auf nur 23 m bei gleicher Endenergie reduziert werden. Die KONUS Strahldynamik [6, 7] erlaubt eine hohe Beschleunigungseffizienz und ermöglicht die Verwendung langer IH-Strukturen mit wenigen Fokussierelementen. Die Auslegung und Simulation der Strahldynamik wurde mit dem Simulationscode LORASR[1] durchgeführt, der am IAP Frankfurt ständig weiterentwickelt wird. Die Strahldynamik wurde für die Beschleunigung von Hochstrom-Ionenstrahlen bei möglichst geringem Emittanzwachstum optimiert. Die longitudinale Strahldynamik konnte durch die Anpassung der einzelnen KONUS Abschnitte zueinander optimiert werden, sodass ein longitudinales Emittanzwachstum von 11.1 % erreicht werden konnte. Die transversale Strahlführung mit Quadrupol-Triplettlinsen wurde auf einen optimierten konstanten Phasenvorschub eingestellt. Dadurch konnte ein transversales Emittanzwachstum von weniger als 30 % für einen Strahlstrom von 15 emA U^{28+} erreicht werden. Nach der Optimierung der Strahldynamik wurde diese mit einem zweiten Simulationscode (TraceWin[2]) verifiziert. Um die Stabilität des Designs im Hinblick auf mögliche Justierfehler der Linsen und Kavitäten, Fehler der Feldamplituden und -phasen, sowie Fehler bei der Injektion des Strahls zu untersuchen, wurden umfangreiche Fehlerstudien durchgeführt. Hierfür wurden zuerst die Einflüsse einzelner Fehlertypen untersucht und Grenzwerte definiert. Auf Basis dieser Grenzwerte wurden dann Fehlerstudien mit gleichzeitiger Anwesenheit aller Fehlertypen durchgeführt. Desweiteren wurden verschiedene Strategien zur Strahlsteuerung mit sogenannten Steerern untersucht, um die notwendige Anzahl und Anordnung solcher korrektiven Elemente zu bestimmen. Die Ergebnisse zeigen, dass das entwickelte Beschleunigerkonzept innerhalb technisch machbarer Toleranzen nur eine geringe Abweichung vom Optimalbetrieb aufweist. Mit dem richtigen Steering-Konzept können zudem große Fehlertoleranzen kompensiert werden, was zusätzliche Sicherheit im Betrieb bedeutet. Desweiteren wurden in dieser Arbeit grundlegende Untersuchungen zur KONUS-Strahldynamik durchgeführt um künftige Auslegung von Linearbeschleunigern mit geringem Emitanzwachstum zu erleichtern.

[1] LORASR steht für "**Lo**ngitudinale und t**ra**nsversale **S**trahltransportrechnungen unter Berücksichtigung der **R**aumladung".

[2] http://irfu.cea.fr/Sacm/logiciels/index3.php

Die fünf IH-Strukturen wurden mit dem Programm CST Microwave Studio entworfen und simuliert. Die Kavitäten haben eine Zylinderform und sollen in einzelne Module von nicht mehr als $1,5\,\mathrm{m}$ Länge unterteilt werden um die Verkupferung und die Justage zu erleichtern (siehe Abbildung 0.4). Die IH-Strukturen sind folgendermaßen aufgebaut: In den zylindrischen Tanks sind zwei gegenüberliegende Trägerstrukturen angebracht, an denen die Driftröhren auf Stützen befestigt sind. Die Trägerstrukturen reichen nicht ganz bis an die Enden der Struktur heran, damit das Magnetfeld geschlossen werden kann. Um den Fluss des Magnetfeldes an den Enden der Kavität zu erhöhen, werden zusätzlich die äußersten Stützen abgeschrägt und Aussparungen in die Trägerstrukturen eingebracht. Dadurch wird der Querschnitt für den Magnetfluss erhöht. Mit diesen Maßnahmen wurden die Strukturen so optimiert, dass sie eine flache Feldverteilung aufweisen. Der gepulste Leistungsbedarf der fünf Kavitäten beträgt zwischen $0.8\,\mathrm{MW}$ und $1.1\,\mathrm{MW}$. Damit liegt die benötigte HF-Leistung pro Kavität deutlich unter dem GSI Design-Limit der Verstärkerleistung von $1.35\,\mathrm{MW}$. Folglich kann der in dieser Arbeit entwickelte Beschleuniger mit den bestehenden HF-Verstärkern des GSI-UNILAC betrieben werden [8]. Die effektiven Shuntimpedanzen der Kavitäten liegen im Bereich $Z_{\mathrm{eff}} = 90 - 152\,\frac{\mathrm{M\Omega}}{\mathrm{m}}$.

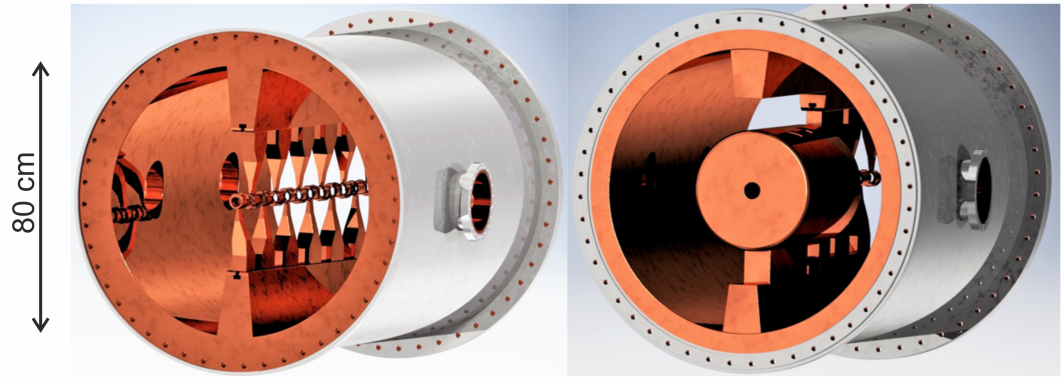

Abbildung 0.4: Beispiel für zwei Tankmodule des IH-Typ Beschleunigers. (Rendergrafik von D. Bänsch, Goethe Universität Frankfurt).

Die in dieser Arbeit entwickelten Strahldynamikauslegungen und Beschleunigerkavitäten können für die Verbesserung des GSI-UNILAC in Hinblick auf einen Uran Hochstrombetrieb für FAIR verwendet werden. Mit Hilfe der entwickelten MEBT Sektion können Strahlverluste im HSI verhindert und eine deutliche Verbesserung der Strahlqualität des UNILAC erreicht werden. Hierfür müssen weder der RFQ noch die zwei IH-Kavitäten des HSI verändert werden. Der auf IH-Strukturen basierende

Poststripper Beschleuniger stellt eine effiziente Lösung für den zukünftigen Hochstrombetrieb des UNILAC dar. Das Ersetzen des Poststripper Alvarez DTL mit der vorgeschlagenen, auf IH-Strukturen basierenden Lösung, reduziert die Kosten um mindestens 35 % im Vergleich zu einem neuen Alvarez DTL. Außerdem bleibt bei dieser Lösung noch Platz im UNILAC Tunnel für zukünftige Upgrades.

Der GSI UNILAC ist bereits heute der weltweit stromstärkste Linearbeschleuniger für schwere Ionen. Durch die in dieser Arbeit entwickelten Maßnahmen wird der gepulste Ionenstrom noch einmal deutlich erhöht. Dies ist notwendig um die hohen Anforderungen einer Hochstrom-Beschleunigeranlage mit Synchrotronkette wie FAIR zu erfüllen. Andere im Bau befindliche Anlagen wie Linearbeschleuniger mit langem Tastverhältnis (MSU FRIB[3], USA) oder Zyklotronanlagen (RIKEN RIBF[4], Japan) können hohe mittlere Ionenströme am Target erreichen. Um mit einem kurzen Tastverhältnis wie bei FAIR vergleichbare Intensitäten zu erreichen, ist somit das Erreichen möglichst hoher Ionenströme im Injektor-Beschleuniger unerlässlich. Insofern ist die hier beschriebene Entwicklung hochstromfähiger Linearbeschleuniger auch von Interesse für die Auslegung zukünftiger Anlagen zur Beschleunigung intensiver Schwerionenstrahlen.

[3]https://frib.msu.edu/
[4]http://www.nishina.riken.jp/RIBF/

Contents

1 Introduction

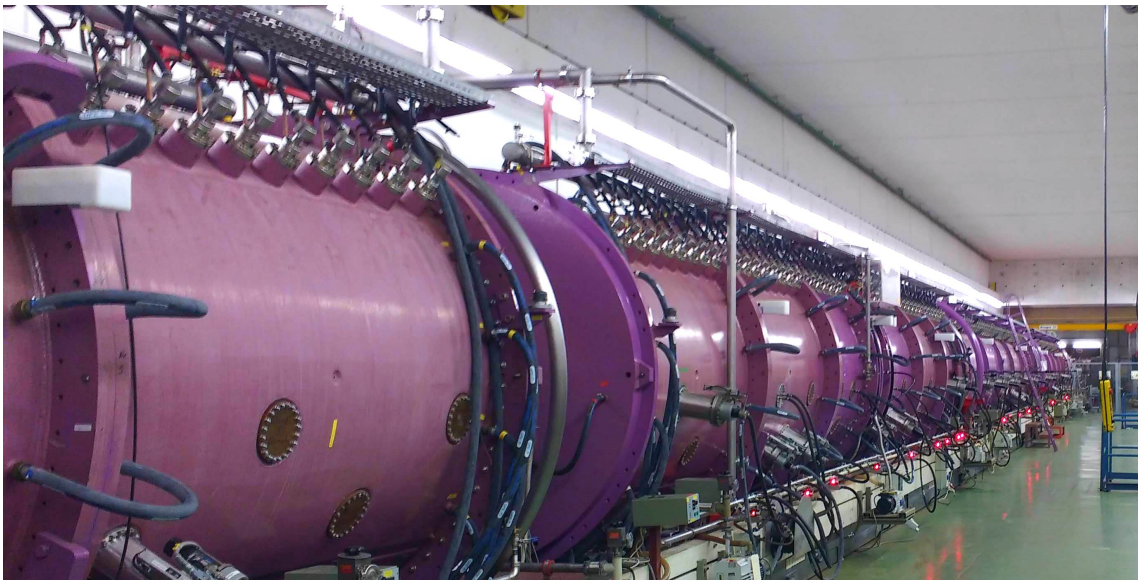

Figure 1.1: Picture showing the existing poststripper linac of the GSI UNILAC (October 2016).

The Facility for Antiproton and Ion Research FAIR is currently under construction at GSI Darmstadt and will provide unprecedented intensities of protons and heavy ions up to uranium at energies of up to 29 GeV for protons and 2.7 $\frac{\text{GeV}}{\text{u}}$ for U^{28+}. To achieve high intensities in the synchrotron accelerators, high beam currents have to be provided by the injector linear accelerators (*linacs*). High current heavy ion beams are provided by the Universal Linear Accelerator UNILAC, which in its current state however will not be able to provide the required FAIR beam currents. This thesis deals with the development of upgrades for the UNILAC to ensure its high current capability. The first improvement is a matching section MEBT[1] for the interface between the RFQ[2] and the IH-DTL[3] of the existing high current injector

[1]MEBT: "Medium Energy Beam Transport"
[2]RFQ: "Radiofrequency Quadrupole"
[3]IH-DTL: "Interdigital H-Mode-Structure Drift Tube Linac"

HSI at the UNILAC. With this new MEBT section, particle losses are eliminated and the overall beam quality is improved. As a second improvement, a complete replacement of the existing Alvarez-DTL is presented. A combination of efficient IH-type cavities and KONUS[4] beam dynamics results in a reduction of the linac length from about 60 m (Alvarez) to just 23 m (new IH-DTL) while providing the same energy and fulfilling FAIR requirements of a high beam current and beam quality. This thesis contains a detailed beam dynamics design of the new linac including some fundamental investigations of the KONUS beam dynamics concept. A cross-check of the beam dynamics design was performed with two independent multi-particle simulation codes. Detailed error studies were conducted to investigate the influence of manufacturing, alignment and operating errors on the beam dynamics performance. Additionally, all five linac cavities were designed, optimized, and their RF[5] parameters including power requirements calculated to provide a comprehensive linac design.

[4]KONUS: "Combined Zero Degree Structure" from the German "Kombinierte Null-Grad Struktur"
[5]RF: "Radio Frequency"

2 Linear Accelerators

In this chapter the properties of RF linacs and their beam dynamics are discussed with a special emphasis on heavy ion linacs. The general principle of RF linacs is the acceleration of charged particles with longitudinal electric fields generated in a resonant cavity. A variety of different geometries of such cavities is possible. In the following the most relevant geometries for heavy ion acceleration are detailed. The motion of particle bunches in the transverse and longitudinal planes is summarized under the term beam dynamics.

For more detailed information on RF linear accelerators, the book "RF Linear Accelerators" by Thomas P. Wangler [9] is recommended. Another recommended read, especially for beam dynamics topics, is the "Theory and Design of Charged Particle Beams" by Martin Reiser [10].

2.1 Accelerator Structures

The acceleration of charged particle beams using RF electromagnetic fields can be achieved with a variety of different structures. As a first popular approach the Wideröe DTL[1] developed by Rolf Wideröe in 1928 [11] should be mentioned. It is based on metallic tubes that are connected to a high frequency alternating voltage source.These drift tubes are connected to opposing polarity of a transmission line as shown in Figure 2.1. A particle beam with a given initial velocity v_0 traveling through the structure is then accelerated by the electric field formed in the gaps between the drift tubes. To be able to properly accelerate the beam, the geometry of the drift tube structure has to be matched to the velocity of the particles. Therefore the distance between two adjacent gaps is given by

$$L_{\mathrm{p,Wideröe}} = \frac{\beta_i \lambda}{2} \tag{2.1}$$

[1] DTL: "Drift Tube Linac"

with the particle velocity $\beta_i = \frac{v_i}{c}$ in units of c and the wavelength λ of the high frequency voltage source.

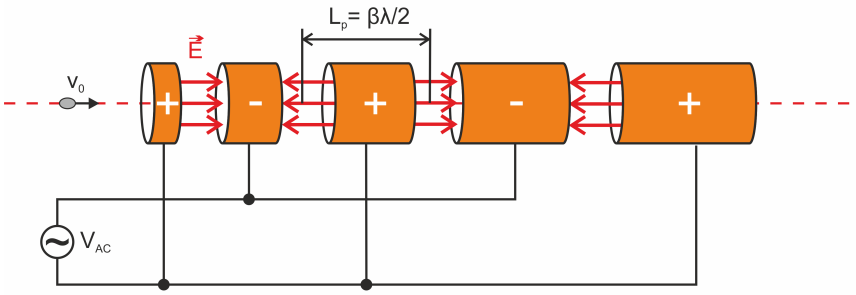

Figure 2.1: Layout of a high frequency alternating voltage Wideröe DTL.

A revolution in the linac design was the idea to use RF resonant cavities for the purpose of particle acceleration. To achieve this, the most simple approach is a pillbox cavity which is a hollow closed cylinder. The basic resonant mode of such a pillbox cavity with a transverse magnetic field (TM_{010}-mode) can be used to accelerate particles by the longitudinal electric field (see Figure 2.2). However, in this simple form only one RF cycle can be used to accelerate the particles. To build an accelerator in this way, a huge number of single cavities has to be arranged in a line which can be impracticable and inefficient.

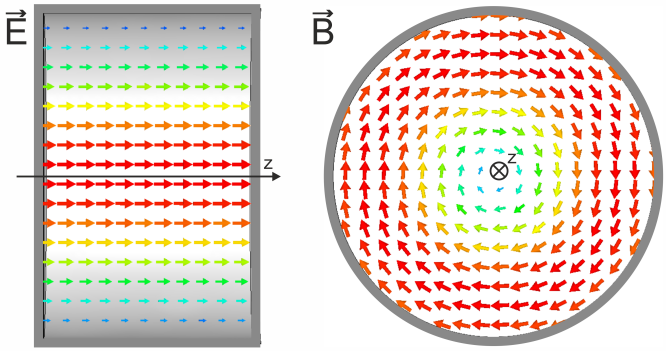

Figure 2.2: TM_{010}-mode of a pillbox cavity with the longitudinal electric field $\overrightarrow{E}$ (left) and the transverse magnetic field $\overrightarrow{B}$ (right) shown. Colors of the arrows indicate the amplitude of the field from high (red) to low (green/blue).

The concept proposed by Luis Alvarez [12, 13] was to make use of the same basic TM_{010} mode in a long pillbox cavity, but to introduce tubes into the cavity to shield

the particles from the electric field when the field would decelerate the beam. In the original approach, the transverse beam focusing was achieved with metallic grids within the drift tube aperture to generate electric focusing fields [14].

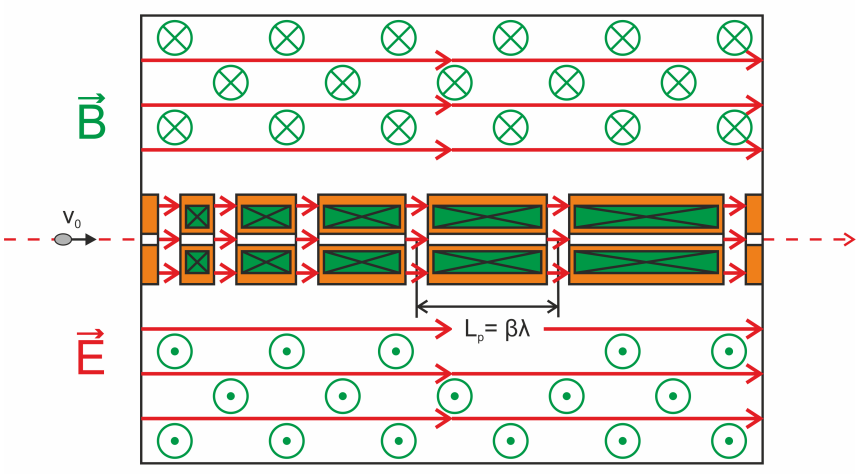

Figure 2.3: Layout and electromagnetic fields of an Alvarez DTL. The lenses (green, crossed) are mounted inside the drift tubes (orange).

In later Alvarez concepts each drift tube houses a magnetic quadrupole singlet lens for transverse focusing (see Figure 2.3). This concept is nowadays referred to as an Alvarez DTL. The period length of an Alvarez DTL is

$$L_{\mathrm{p,Alvarez}} = \beta\lambda. \tag{2.2}$$

One drawback of the TM_{010} mode is the long period length of $\beta\lambda$ between the accelerating gaps. Another downside is the large cavity diameter that results from the use of the basic mode. The basis of modern IH-type and CH-type cavities, is the use of H-modes (TE-modes) for acceleration [15, 16, 6]. While the basic TE_{111}-mode has no longitudinal component of the electric field, this can be changed by the introduction of drift tubes that are held by stems on opposing sides of the cavity walls (see Figure 2.4). While the main part of the magnetic field circles the cavity on the long sides, the introduction of drift tubes and stems leads to additional circular magnetic fields around the stems that induce currents in the stems and drift tubes. This way the ends of the drift tubes get charged electrically and an electric field concentrated between the drift tubes is formed which is directed in the longitudinal direction along the beam axis. Since the drift tubes are connected to opposing sides

of the cavity, the sign of the electric field changes from gap to gap. This structure is called an "Interdigital H-mode Structure", short "IH", which originates from the way the stems intertwine or "interdigitate". Therefore the IH-structure is also a

$$L_{\mathrm{p,IH}} = \beta\lambda/2 \tag{2.3}$$

structure like the Wideröe linac.

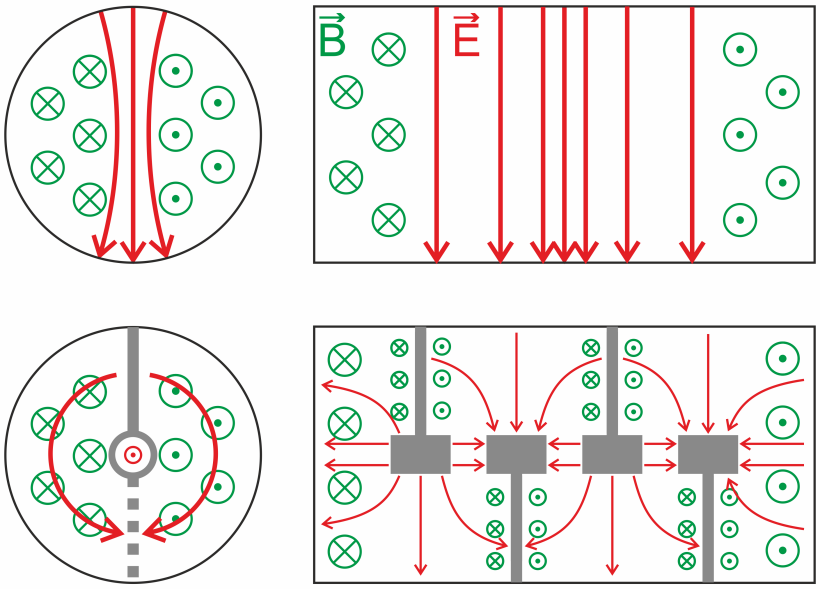

Figure 2.4: The TE_{111}-mode of an empty pillbox cavity (top) and the modified TE_{111}-mode of an IH-type cavity (bottom).

A cavity as shown in Figure 2.4 has an E_z field distribution that is highest in the center and decreases significantly toward the ends of the cavity since the TE_{111} mode has nodes in the E_z-field on the cavity ends. To get a flat voltage distribution in an IH-Type cavity, the stems are positioned on high girders in the cavity (see Figure 2.5). Such girder structures allow for a better guiding of the magnetic field across the whole cavity. They are typically undercut to allow a larger cross section area for the magnetic field in the cavity ends. This way, the TE_{111}-mode can be transformed to a $TE_{11(0)}$ mode that is much more useful for particle acceleration due to its flat field distribution on the beam axis (see also Chapter 7.1).

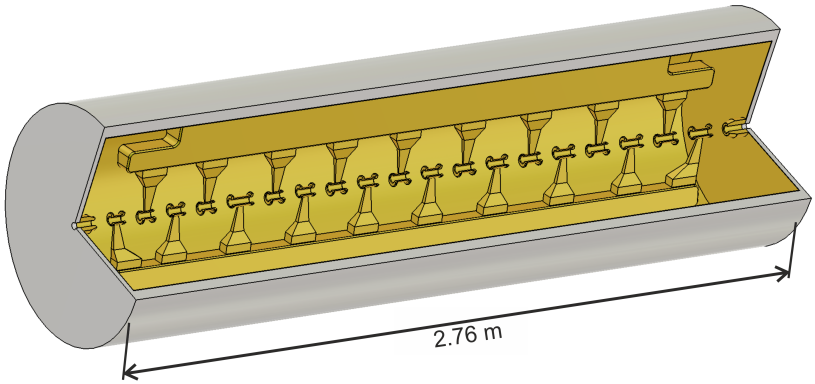

Figure 2.5: Example of an IH-type cavity at $108\,MHz$ for $\beta = 0.097$.

An example for the resulting IH-type structure is shown in Figure 2.5 and is widely used nowadays in heavy ion linacs due to its high shunt impedance and much smaller overall size compared to TM_{010} cavities. The typical ion velocity range for IH-type cavities is $\beta = 0.01 - 0.15$. A limiting factor for higher energies is the structure size of the cavities which becomes too small for manufacturing at frequencies $> 300\,\text{MHz}$. For higher β the period length increases and requires a frequency change to higher frequencies to reduce the gap lengths. The operating frequency is typically $< 250\,\text{MHz}$ for IH-type cavities. For example the two IH-type cavities of the High Current Injector at GSI have an operating frequency of 36 MHz and tank diameters of about 2 m [17, 18] while the injector linac for the Heidelberg Ion Therapy Center operates at 217 MHz leading to transverse cavity dimensions of less than 0.35 m [19].

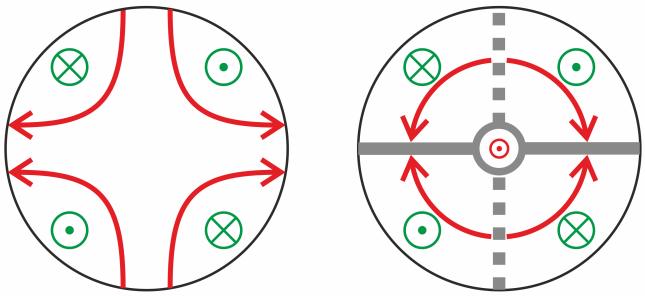

Figure 2.6: Cross section of the TE_{211}-mode in an empty cavity (left) and the modified CH-type cavity (right).

For higher ion velocities in the range of $\beta = 0.1 - 0.5$, cavities based on the TE_{211}-mode can be used since the cavity dimensions are larger than IH-type cavities at the

same frequency. To use the TE_{211}-mode for acceleration, the cavity is modified in a way similar to the IH-type cavity. The drift tubes are connected to the cavity outer wall by stems that span the whole diameter of the cavity and are positioned in the center of the stems. Since the stems are oriented in a crossed configuration, this type of cavity is called a "Crossbar H-Mode Structure", short "CH" [20]. In Figure 2.6, the electric and magnetic field for the cross section of a CH-type cavity and the corresponding pillbox mode are shown. Neighboring drift tubes are on opposite potentials and therefore the accelerating axial field is also that of a $\beta\lambda/2$ structure. The typical frequency range for CH-type cavities is $300 - 600\,\mathrm{MHz}$ [20, 21]. An example for a 325 MHz CH-type cavity is shown in Figure 2.7.

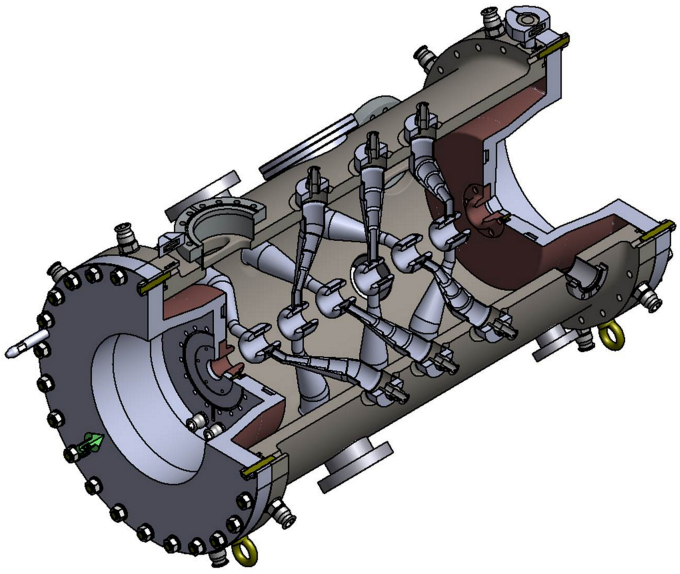

Figure 2.7: Example for a normal conducting CH-type cavity at 325.2 MHz designed for $\beta = 0.164$ [22].

2.2 RF Cavity Properties

Accelerator structures for ion linacs are constructed as standing wave cavity resonators in the radio frequency range. Different cavity resonant modes used for acceleration were discussed in Chapter 2.1. In this section, the most relevant parameters of RF cavities, namely the quality factor, shunt impedance and power requirements are discussed.

2.2.1 Stored Energy and Quality Factor

The total energy stored in the cavity $U(t)$ is the integral over the electromagnetic field for the cavity volume V given as

$$U(t) = \int_V \left(\frac{\epsilon_0}{2} |E(t)|^2 + \frac{1}{2\mu_0} |B(t)|^2 \right) dV \tag{2.4}$$

which is constant in time, while the energy oscillates between the electric and the magnetic field $E(t)$ and $B(t)$ respectively (ϵ_0 and μ_0 are the vacuum permittivity and vacuum permeability). With E_0 and B_0 being the maximum field amplitudes, the stored energy can also be expressed time independent as

$$U_{\text{stored}} = \frac{\epsilon_0}{2} \int_V |E_0|^2 dV = \frac{1}{2\mu_0} \int_V |B_0|^2 dV. \tag{2.5}$$

The quality factor (also Q-value) Q of a resonant cavity is the ratio of the stored field energy per RF cycle $P_{\text{cycle}} = \omega \cdot U_{\text{stored}}$ in the cavity and the power P_{loss} dissipated in the cavity walls due to ohmic losses

$$Q = \frac{\omega \cdot U_{\text{stored}}}{P_{\text{loss}}}, \tag{2.6}$$

where ω is the angular frequency of the excited resonant mode. For normal conducting linac cavities the Q-value usually is in the range of $10^3 - 10^5$ while for superconducting cavities it is in the range of $10^8 - 10^{10}$.

2.2.2 Shunt Impedance

The figure of merit to describe the acceleration efficiency of a linac cavity is the shunt impedance R_0. It is defined as the ratio of the peak accelerating voltage V_0 generated along the beam axis for a given dissipated power

$$R_0 = \frac{V_0^2}{P_{\text{loss}}}. \tag{2.7}$$

For a multi gap structure, the accelerating voltage V_0 of an accelerating cavity is defined as the sum of the individual peak gap voltages. To account for the energy gain of a particle with a relative phase of $\phi = 0\,^\circ$ the transit time factor T is included

(see Equation (2.31) in Chapter 2.5.1) to give the effective shunt impedance

$$R = R_0 \cdot T^2. \tag{2.8}$$

The most commonly used parameter in linac cavity design is the effective shunt impedance divided by the length of the cavity L_{cav}

$$Z_{\text{eff}} = \frac{R_0 \cdot T^2}{L_{\text{cav}}} = \frac{(V_0 T)^2}{P_{\text{loss}} \cdot L_{\text{cav}}}. \tag{2.9}$$

with the dimension $[Z_{eff}] = \frac{\text{M}\Omega}{\text{m}}$. Sometimes also the actual energy gain given by the mean particle synchronous phase ϕ_s is included to give

$$Z_{\text{eff}} \cdot \cos^2(\phi_{\text{s}}) \tag{2.10}$$

as a measure for the effectiveness of the accelerator design. An example of $Z_{\text{eff}} \cdot \cos^2(\phi_{\text{s}})$ for different linac structures including the poststripper IH-DTL from Chapter 6 is shown in Figure 2.8. The graph shows that, for particle velocities of up to 20 %, H-mode structures are significantly more efficient than conventional structures such as an Alvarez DTL.

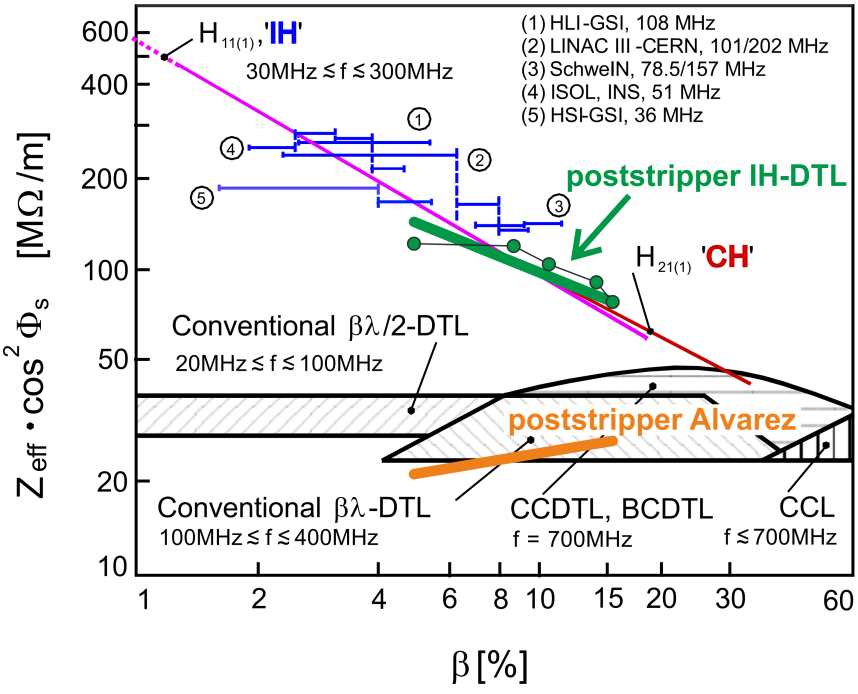

Figure 2.8: Effective shunt impedance for different normal conducting structures for $\beta = 1\,\% - 60\,\%$ (adapted from [18, 23]).

2.2.3 Beam Power

When the beam is accelerated in a linac cavity, energy is transferred from the electromagnetic field in the cavity to the beam. The RF power transferred to the beam is called the beam power

$$P_{\text{beam}} = I_{\text{beam}} \cdot \frac{\Delta W_{\text{beam}}}{q} \tag{2.11}$$

where I_{beam} is the average beam current, ΔW_{beam} is the beam energy gained passing the cavity and q is the charge of the individual particles of the beam. For example for a Uranium beam ionized to 28+ with $I_{\text{beam}} = 15\,\text{emA}$ and an energy gain in the cavity of $\Delta W_{\text{beam}} = 504\,\text{MeV}$ which is equal to an accelerating voltage of $V_0 T \cdot \cos(\phi_s) = 18\,\text{MV}$, the calculated beam power is $P_{\text{beam}} = 15\,\text{emA} \cdot \frac{504\,\text{MeV}}{28 \cdot e} = 270\,\text{kW}$. The total power required to run the accelerator is the sum of all power losses and the required beam power

$$P_{\text{total}} = P_{\text{loss}} + P_{\text{beam}}. \tag{2.12}$$

2.3 Particle Distributions and Twiss Parameters

A bunched particle beam in general can be described as a particle distribution in 6D phase space. Each particle within the bunch is identified by its locations in the three dimensions of space x, y, z and the corresponding momenta p_x, p_y, p_z. The more commonly used convention in linac literature is the use of x, y, z with the corresponding deflection angles x', y', z'. These coordinates can be transformed as

$$x' = \frac{p_x}{p},\ y' = \frac{p_y}{p},\ \text{and}\ z' = \frac{p_z}{p} \tag{2.13}$$

in reference to the total momentum p. In the longitudinal plane z, z' often the phase ϕ and energy W relative to the bunch center phase ϕ_{cp} (correlated with the RF) and energy W_{cp} are used. The particle distribution can then be viewed as three 2D projections of the transverse planes and the longitudinal plane (an example is shown in Figure 2.9).

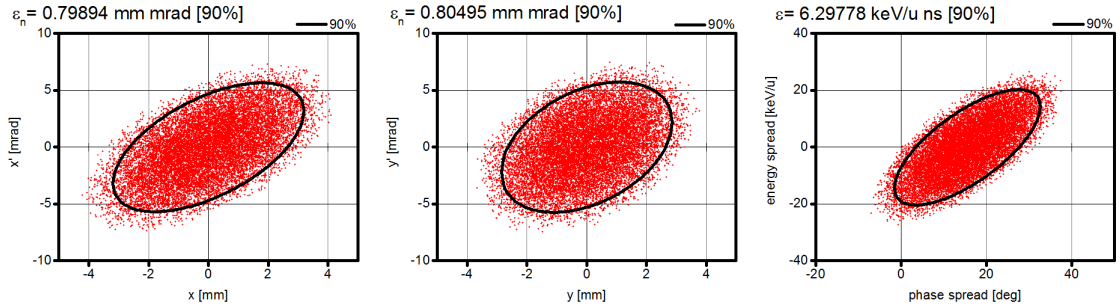

Figure 2.9: 2D projections of a particle bunch. The plots are x-x' (left) y-y' (middle) and $\phi - W$ (right).

For beam dynamics simulations usually a 6D particle distribution is generated by particles randomly populating a 4D or 6D hyperellipsoid (cw or bunched beam). The most popular distributions are the

- K-V (Kapchinsky and Vladimirsky) distribution which has homogeneously filled ellipses in all 2D projections [24, 25],
- the Gaussian distribution where the 6D hyperellipsoid is filled with a 6D Gaussian density distribution, which also means that the 2D projections are Gaussian,
- and the Waterbag distribution which is a 6D hyperellipsoid homogeneously filled with particles.

The simulations shown in Chapter 6 were all performed with Waterbag distributions. In the 2D projections of such particle distributions, the particles are confined within an ellipse with the area $A = \pi \cdot h \cdot h'$ where h and h' are the half axes of the ellipse. When the ellipse is in canonical orientation, the half axes h and h' can be directly related to the projected values of x, x', y, y', and ϕ, W. For each of these three 2D projections, the corresponding emittances $\epsilon_{x-x'}$, $\epsilon_{y-y'}$, and $\epsilon_{\phi-W'}$ are defined as the area of the beam ellipses divided by π. Typical conventions for the emittance units are

$$[\epsilon_{x/y}] = \text{mm·mrad};\ [\epsilon_{x/y}] = \mu\text{m·rad} \tag{2.14}$$

$$[\epsilon_z] = \frac{\text{keV}}{\text{u}} \cdot \text{ns};\ [\epsilon_z] = \text{MeV·deg};\ [\epsilon_z] = \text{mm·mrad} \tag{2.15}$$

where u is the atomic mass unit. The emittance of a beam is a measure of its quality. Usually the goal of linac design is to minimize emittance growth along the

accelerator.

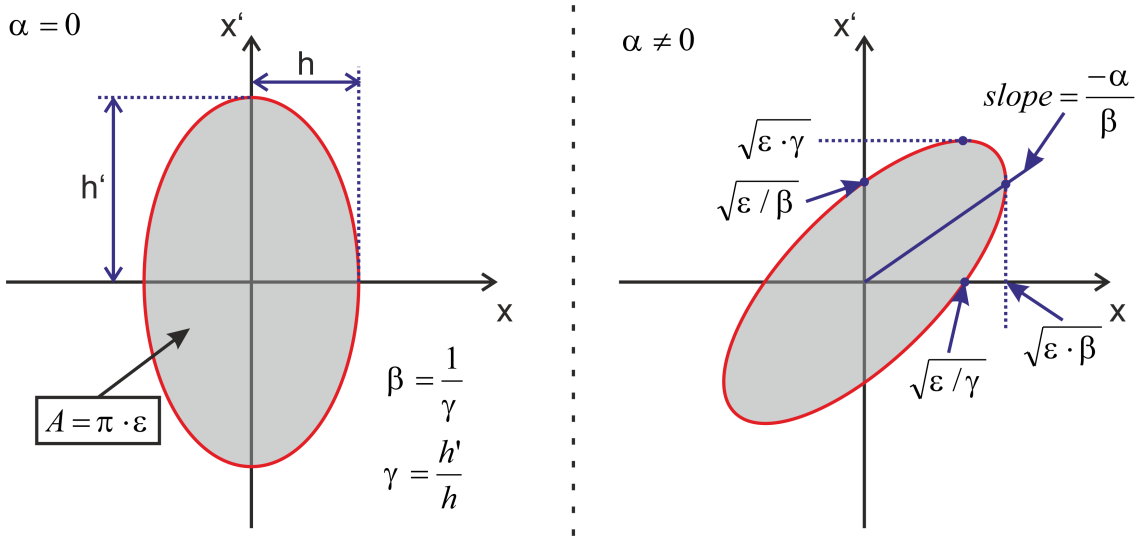

Figure 2.10: Geometrical relations of the Twiss parameters and the corresponding ellipse in x-x' for $\alpha = 0$ and $\alpha \neq 0$.

Each ellipse enveloping the particles can be characterized by the so called "Twiss" or "Courant-Snyder" parameters which describe the form of the ellipse corresponding to the equations [9]

$$\gamma x^2 + 2\alpha x x' + \beta x'^2 = \epsilon_x \tag{2.16}$$

and

$$\gamma = \frac{1 + \alpha^2}{\beta} \tag{2.17}$$

while α, β, γ are the Twiss parameters and ϵ_x the emittance of the ellipse. For y and z analogous equations can be formed. Figure 2.10 shows the geometrical "meaning" of those parameters. The parameter α is dimensionless and relates to the tilt of the ellipse. If $\alpha = 0$ the ellipse is not tilted, if $\alpha > 0$ or $\alpha < 0$, then the ellipse is tilted to the "left" or the "right" respectively.

2.4 Transverse Beam Dynamics

The particle motion in the transverse planes in a linear accelerator is the limiting factor for apertures and cavity lengths. Every particle beam has finite emittances $\epsilon_x = h_x \cdot h_{x'} > 0$, $\epsilon_y = h_y \cdot h_{y'} > 0$ and therefore if the beam has finite length in one dimension, it also has a finite momentum distribution. Consequently each particle beam is divergent in space and therefore will expand over time when drifting in free space. Additional effects that increase the beam size and divergence are space charge forces (especially for high current beams) and RF gap defocusing. To be able to accelerate beams over long distances (m to km), the beam has to be focused by external forces. For charged particle beams this can be achieved either with electric or magnetic fields acting on the particles in the transverse planes by the Lorentz force

$$\vec{F} = q \cdot \left(\vec{E} + \vec{v} \times \vec{B}\right). \tag{2.18}$$

For ion linacs, electric fields are used only up to about $\beta \approx 0.03$ for transverse focusing. Beyond that they are usually only used to make steering corrections of the beam with respect to the beam axis. Most transversely acting elements along ion linacs are based on magnetic multi-poles. The most basic types are magnetic dipoles that can bend the particle trajectory in one plane and arrays of magnetic quadrupoles that are used to focus the beam in both transverse planes. In this chapter the RF defocusing, beam focusing with magnetic quadrupole lenses and focusing lattices will be discussed.

2.4.1 RF Defocusing in Drift Tube Linacs

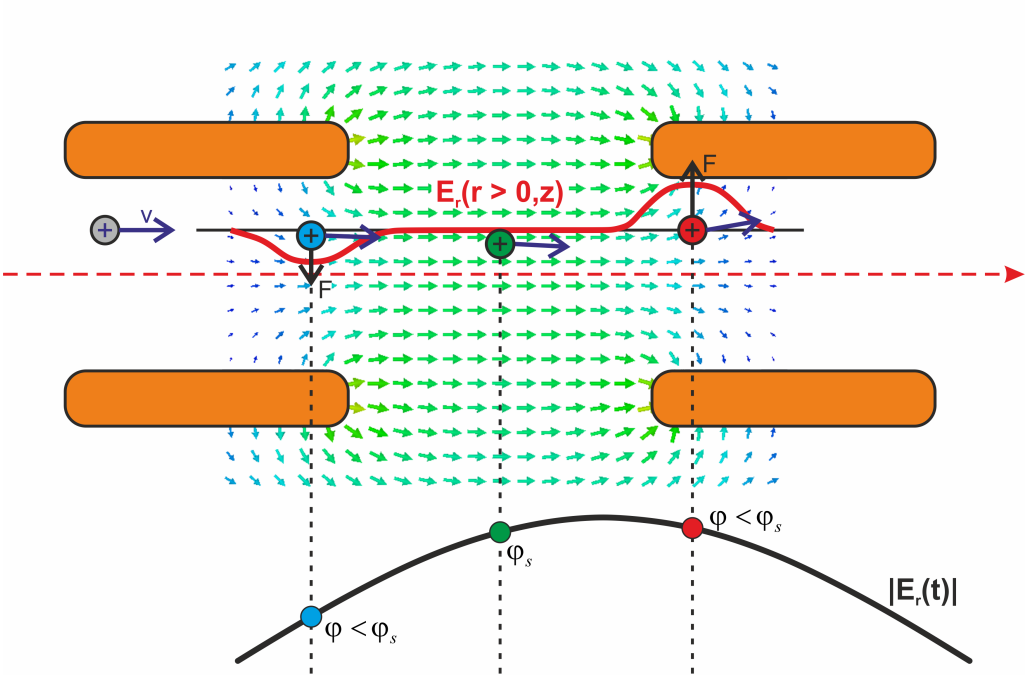

Figure 2.11: Electric fields in an accelerating gap.

For particles on a trajectory that is offset from the beam axis, the electric field between the drift tubes has a non-zero radial component $E_r(z, t, r > 0) \neq 0$ (see Figure 2.11). As a result, all particles that are not passing an accelerating gap perfectly centered during acceleration, experience a radial Lorentz force. At the beginning of the gap those particles experiences a force towards the beam axis which means that the beam is being focused by the electric field. Following that at the end of the gap the Lorentz force is deflecting these particles from the beam axis. The amplitude of the radial electric field is defined by a cosine function

$$E_r(r, z, t) = E_{r,0}(z, r) \cdot \cos(\omega t + \phi). \tag{2.19}$$

Therefore a net defocusing effect occurs for negative synchronous phases (see Figure 2.11) since the field amplitude of the focusing field in the beginning of the gap is lower (earlier time $\phi < \phi_s$) than the defocusing field at the end of the gap (later time $\phi > \phi_s$). For a synchronous phase $\phi_s = 0°$, both effects cancel out if the velocity change in the gap is neglected.

2.4.2 Magnetic Quadrupole Lenses

A magnetic quadrupole lens is made up of four poles arranged 90° apart around the beam axis where the opposing poles have the same polarity (see Figure 2.12). The quadrupole magnet is positioned with the beam axis going through its center. If a particle passes the lens off axis, it sees the magnetic field of the quadrupole. In a single quadrupole a particle beam is only focused in one transverse plane and defocused in the other. To achieve a linear increase of the magnetic field (and therefore a constant gradient $B' = \frac{\delta B_x}{\delta y} = \frac{\delta B_y}{\delta x} = \text{const}$) in both transverse planes, the shape of the pole tips has to be hyperbolic. This is true assuming infinite pole sizes and no saturation effects.

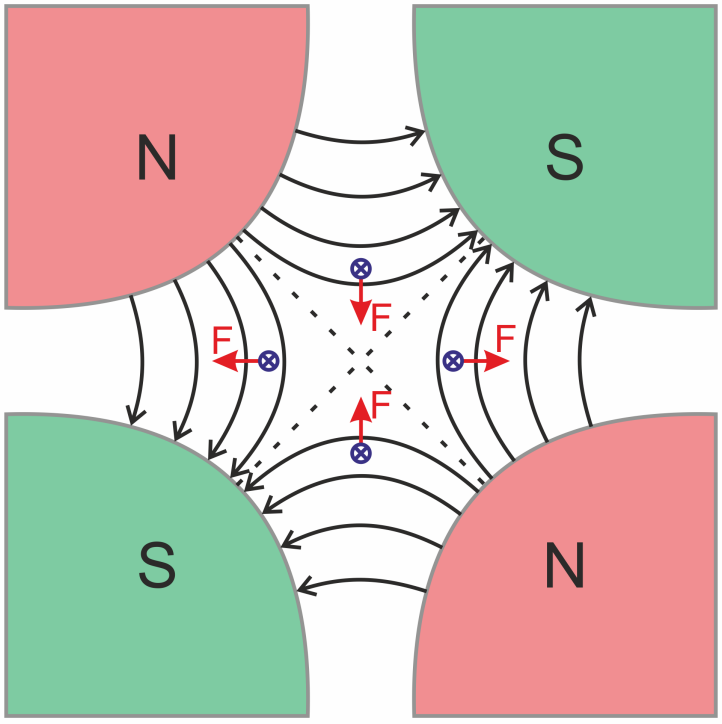

Figure 2.12: Layout and magnetic field distribution of a quadrupole magnet. The forces acting on a particle at different positions are shown, here the lens is focusing in the vertical plane and defocusing in the horizontal plane.

The magnetic field at the pole tip surface B_0 can then be calculated by

$$B_0 = B' \cdot r_a \tag{2.20}$$

with the field gradient B', where r_a is the aperture radius of the magnet assuming a symmetric layout in x and y. The force F experienced by a particle passing through the magnet is

$$\vec{F}(x,y) = \begin{pmatrix} F_x \\ F_y \end{pmatrix} = \begin{pmatrix} \gamma m_0 \ddot{x} \\ \gamma m_0 \ddot{y} \end{pmatrix} = \begin{pmatrix} -q v_z B_y(x) \\ +q v_z B_x(y) \end{pmatrix} \tag{2.21}$$

with q being the charge of the particle, γm_0 the Lorentz factor times the rest mass while assuming the velocity $v_z \gg v_x, v_y$. In accordance with (2.20) the magnetic field strengths in x and y are $B_y(x) = B' \cdot x$ and $B_x(y) = B' \cdot y$. Combining this with equation (2.21) and converting the time derivatives to $\dot{x} = \frac{dx}{dt} = \frac{dx}{dz} \cdot \frac{dz}{dt} = x' \cdot v_z$ the following equations of motion can be formulated

$$\frac{d^2x}{dz^2} + \frac{qB'}{\gamma m_0 v_z} \cdot x = 0 \tag{2.22}$$

$$\frac{d^2y}{dz^2} - \frac{qB'}{\gamma m_0 v_z} \cdot y = 0. \tag{2.23}$$

Defining the focusing strength κ as $\kappa = \frac{qB'}{\gamma m_0 v_z} = \frac{qB_0}{\gamma m_0 v_z r_a}$ and using the initial conditions $x = x_0$, $y = y_0\,, z = 0$, $x' = x'_0$, $y' = y'_0$, the solutions to these differential equations are

$$x = x_0 \cos(\sqrt{\kappa} z) + \frac{x'_0}{\sqrt{\kappa}} \sin(\sqrt{\kappa} z) \tag{2.24}$$

$$y = y_0 \cosh(\sqrt{\kappa} z) + \frac{y'_0}{\sqrt{\kappa}} \sinh(\sqrt{\kappa} z). \tag{2.25}$$

In Figure 2.13 the resulting particle trajectories defined by the solutions (2.24) and (2.25) for an example case are shown. For $\kappa > 0$ the quadrupole magnet is focusing the beam in the horizontal plane as described by the cosine and sine functions of the solution. Consequently the beam is being defocused in the vertical plane by the same magnet configuration.

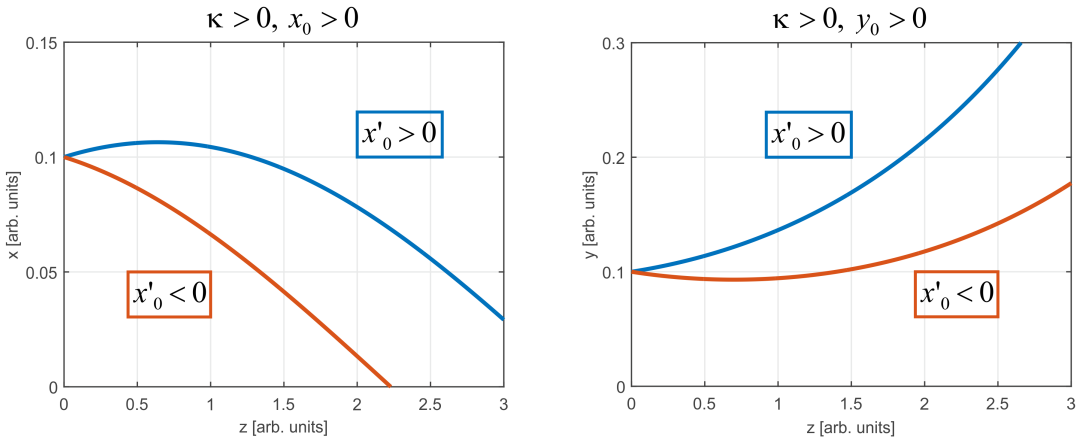

Figure 2.13: Exemplary solutions for the horizontal plane (left) and vertical plane (right) of a particle moving through a magnetic quadrupole lens.

By combining two quadrupoles with different polarities, simultaneous focusing in both planes can be achieved. This is called a quadrupole doublet (see Figure 2.14 (a)). For a quadrupole doublet the envelopes behind the lens are asymmetric. A more symmetric beam with a common beam waist in both transverse directions can be achieved with a quadrupole triplet lens (see Figure 2.14 (b)). A triplet lens is composed of three quadrupoles where the outer triplets have the same polarity and opposite polarity to the middle lens. The middle lens is usually about as long as the outer lenses combined with a ratio of $L_{\text{inner}}/L_{\text{outer}} = 0.9-1$ depending on the beam parameters [18, 21]. Using quadrupole triplet lenses, longer focusing periods can be achieved than with doublet or singlet focusing schemes.

(a)

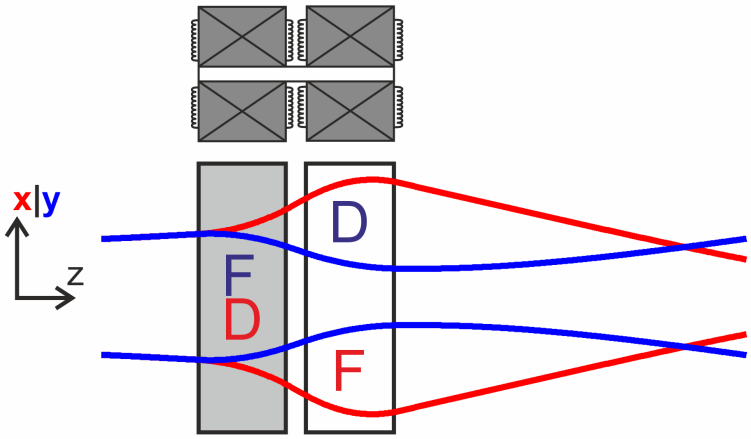

(b)

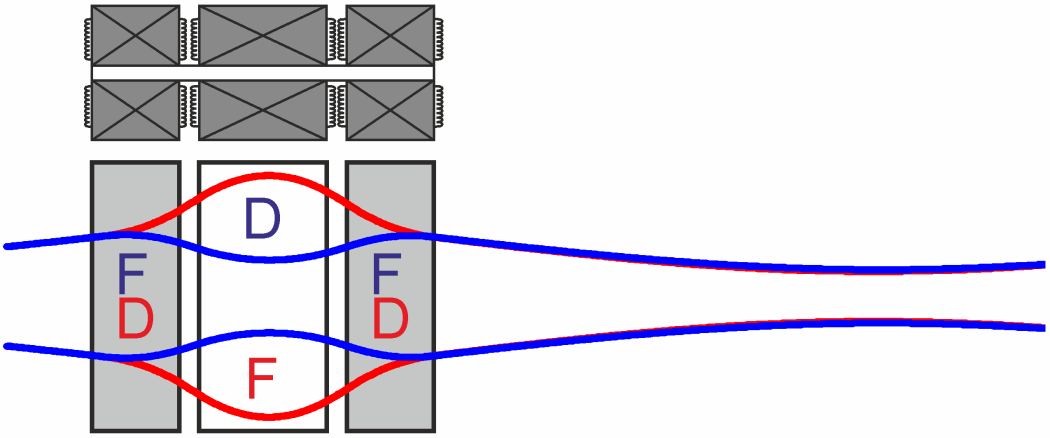

Figure 2.14: Layout and typical beam envelopes for doublet lens (a) and triplet lens (b). The red and blue lines represent the beam envelopes in the horizontal and vertical plane. The magnets effect on the beam in the respective plane is marked by **F** (focusing) and **D** (defocusing) in the corresponding color. As shown, the beam envelopes behind the doublet can not be matched, whereas the beam envelopes in both planes behind the triplet lens can be matched to the same focal point and envelope shape.

2.4.3 Focusing Lattices

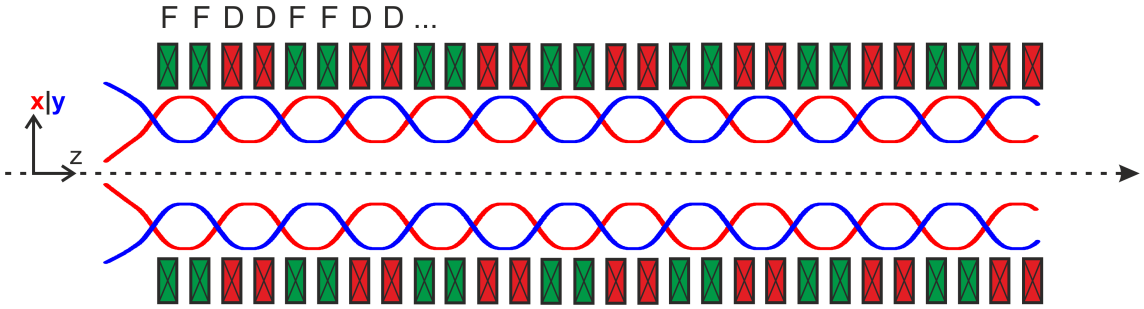

Figure 2.15: Example for a singlet focusing lattice in FF-DD configuration with respect to the horizontal plane. Horizontally focusing lenses are shown in green, defocusing lenses in red. The transverse beam envelopes are shown in red (horizontal) and blue (vertical).

Transverse focusing of an accelerated beam can be realized by the different combinations of quadrupole focusing magnets that are repeated in a focusing lattice. The notation for focusing lattices is **F** for a focusing quadrupole lens, **D** for a defocusing quadrupole lens and **0** for a drift line. For an Alvarez DTL where the quadrupoles are inside the drift tubes and therefore the focusing periods are short, periodic focusing is possible with quadrupole singlets. The focusing lattice basic cell for an Alvarez DTL is **F0D0** where each drift tube houses a lens with opposite polarity to its neighbors. The focusing period of a **F0D0** lattice is two times the linac period $L_{\mathrm{F0D0}} = 2 \cdot \beta\lambda$. To reduce the necessary gradient in the quadrupole singlets the **F0D0** lattice can be extended by doubling its elements to a **FFDD** lattice [26] (the **0** between the focusing elements is implied) which also doubles the focusing period $L_{\mathrm{FFDD}} = 4 \cdot \beta\lambda$. An example of the periodicity of the **FFDD** lattice is shown in Figure 2.15. The particle motion in a focusing lattice can be characterized by the phase advance per focusing period

$$\sigma_{\mathrm{trans}} = \frac{360^\circ}{N_p} \tag{2.26}$$

where N_p is the number of focusing periods in which the particle performs one full oscillation in the transverse planes. Transverse beam focusing for separated function linacs, where the focusing lenses are outside of a longer linac cavity, usually require much longer drift lengths between the focusing elements. In this case doublet or triplet magnets are used for the focusing lattice.

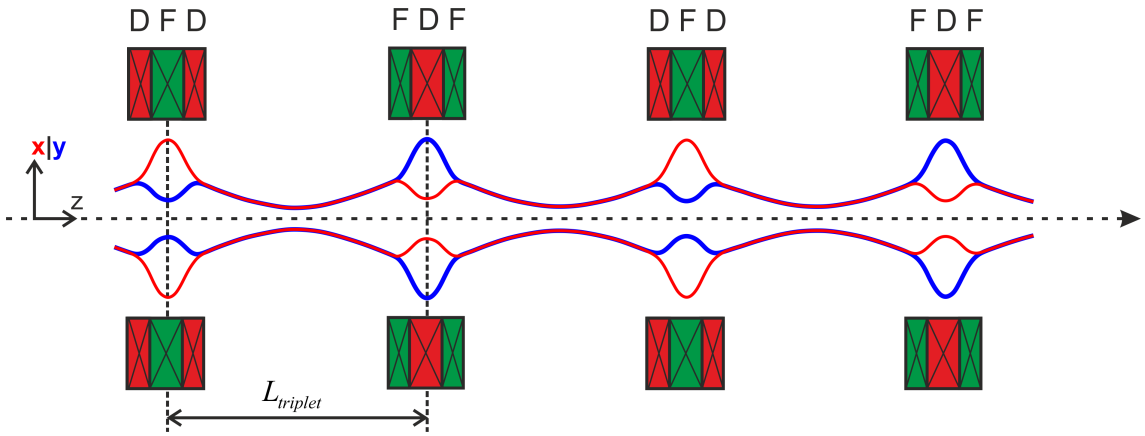

Figure 2.16: Example for a singlet focusing lattice in DFD-FDF configuration with respect to the horizontal plane. Horizontally focusing lenses are shown in green, defocusing lenses in red. The transverse beam envelopes are shown in red (horizontal) and blue (vertical).

For long cavities such as IH-type or CH-type cavities with up to several meters length, triplet focusing is necessary to ensure transverse confinement of the beam over these long structures. The most effective triplet lattice is the **DFD 0 FDF** lattice which is preferred over **DFD 0 DFD** or **FDF 0 FDF** lattices for KONUS beam dynamics [23]. Alternating **DFD** and **FDF** in the lattice provides equal beam sizes in both transverse planes and also better phase advance stability [27]. In Figure 2.16 the layout and beam envelopes for such a **DFD 0 FDF** lattice are shown. The focusing period L_{triplet} is defined as the distance between two consecutive triplet centers so that only one drift tube section is contained within this period. As shown in Figure 2.16 triplet lattices provide periodic focusing over long distances. The phase advance for triplet lattices is defined for the period length L_{triplet} while the periodicity of the lattice is twice as long.

2.5 Longitudinal Beam Dynamics

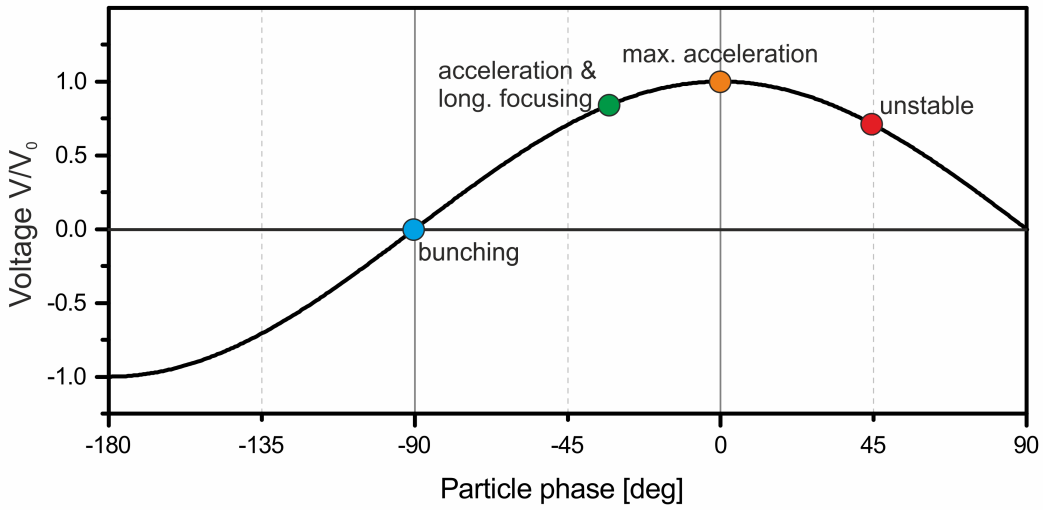

Figure 2.17: Magnitude of the accelerating voltage of an accelerating gap.

Charged particles such as electrons, protons and heavier ions can be accelerated with time-dependent longitudinal electric fields. However, for a continuous beam of charged particles in a RF linac, not all particles are accelerated. This is due to the fact, that half of the particles feel a force from the electric field, that is directed opposite to their motion. Therefore the particle beam in a RF linac is separated into particle bunches where a maximum of one bunch per RF cycle is allowed. This way the particle bunch can be accelerated if its phase ϕ relative to the RF electric field in the gap between two drift tubes is in the correct range (see Figure 2.17). The acceleration voltage of the gap is given by $V(\phi) = V_0 \cdot T \cdot \cos(\phi)$ with the transit time factor T (see following section 2.5.1). If the particle bunch has a phase of $0\,^\circ$, the acceleration is maximized since $V = V_0 \cdot T$. However, the particle bunch is not point-like but has finite dimensions in the three coordinates x,y and z[2] and the corresponding momenta. Since the particle bunch contains particles with different speeds, they arrive at different times in the gap center. If a particle is faster, it arrives earlier than the bunch center and therefore has a phase smaller than the bunch center phase ϕ_{cp}. Slower particles, arriving later than the bunch center, have a larger phase.

[2]The convention in linear accelerator physics is that x = horizontal, y = vertical and z = beam axis.

So if the bunch center synchronous phase is $\phi_{\mathrm{cp}} = 0\,^\circ$, both early and late particles get less acceleration than the particles in the bunch center. This leads to a simultaneous increase of the bunch phase- and energy-width which is considered an unstable beam motion. A common approach to avoid this is to use a bunch center phase in the range of about $-40\,^\circ \leq \phi_{\mathrm{cp}} \leq -30\,^\circ$, where the acceleration is still $75\,\% - 85\,\%$ of the maximum value. In this case, early particles see a lower accelerating field while late particles see a higher accelerating field. Therefore the main benefit of a negative synchronous phase is that the beam is effectively compressed in energy and therefore also in phase in following gaps (called bunching the beam) while the bunch as a whole is accelerated. Acceleration at positive synchronous phases would lead to the opposite effect and therefore to a widening of the particle bunch and unstable beam motion. The effect of beam bunching is highest for a synchronous phase of $\phi_{\mathrm{cp}} = -90\,^\circ$ while on average no energy is gained. A cavity operated at $\phi_{\mathrm{cp}} = -90\,^\circ$ is called a buncher cavity and is used to reduce the phase and/or energy width of a beam e.g. after a long drift section. More advanced acceleration schemes make use of a changing synchronous phase along the linac. Examples are the Alternating Phase Focusing (APF) [28], Equidistant Multigap Structures (EQUUS) [29, 30], and KONUS [18, 7]. The KONUS beam dynamics concept uses sections with ϕ_s close to zero degrees and additional short sections at negative synchronous phase to improve the acceleration efficiency and reduce RF defocusing (see Chapter 3).

2.5.1 Energy Gain in an Accelerating Gap

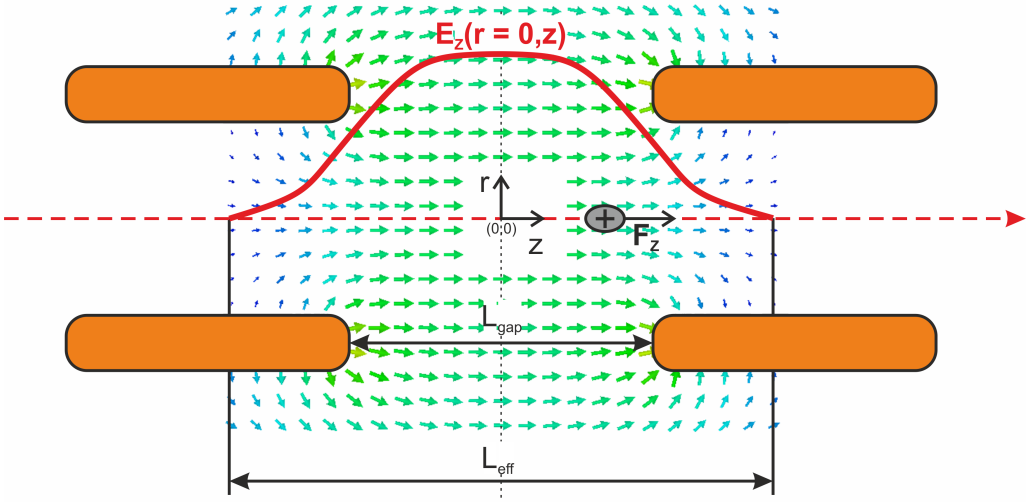

Figure 2.18: Schematic electric field distribution in an accelerating gap. The accelerating force F_z is caused by the longitudinal component E_z of the electric field on the beam axis (radius $r = 0$). The beam is moving in the direction z.

When a particle bunch passes the accelerating gap, it experiences the electric field between the two drift tubes (see Figure 2.18). If the beam is in the correct phase with the electric field of the cavity it is accelerated in the direction of the beam motion. In the following, the particle bunch will be reduced to its center of mass particle to describe the motion of the beam. The electric field E_z contributing to the acceleration of the particle can be expressed as the time dependent field

$$E_z(r, z, t) = E_z(r, z) \cdot \cos(\omega t(z) + \phi) \tag{2.27}$$

where the phase ϕ relates the position of the particle relative to the RF cycle (with the angular frequency ω) in the center of the gap. For convenience, the coordinate origin is set to the center between the drift tubes on the beam axis. With equation (2.27), the energy gain of the beam after passing the gap is

$$\Delta W = \int_{-\frac{L_{\text{eff}}}{2}}^{\frac{L_{\text{eff}}}{2}} q \cdot E_z(r, z, t)\, dz = q \int_{-\frac{L_{\text{eff}}}{2}}^{\frac{L_{\text{eff}}}{2}} E_z(r, z) \cdot \cos(\omega t(z) + \phi)\, dz \tag{2.28}$$

where L_{eff} is the length from the beginning to the end of the electric field amplitude between the gaps as seen in Figure 2.18. Usually this value is larger than the geometric gap length L_{gap} since the field penetrates into the tube to some extent. The maximum voltage between the two drift tubes on the beam axis is given by

$$V_0 = \int_{-\frac{L_{\text{eff}}}{2}}^{\frac{L_{\text{eff}}}{2}} E_z(0,z)\,dz \tag{2.29}$$

with $r = 0$ being the position of the beam axis. Since the particle passes the gap with a finite speed, the electric field changes during this motion. Therefore the particle will always effectively see a voltage lower than the maximum voltage V_0. The maximum effective voltage is experienced by the particle if $\phi = 0$ when the particle is at the gap center and therefore is

$$V_{eff=} \int_{-\frac{L_{\text{eff}}}{2}}^{\frac{L_{\text{eff}}}{2}} E_z(0,z) \cdot \cos(\omega t(z))\,dz \tag{2.30}$$

where it is important to note that the time is dependent on the position of the moving particle $t = t(z)$. The following quotient of the maximum voltage and the maximum effective voltage is called the "Transit Time Factor"

$$T = \frac{V_{\text{eff}}}{V_0} = \frac{\int_{-\frac{L_{\text{eff}}}{2}}^{\frac{L_{\text{eff}}}{2}} E_z(0,z) \cdot \cos(\omega t(z))\,dz}{\int_{-\frac{L_{\text{eff}}}{2}}^{\frac{L_{\text{eff}}}{2}} E_z(0,z)\,dz} \leq 1. \tag{2.31}$$

If the velocity change of the particle in the gap is neglected $\omega t(z)$ can be approximated as

$$\omega t(z) = \frac{2\pi c z}{v\lambda} = \frac{2\pi z}{\beta\lambda} \tag{2.32}$$

by expressing the angular frequency as $\omega = 2\pi\frac{c}{\lambda}$ and the time as $t = \frac{z}{v}$ with the initial particle velocity v and the corresponding $\beta = \frac{v}{c}$.

The transit time factor is

$$T = \frac{V_{\text{eff}}}{V_0} = \frac{\int_{-\frac{L_{\text{eff}}}{2}}^{\frac{L_{\text{eff}}}{2}} E_z(0,z) \cdot \cos(\frac{2\pi z}{\beta\lambda})\, dz}{\int_{-\frac{L_{\text{eff}}}{2}}^{\frac{L_{\text{eff}}}{2}} E_z(0,z)\, dz}. \tag{2.33}$$

Finally the energy gain of the bunch center particle can be expressed as

$$\Delta W = q \cdot V_0 \cdot T \cdot \cos(\phi) = q \cdot V_{\text{eff}} \cdot \cos(\phi) \tag{2.34}$$

which is the common form to estimate the energy gains in an accelerating structure. The energy is usually measured in units of electron Volts eV, which is the energy equivalent of an electron being accelerated by a voltage of 1 V.

2.5.2 Particle Motion in Longitudinal Phase Space

The longitudinal motion of the particle bunch in an accelerator structure can be approximately calculated by the "thin gap" approximation. In this model the acceleration in each gap is reduced to the gap center. In the gap center a particle experiences the effective voltage $V = V_{\text{eff,i}} \cdot \cos(\phi_i)$ depending on the particle's phase relative to the cavity RF cycle (as described at the beginning of Chapter 2.5). The particle velocity β_i is assumed constant between two adjacent gaps i and i+1 (see Figure 2.19).

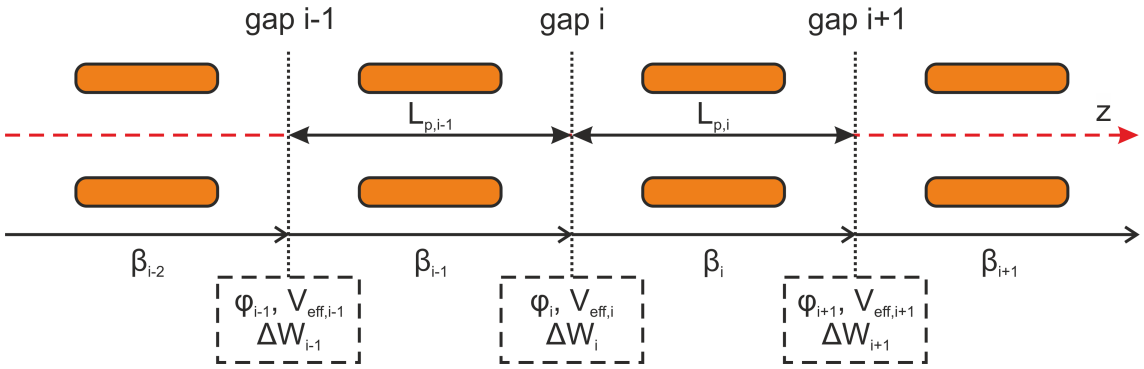

Figure 2.19: Definition of variables of an accelerating structure with n gaps.

A linac structure is characterized by the so called virtual synchronous particle with phase $\phi_{i,s}$ and velocity $\beta_{i,s}$. This synchronous particle is the reference of the linac structure design, having the same relative phase to the cavity RF in each gap. It satisfies the condition for the period length $L_p = \beta\lambda/n$, where λ is the wavelength of the cavity resonance frequency and n an integer value. $n = 2$ is valid for H-mode accelerators and will be used in the following. The energy gain of the synchronous particle in the center of gap i is given by

$$\Delta W_{i,s} = q \cdot V_{\text{eff,i}} \cdot \cos(\phi_{i,s}) \tag{2.35}$$

and for an arbitrary particle k of the bunch

$$\Delta W_{i,k} = q \cdot V_{\text{eff,i}} \cdot \cos(\phi_{i,k}). \tag{2.36}$$

Their total energies after acceleration in the gap are

$$W_{i,s} = W_{i-1,s} + \Delta W_{i,s} = W_{i-1,s} + q \cdot V_{\text{eff,i}} \cdot \cos(\phi_{i,s}) \tag{2.37}$$

and

$$W_{i,k} = W_{i-1,k} + \Delta W_{i,k} = W_{i-1,k} + q \cdot V_{\text{eff,i}} \cdot \cos(\phi_{i,k}), \tag{2.38}$$

respectively. The energy difference of the particle k to the synchronous particle therefore is

$$\Delta(W_{i,k} - W_{i,s}) = q \cdot V_{\text{eff,i}} \cdot [\cos(\phi_{i,k}) - \cos(\phi_{i,s})]. \tag{2.39}$$

In general, the particle k of a bunch does not have the same energy as the synchronous particle, meaning $W_{i-1,k} \neq W_{i-1,s}$. As a result, the particle phase $\phi_{i,k}$ is determined by the difference in travel time compared to the virtual synchronous particle. The travel time of the synchronous particle is

$$t_{i-1,s} = \frac{T}{2} = \frac{L_{p,i-1}}{\beta_{i-1,s} \cdot c} \tag{2.40}$$

where T is the period length of the RF cycle. Using (2.40) the travel time of the particle k can be written as

$$t_{i-1,k} = \frac{L_{p,i-1}}{\beta_{i-1,k} \cdot c} = \frac{\beta_{i-1,s}}{\beta_{i-1,k}} \cdot t_{i-1,s}. \tag{2.41}$$

In general, the phase $\phi_{i,k}$ of the particle relative to the phase in the preceding gap center $\phi_{i-1,k}$ is

$$\phi_{i,k} = \phi_{i-1,k} + \pi \frac{\Delta t_{k,s}}{t_{i-1,s}} = \phi_{i-1,k} + \pi \frac{t_{i-1,k} - t_{i-1,s}}{t_{i-1,s}} \tag{2.42}$$

which can be simplified using (2.41) to the form

$$\phi_{i,k} = \phi_{i-1,k} + \Delta\phi_{i,k} = \phi_{i-1,k} + \pi \cdot \left(\frac{\beta_{i-1,s}}{\beta_{i-1,k}} - 1 \right). \tag{2.43}$$

As a result, the difference between the k particle phase and the phase of the synchronous particle then is

$$\Delta(\phi_{i,k} - \phi_{i,s}) = \Delta\phi_{i,k} - \underbrace{\Delta\phi_{i,s}}_{=0} = \pi \cdot \left(\frac{\beta_{i-1,s}}{\beta_{i-1,k}} - 1 \right) = -\pi \frac{\beta_{i-1,k} - \beta_{i-1,s}}{\beta_{i-1,k}}. \tag{2.44}$$

Equations (2.39) and (2.44) describe the particle motion in the phase space for each particle of the bunch. Using the relativistic expression for the energy of an

accelerated particle [9]

$$\Delta W = \Delta\beta \cdot \beta \cdot \gamma^3 \cdot mc^2 \tag{2.45}$$

and inserting it into (2.44), the phase difference in dependence of the initial energy is

$$\Delta(\phi_{i,k} - \phi_{i,s}) = -\pi \frac{W_{i-1,k} - W_{i-1,s}}{\beta^3_{i-1,s} \cdot \gamma_{i-1,s} \cdot mc^2}. \tag{2.46}$$

Finally, equations 2.39 and 2.46 describe the motion of the particles in the phase space when they are accelerated by an array of accelerating gaps with a $\beta\lambda/2$ period. These formulas can be solved numerically to predict the particle motion of a linac design. The stability of the particle motion is a key concern in linac beam dynamics.

Stability of Longitudinal Particle Motion

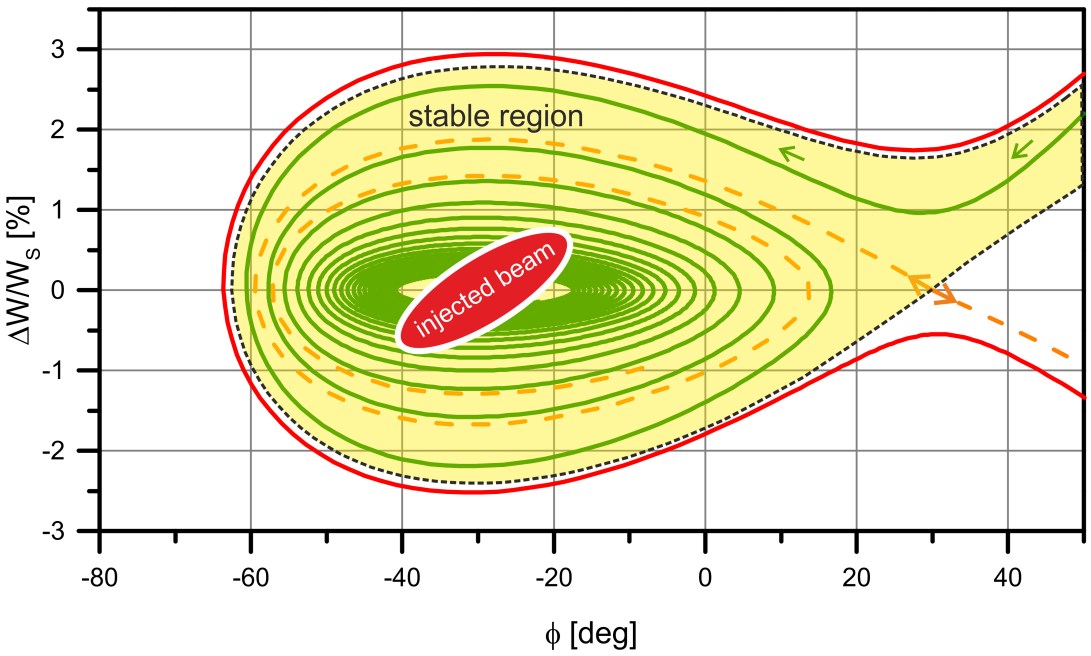

Figure 2.20: Particle motion in the phase space for $\phi_s = -30°$. The stable region is marked in yellow.

The particle motion for different injection parameters based on equations (2.39) and (2.46) is plotted for synchronous phases of $\phi_s = -30°, -90°,$ and $0°$ in Figures 2.20 to 2.22, respectively. These plots were generated assuming a constant energy gain G multiplied by the cosine of the particle phase (i.e. $\Delta W = G \cdot \cos(\phi)$) for each gap. The phase space of the commonly used negative synchronous phase structure

for $\phi_s = -30°$ is shown in Figure 2.20. In this case, the beam is accelerated, as well as focused in the longitudinal plane. If the particle is injected in the stable region (yellow area), it will move on a spiral orbit nearing the virtual synchronous particle of the structure (green line in Figure 2.20). This area is also referred to as the "bucket" since it can be modeled as a potential well that traps the accelerated particles. If the particle is injected outside of the stable region, over time it will get out of sync and will eventually be lost (red line in Figure 2.20). Therefore if a particle beam is injected with $\phi_{\mathrm{cp}} - \phi_s = 0$ and $W_{\mathrm{cp}} - W_s = 0$ and its emittance is (much) smaller than the stable region in the phase space of the negative synchronous structure, the beam could theoretically be accelerated by an infinitely long structure. The stable region around the negative synchronous particle is roughly $-2 \cdot |\phi_s| \leq \phi \leq |\phi_s|$.

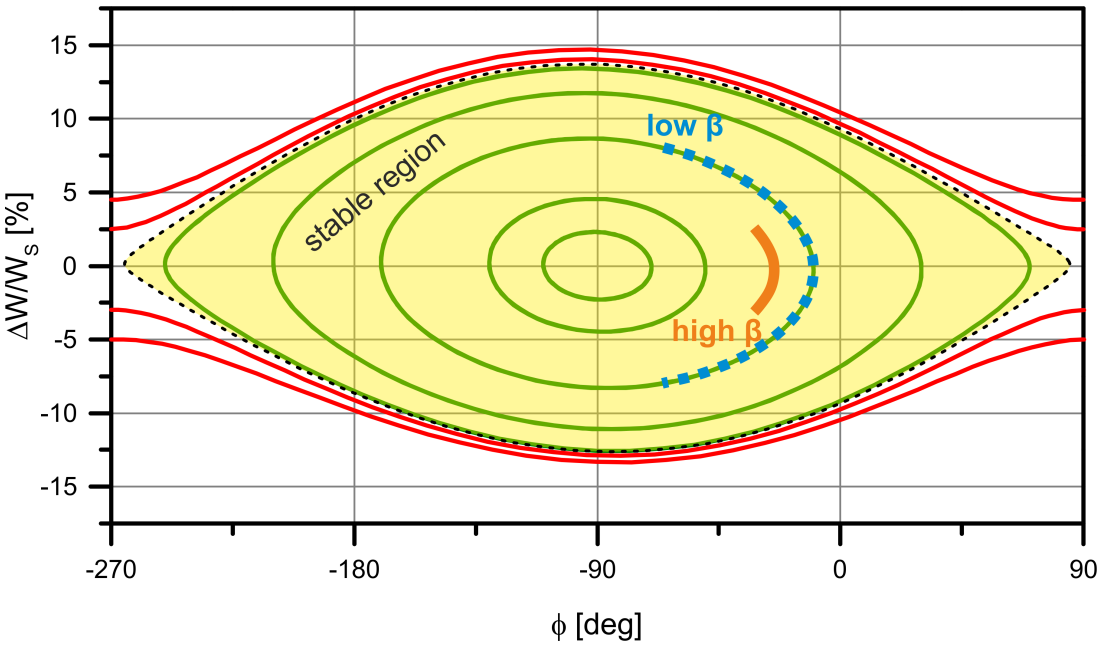

Figure 2.21: Particle motion in the phase space for $\phi_s = -90°$. The stable region is marked in yellow.

A structure with a synchronous phase of $\phi_s = -90°$ has the largest stable area (see Figure 2.21), while no acceleration of the beam takes place in such a structure. Around the synchronous particle, the particles move on closed orbits in the phase space. In equidistant multi gap structures (also called EQUUS [28], constant-β cavities) the geometrical virtual particle has $\phi_s = -90°$. However, the beam can be injected with an energy lower than that of the virtual synchronous particle, which corresponds to a negative phase typically in the range of $\phi_{\mathrm{cp}} = -60°$ to $-30°$.

This way, an energy gain can be achieved by only using part of the closed orbits (examples of trajectories are shown in Figure 2.21).

By variation of the cavity field amplitude and phase the energy gain in the cavity can be adjusted in a wide range. The main application of EQUUS is the acceleration of particles where the velocity change is small enough and the beam can be accelerated at a negative phase, e.g. $\phi_{\mathrm{cp}} = -20°$, while it will only shift slowly in phase [9] (see orange line in Figure 2.21). For slower beams ($\beta = 5 - 10\,\%$) the EQUUS beam dynamics concept can also be used if energy variability is required [30, 29]. Here the injected beam starts with a significantly lower energy than the geometric synchronous particle ($-10\,\%$ or less) and a negative phase. The beam will then travel towards more positive phases and get closer to the energy of the virtual particle. In a symmetric configuration, the beam will pass the point $W_{\mathrm{cp}} = W_s$ at a synchronous phase closer to 0° and then return to the initial negative phase of the injection with a higher energy than the virtual synchronous particle of the cavity (see blue dashed line in Figure 2.21).

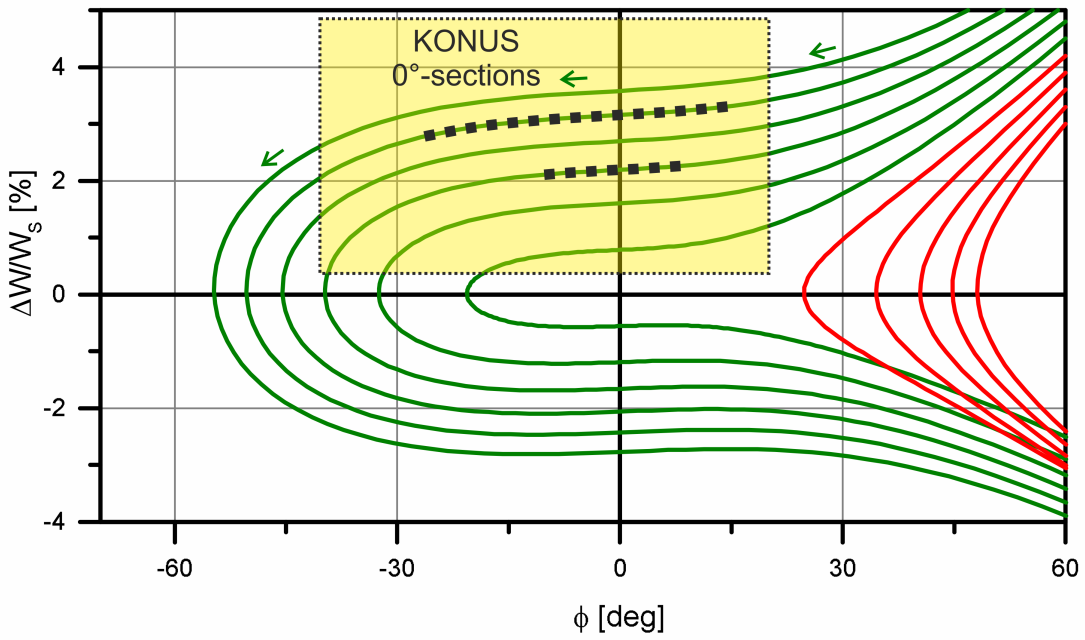

Figure 2.22: Particle motion in the phase space for $\phi_s = 0°$. No stable region for continuous acceleration exists.

If the virtual synchronous particle phase is $\phi_s = 0°$, the resulting paths for particles accelerated by this structure show no stable region, within which the beam would be

contained to a certain part of the phase space. Instead, all injected particles will drift away from the synchronous particle eventually (see Figure 2.22). However, similar to the EQUUS concept, an acceleration of the beam can still be achieved by using only parts of the available phase space paths. If a particle is injected near $\phi_{\mathrm{cp}} = 0°$ and with an excess energy compared to that of the synchronous particle $W_{\mathrm{cp}} > W_s$ then the beam can be accelerated efficiently. The particle moves along the given path towards more negative (earlier) phases since it is faster than the synchronous particle while also the relative energy difference to the synchronous particle gets smaller. Examples of such paths are shown in Figure 2.22 as dashed black lines. However, since in this case the beam is close to $\phi = 0°$ much less longitudinal focusing than for a negative synchronous phase is acting on the beam. This can be counteracted by adding accelerating gaps at a negative synchronous phase. Such a combination is then called the "Combined Zero Degree Structure" (KONUS). Further details on KONUS beam dynamics will be explained in the following Chapter 3.

3 KONUS Beam Dynamics Concept

The Combined Zero-Degree Structure KONUS (from the German "Kombinierte Null-Grad Struktur") was developed to achieve high acceleration efficiency with H-mode cavities [7, 18]. Its main advantage is the reduction of RF defocusing effects, allowing the beam to pass an increased number of accelerating gaps between two transversely focusing lenses. Another benefit is an increased energy gain in the linac structure by accelerating the beam near a synchronous phase $\phi_s = 0°$. In a KONUS structure, the necessary longitudinal beam focusing and matching is achieved by additional short rebuncher sections with a negative synchronous phase at the beginning of each KONUS period. The average synchronous phase of a KONUS linac is usually in the range of $-20° \leq \bar{\phi}_s \leq -10°$. Which is an increase in the energy gain for a given cavity voltage in comparison to negative synchronous phase structures where the mean synchronous phase is usually in the range of $-40° \leq \bar{\phi}_s \leq -25°$. For example, if

$$\bar{\phi}_{\mathrm{s,KONUS}} = -15° \text{ and } \bar{\phi}_{\mathrm{s,nSynch}} = -35° \tag{3.1}$$

then the difference in energy gain for the same cavity voltage is

$$\frac{\Delta W}{W} = \cos(-15°) - \cos(-35°) = 14.7\,\%. \tag{3.2}$$

The RF defocusing effect as discussed in Chapter 2.4.1 is dependent on the synchronous phase of the accelerated particle. A synchronous phase close to $\phi_s = 0°$ leads to a reduction of the RF defocusing effect. This way, the cavities between two focusing triplet lenses can be longer with KONUS than with conventional negative synchronous phase structures.

3.1 The KONUS lattice period

In KONUS linacs, a triplet DFD-FDF (or FDF-DFD) lattice is used for transverse focusing. The transverse focusing scheme with the corresponding beam envelopes is shown in Figure 3.1. In this example a cavity with two internal triplet lenses is shown. Usually the focusing triplet channel is designed so that the beam waist in both transverse planes is close to the middle of the drift tube section in between the lenses. This way long sections with good aperture clearance can be achieved. The phase advance of the focusing lattice can be optimized with respect to the emittance growth along the lattice.

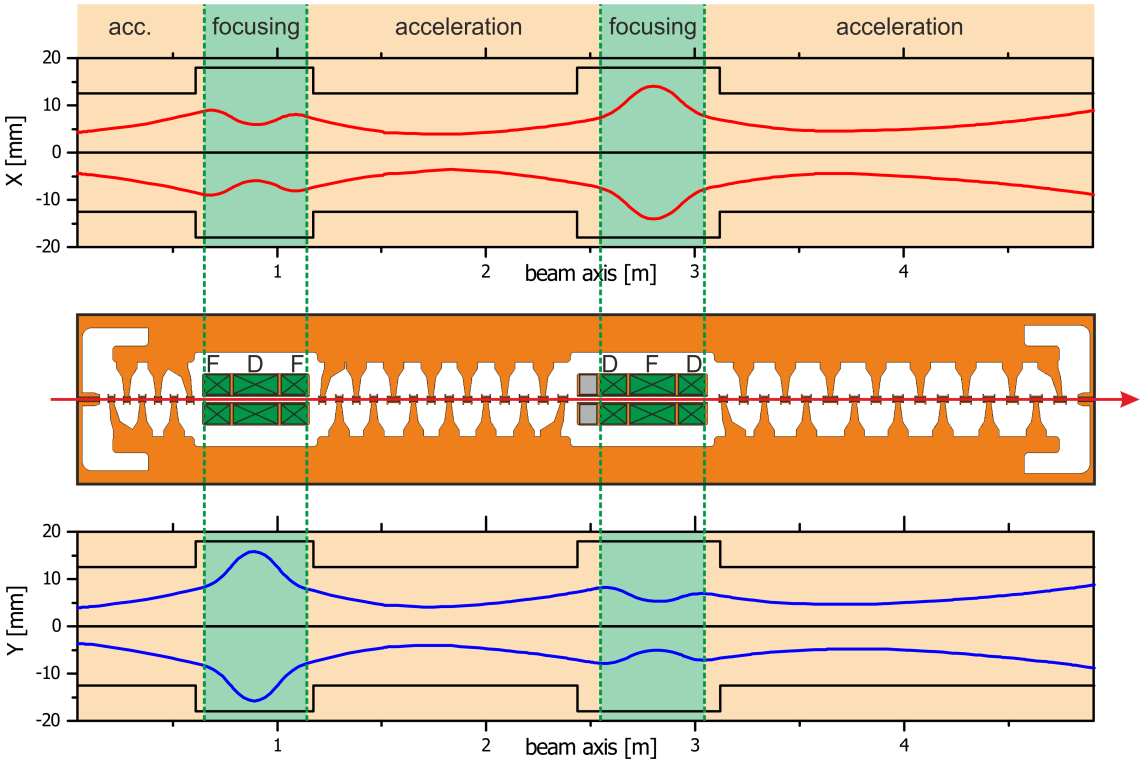

Figure 3.1: Transverse focusing scheme of a KONUS lattice with two lenses in a FDF-DFD lattice.

In Figure 3.2, the longitudinal beam motion relative to the synchronous particle in a KONUS lattice is shown. The energy- and phase-envelopes of the beam are shown relative to the virtual synchronous particle. Additionally, the longitudinal beam envelopes relative to the actual bunch center are shown in Figure 3.3. Each section is generated based on a virtual synchronous particle that has an energy W_s and phase ϕ_s. Therefore the drift lengths between the gap centers resemble the

acceleration of this virtual synchronous particle through the cavity at $\phi_s = 0°$ in the zero degree sections and at a negative phase (e.g. $\phi_s = -35°$) in the rebuncher sections. The structure is designed so that the actual beam has a higher energy than the virtual synchronous particle ($\frac{\Delta W}{W_s} > 0$) in the zero degree sections and the same energy as the virtual synchronous particle in the rebuncher sections. To achieve this, the virtual synchronous particle is redefined at the beginning of each section of a KONUS lattice. This redefinition of the synchronous particle is displayed in the longitudinal envelope plots as a sudden jump in phase and energy.

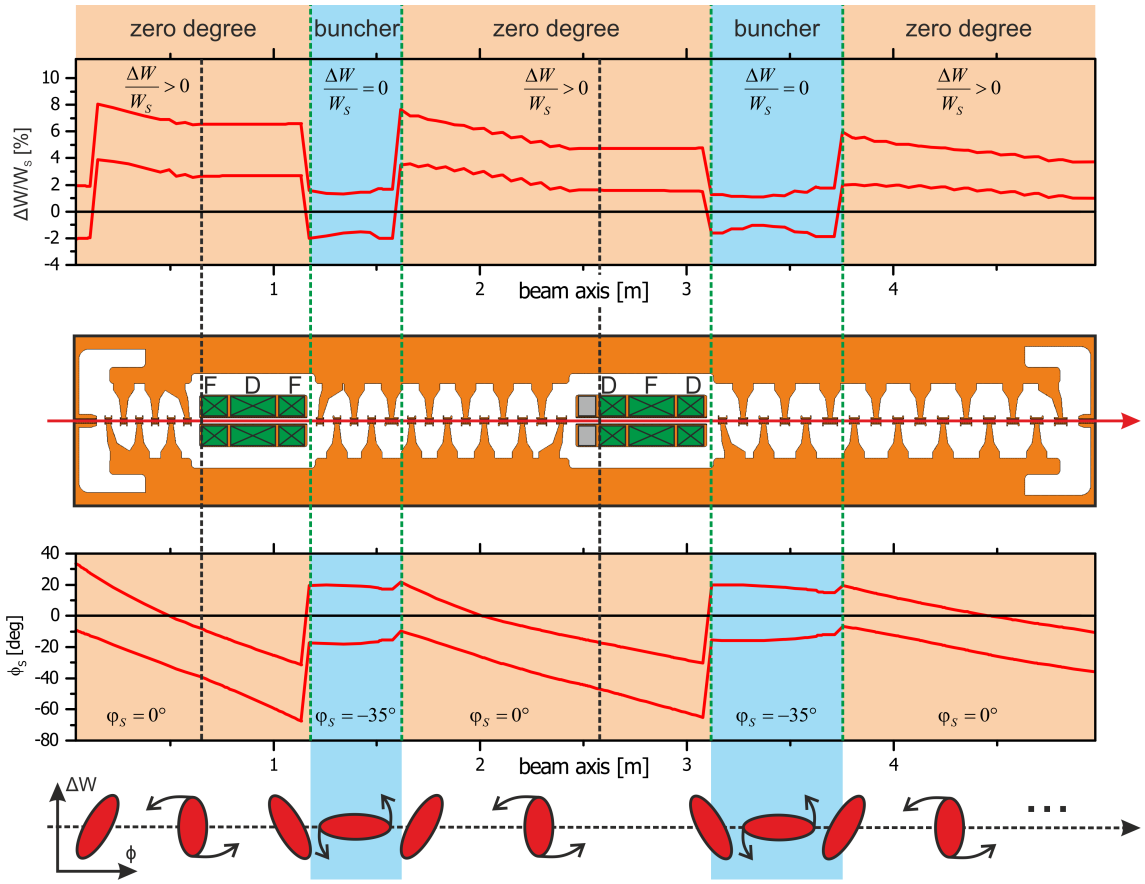

Figure 3.2: Longitudinal beam envelopes of a KONUS lattice. Three zero degree and two rebuncher sections are shown.

The phase jump between a rebuncher and a zero degree section is realized by increasing the drift tube length between the two accordingly. An accelerated beam usually starts with a positive phase close to $\phi_s = 0°$ in the zero degree section while in the rebuncher section the beam center is identical to the synchronous particle. The longitudinal motion in a KONUS lattice is therefore a combination of

the acceleration in the bucket of a negative synchronous phase structure (compare Figure 2.20) and close to the crest at $\phi_s = 0°$ (compare Figure 2.22). However, since the zero degree sections are always short enough to prevent the beam from drifting away into the third and fourth quadrant of the phase space plot for $\phi_s = 0°$, a stable beam motion can be achieved if the sections are matched correctly.

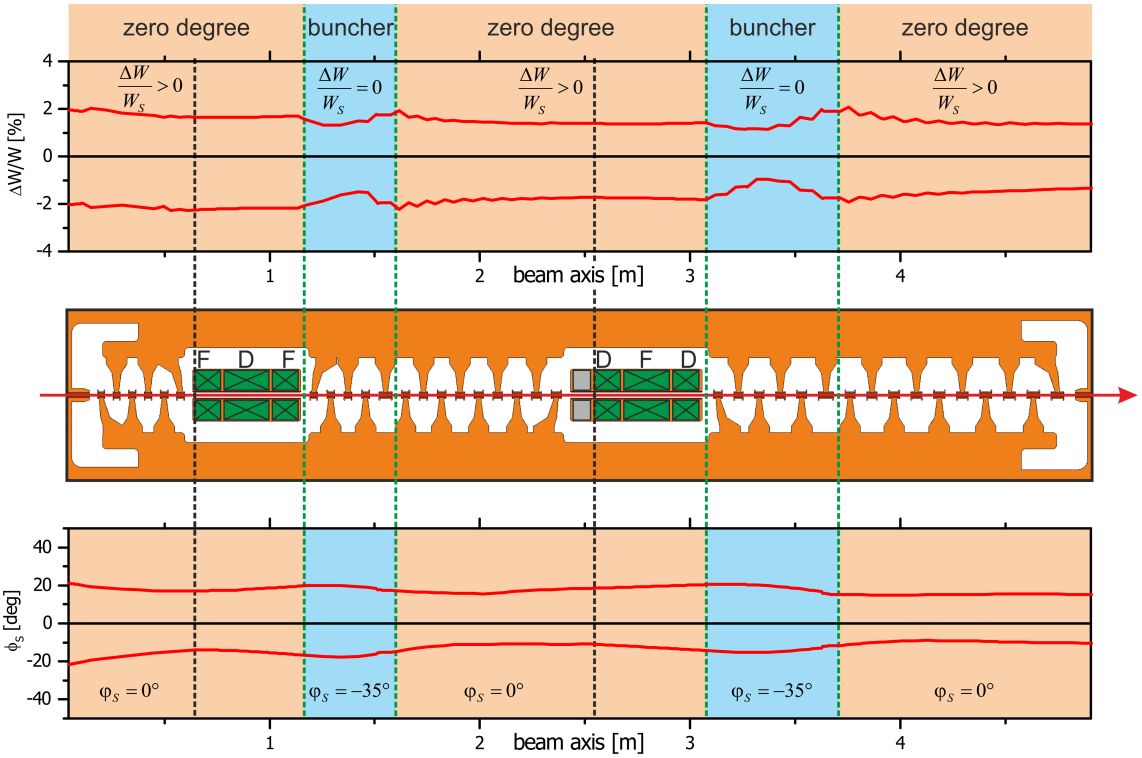

Figure 3.3: Centered longitudinal beam envelopes of a KONUS lattice. Three zero degree and two rebuncher sections are shown.

The bunch center motion for the example of three zero degree and two rebuncher sections is shown in Figure 3.4. Rebuncher sections are not only used to focus the beam longitudinally, but also to match the longitudinal beam to the following zero degree section. A stable beam motion with low emittance growth along a zero degree section is possible if the injected beam has the correct orientation in the longitudinal plane. In general, the beam has to be moderately focused in phase at the injection into a zero degree section. The longitudinal beam motion in a KONUS lattice can be described as follows (see bottom part of Figure 3.2). At the beginning, the beam enters the rebuncher section after drifting through a focusing lens and is therefore defocused at this point. In the following rebuncher gaps the particle beam is sequentially tilted in the longitudinal plane until it has the correct focus for the

injection into the zero degree section. Entering the zero degree section at a phase close to zero, the beam is accelerated with almost no longitudinal focusing. In these first gaps, the highest acceleration efficiency along with minimal RF defocusing is achieved. As the beam progresses in the zero degree section, the phase of the beam shifts to negative phases. Therefore it is being refocused longitudinally towards the end of each zero degree section, while RF defocusing increases.

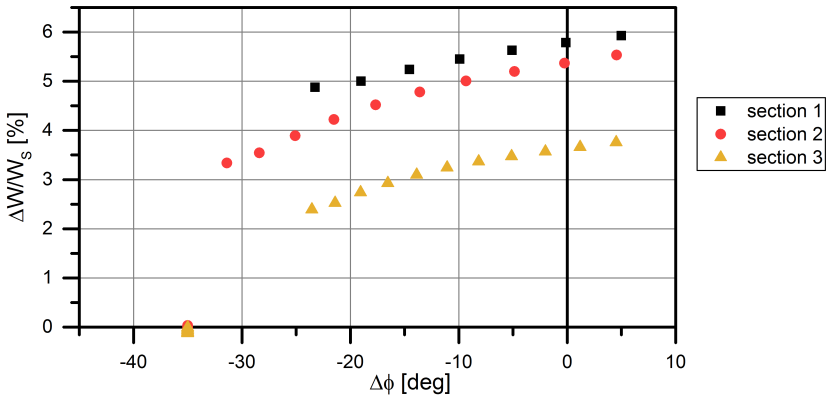

Figure 3.4: Bunch center motion for the example of a KONUS lattice as shown in Figure 3.2.

3.2 Properties of Zero Degree Sections for KONUS

Table 3.1: Simulation parameters for the reference case used in the following parts of Chapter 3.

Particle mass	238 u	Injection Energy W_0	3.91 $\frac{\text{MeV}}{\text{u}}$
Particle charge state	28+	Reference $\Delta W/Ws$	3.22 %
Frequency	108.408 MHz	Reference $\phi_{\text{cp},0}$	5°
Number of gaps	15	Number of particles	10.000
Gap voltage	0.873 MV	Total beam emittance ϵ_0	250 MeV deg
			26.8 $\frac{\text{keV}}{\text{u}}$ns

A detailed investigation of the properties of zero degree sections with injection at energies higher than the virtual synchronous particle was performed for zero current. The simulations were performed with a self-written MATLAB[1] code. This calculation of the individual particle motion is based on the formulas (2.44) and (2.45) from Chapter 2.19. Transverse beam motion is neglected in this model. Writing a dedicated code for these simulations was motivated by the need to be able to investigate all possible iterations of zero degree section input parameters and storing all beam related parameters for each accelerating gap and each particle. Therefore, the code is designed to run thousands of simulations for different structure parameters such as injection phase $\phi_{\text{cp},0}$, excess energy $\Delta W/W_s$ and ellipse orientation Twiss-α. Simulations can be performed for a particle distribution in ϕ and W that is either rectangular or an ellipse. All following simulations in this chapter were performed with an elliptical shape to emulate a particle beam in an accelerator. For the following simulations a reference case was chosen to explore the properties of zero degree sections close to an actual linac design. For this purpose, the fourth zero degree section of the poststripper IH-DTL proposal (Chapter 6) was chosen. The reference particle for the simulations is U^{28+} while the beam current in the following simulations is $I_{\text{beam}} = 0$ emA, neglecting space charge effects. All relevant parameters for the reference case are summarized in Table 3.1. All following simulations in this chapter were performed with these values unless stated otherwise (some parameters are changed during parameter sweeps).

[1] https://de.mathworks.com/products/matlab.html

3.2.1 Injection Matching for Zero Degree Sections

The acceleration of a particle bunch with a bunch center phase ϕ_{cp} close to $\phi_s = 0°$ and an excess energy relative to the structure synchronous particle $W_{\mathrm{cp}} - W_s > 0$ demands careful optimization of the injection parameters. For $\phi_{\mathrm{cp}} = 0°$ the bunch center particle is on the crest of the cosine function of the gap voltage amplitude. Since the particle beam has a certain energy and phase width, there are particles in the bunch that arrive earlier or later than the bunch center. With the bunch center at the crest this means, that late and early particles will be accelerated less than the bunch center, which leads to an increased energy and phase width of the beam. This leads to a "crescent moon" shape of the longitudinal particle distribution. By optimizing the orientation of the injected longitudinal phase space ellipse, this effect can be minimized.

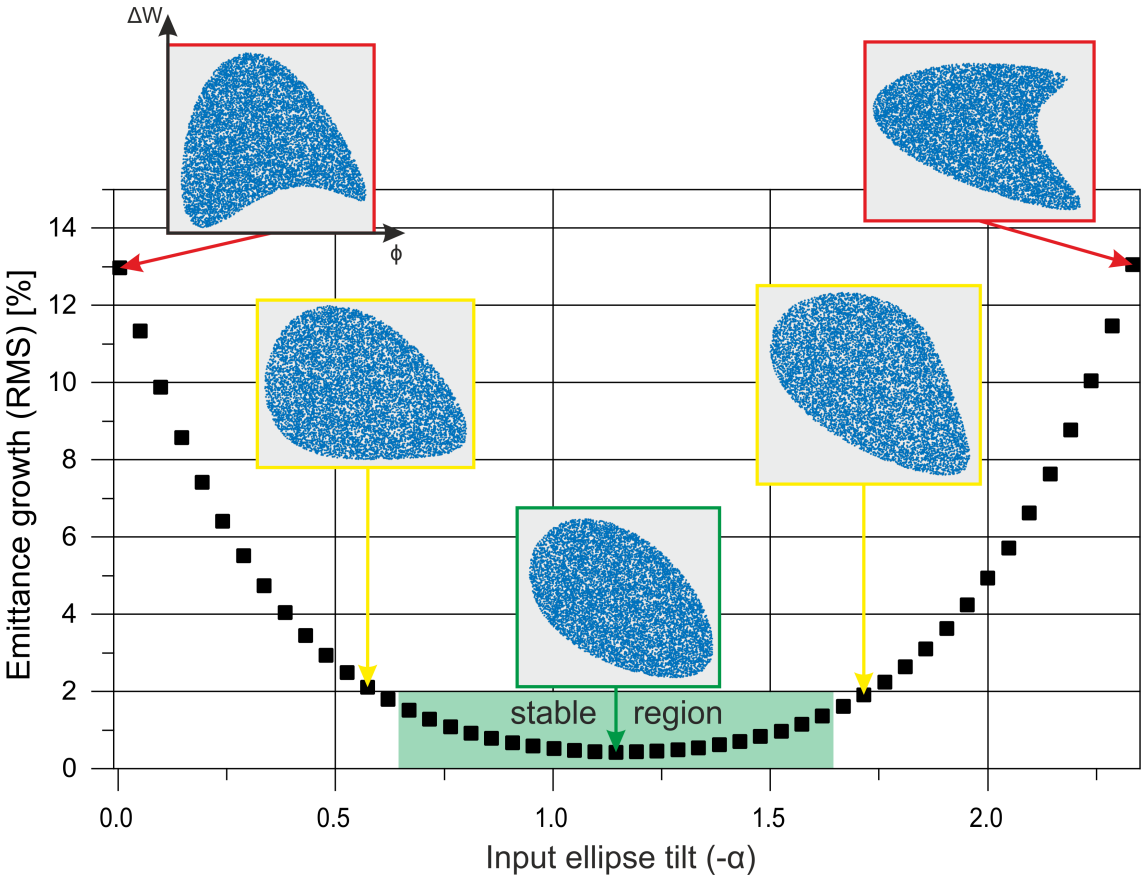

Figure 3.5: Emittance growth for different injection parameter α ($\gamma = \mathrm{const}$) at the beginning of a 15 gap zero degree section with the corresponding output particle cluster plots in the longitudinal plane.

In Figure 3.5 the resulting emittance growth for different orientations of the beam ellipse at the beginning of the lattice is shown along with some exemplary particle distributions at the end of the lattice. If the input beam ellipse is in canonical form ($\alpha = 0$), the output beam is visibly deformed. Three input distributions and the corresponding phase envelopes along the 15 gap section for the most notable cases are shown in Figure 3.6.

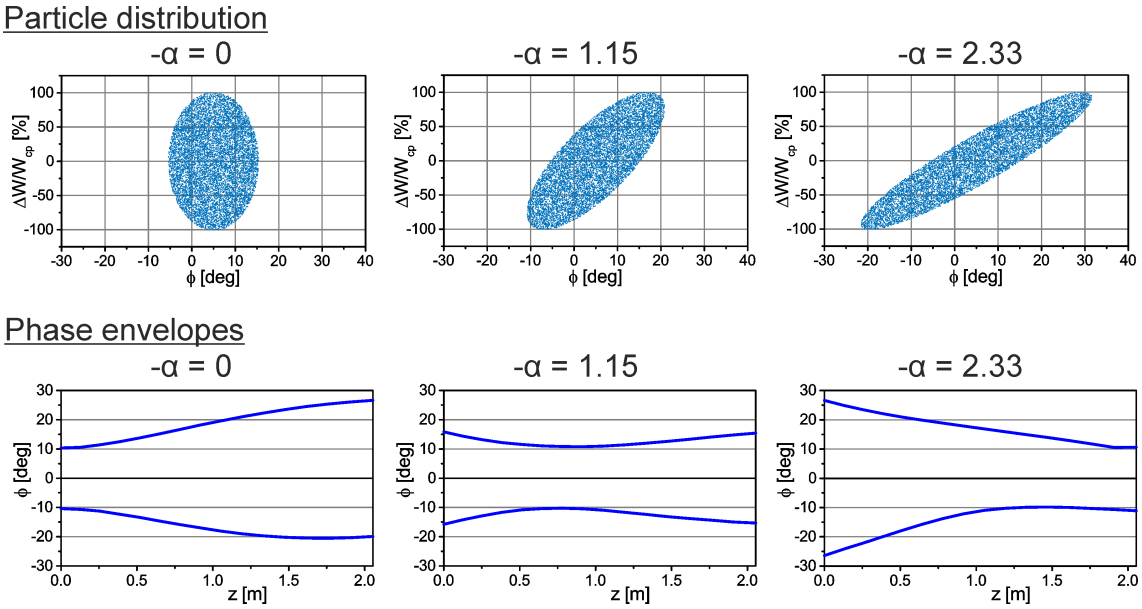

Figure 3.6: Input particle distributions and beam phase envelopes for the three cases $\alpha = 0;\ 1.15;\ 2.33$.

The same is true if the input beam ellipse is tilted too much ($-\alpha > 2$) which means that the beam is wide in phase and the focal point of the phase envelope is close to the end of the structure. In this case, the optimum value $-\alpha = 1.15$ corresponds to a beam where the phase focus is close to the middle of the lattice. From Figure 3.5 it is also clear, that within a certain parameter range (in this case $\sim \alpha_{\mathrm{opt}} \pm 0.5$) the shape of the particle distribution is only slightly deformed. Therefore, if a zero degree section is designed for the optimum Twiss parameters, it has an inherent stability to changing beam parameters. This stability region increases with decreasing beam emittance.

In Figure 3.7, the particle motion of the 15 gap reference section for the optimized case for large and small emittance is shown. The particle distribution is plotted for each gap individually showing the movement of the whole particle bunch in the longitudinal phase space. For each gap, the bunch center is marked with a black

dot. In this optimized case, even the very large emittance of $\epsilon = 250\,\text{MeV deg}$ is accelerated with almost no deformation of the ellipse shape even though the beam fills a large portion of the phase space. For the small emittance of $\epsilon = 18\,\text{MeV deg}$, the beam covers a much smaller phase space area. The optimal beam orientation parameter $-\alpha = 1.15$, however, is the same for both of these extreme cases. In contrast, the same plots are also shown for the mismatched cases $-\alpha = 0$ and $-\alpha > 2$ in Figure 3.8. These plots show how the beam is being deformed during acceleration along the lattice.

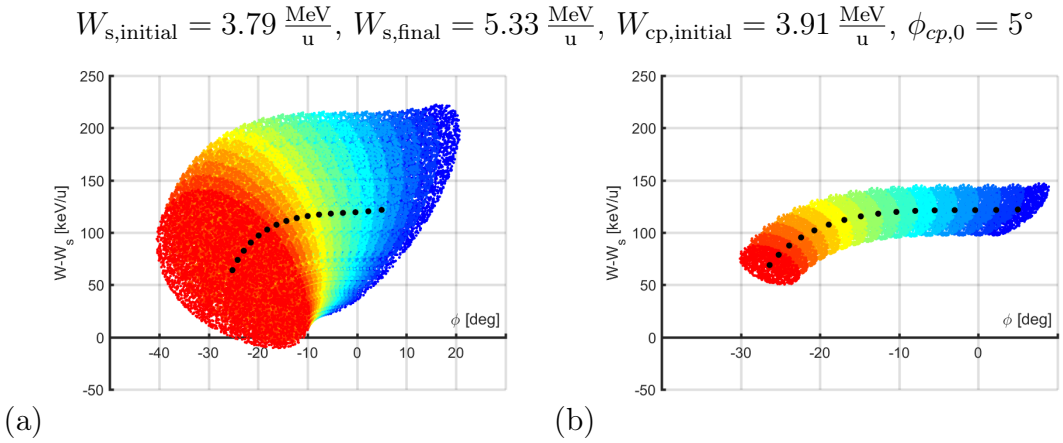

Figure 3.7: Particle distributions of the matched case $-\alpha = 1.15$ for each gap from the input (blue) to the exit (red). For a total longitudinal emittance of $\epsilon_0 = 250\,\text{MeV deg}$ (a) and $\epsilon_0 = 18\,\text{MeV deg}$ (b).

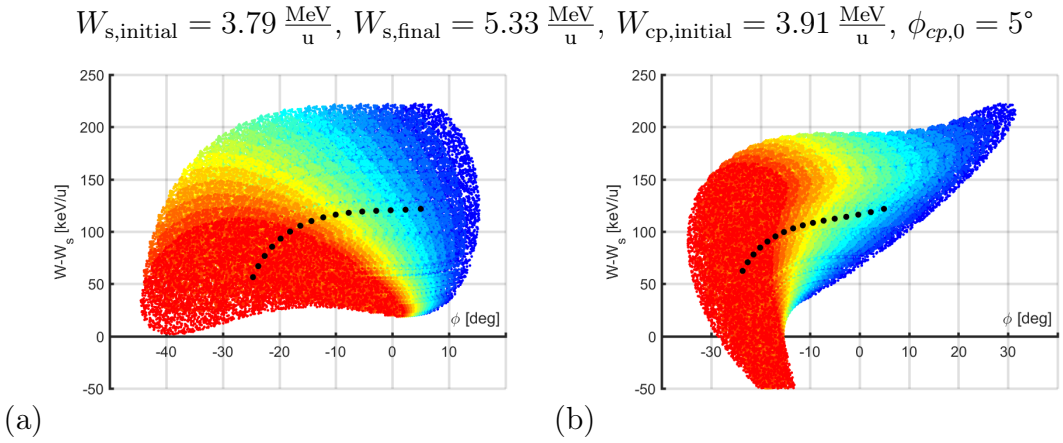

Figure 3.8: Particle distributions of the unmatched cases for each gap from the input (blue) to the exit (red). For a total longitudinal emittance of $\epsilon_0 = 250\,\text{MeV deg}$ with $-\alpha = 0$ (a) and $-\alpha = 2.33$ (b).

3.2.2 Design Parameters

The two parameters that essentially define the geometric structure and beam motion of a zero degree section for a KONUS lattice are the initial energy of the synchronous particle $W_{s,0}$ and the bunch phase at the first gap center $\phi_{\mathrm{cp},0}$. Since the bunch center energy $W_{\mathrm{cp},0}$ of the injected beam is usually a predefined value that is not changed to design the section, the synchronous particle energy parameter can be replaced by the relative excess energy of the injected beam $\frac{\Delta W}{W_s} = \frac{W_{\mathrm{cp}} - W_s}{W_s}$. The energy parameter $\frac{\Delta W}{W_s}$ determines the actual geometric layout since the gap center distances are determined by the virtual synchronous particle. For a given geometry, the initial bunch phase $\phi_{\mathrm{cp},0}$ then defines the path taken by the accelerated beam in the phase space diagram (compare Figure 2.22). These parameters have to be chosen to provide low emittance growth while still delivering a high energy gain to make the best use of the zero degree section acceleration. Simulations were performed by tracking an elliptic particle cluster (same as in Figure 3.7 (a)) for each data point with different $\frac{\Delta W}{W_s}$ and $\phi_{\mathrm{cp},0}$ values. The results are displayed as contour plots of the energy gain and RMS emittance growth for a wide range of the two structure parameters $\frac{\Delta W}{W_s}$ and $\phi_{\mathrm{cp},0}$ in Figure 3.9 and 3.10.

For the reference 15 gap section the energy gain for a wide range of parameters is shown in Figure 3.9 (a). The white rectangle marks a small area that is considered for a KONUS zero degree section in this case. Parameters in this range lead to particle motion that is mostly confined to the second quadrant of the longitudinal phase space plot. The highest energy gain achievable is contained within this region in the lower right corner (see Figure 3.9 (b)). In Figure 3.10 (a), the resulting

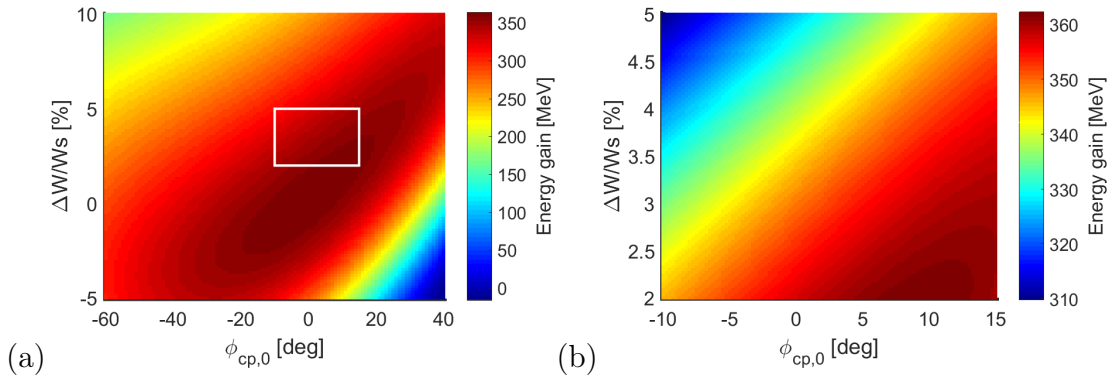

Figure 3.9: Energy gain with different structure parameters for a wide parameter range (a) and the white rectangle zoom in (b).

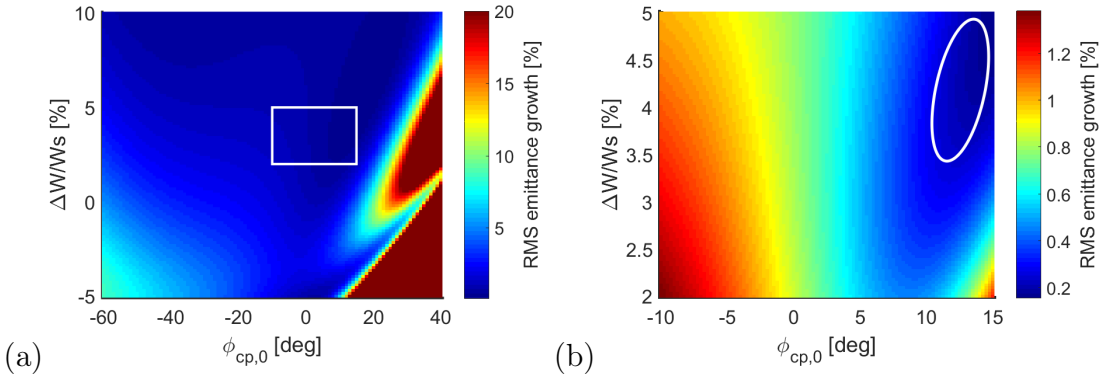

Figure 3.10: RMS emittance growth with different structure parameters for a wide parameter range (a) and the white rectangle zoom in (b). Dark red areas in (a) are $\geq 20\,\%$.

RMS emittance growth for the wide range of parameters is shown, which indicates that the design range (white rectangle) is within a region of low emittance growth. From the emittance growth plot also the parameter limits for stable beam motion are clearly visible as the dark red areas towards the right side of the graph, where the emittance growth increases rapidly. The usual design range for KONUS zero degree sections however is well outside this region of high emittance growth. A more detailed view of the relevant design region is shown in Figure 3.10 (b). An area of minimal emittance growth in the design region already gives a clue towards a possible ideal injection area which is marked by a white ellipse in Figure 3.10 (b).

Table 3.2: Structure parameters of IH-DTL KONUS designs for different applications [31, 5, 32].

GSI HSI		Poststripper IH-DTL		GSI proton linac	
$\frac{A}{q} = 65$		$\frac{A}{q} = 8.5$		$\frac{A}{q} = 1$	
$I_{\text{bunch}} = 18\,\text{emA}$		$I_{\text{bunch}} = 45\,\text{emA}$		$I_{\text{bunch}} = 75\,\text{pmA}$	
U^{4+}		U^{28+}		p+	
36.136 MHz		108.408 MHz		325.244 MHz	
$W_{\text{in}}\,[\frac{\text{MeV}}{\text{u}}]$	$0.12 - 1.14$	$W_{\text{in}}\,[\frac{\text{MeV}}{\text{u}}]$	$1.4 - 9.8$	$W_{\text{in}}\,[\frac{\text{MeV}}{\text{u}}]$	$3 - 59$
$\phi_{\text{cp,0}}$	5° to 19°	$\phi_{\text{cp,0}}$	5° to 7°	$\phi_{\text{cp,0}}$	3° to 18°
$\frac{\Delta W}{W_s}$	2 to 6 %	$\frac{\Delta W}{W_s}$	2 to 6 %	$\frac{\Delta W}{W_s}$	2 to 10 %

Some typical design parameters for different particle energies of several KONUS designs from protons to uranium are compiled in Table 3.2. Usually, a KONUS design starts off with a high relative excess energy in the first sections which is then reduced gradually along the linac for each section. This is necessary to keep the beam traveling towards roughly the same negative synchronous phase at the end of each section. A stable beam motion over long distances can be achieved this way.

4 GSI UNILAC and FAIR

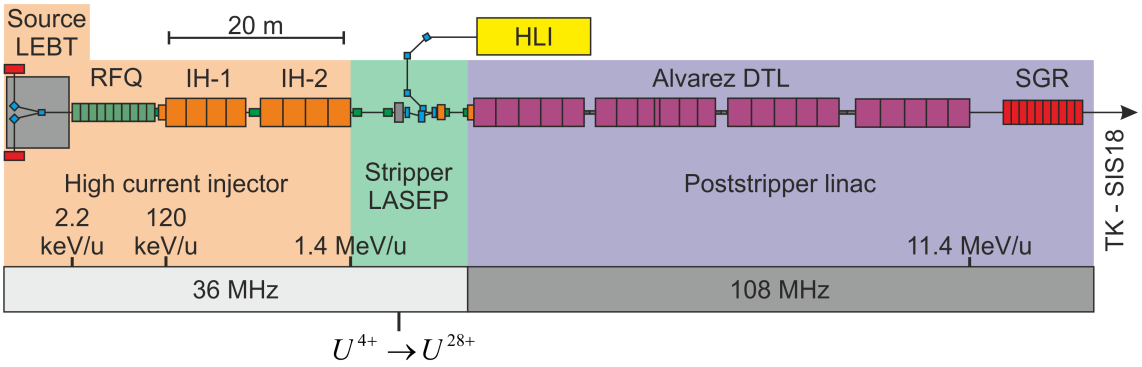

Figure 4.1: Layout of the UNILAC showing the different lengths of the existing Alvarez-DTL and the proposed new IH-DTL.

The "Universal Linear Accelerator", called UNILAC, is a normal conducting heavy ion linac that can accelerate all elements up to uranium to more than 15 % the speed of light. In Figure 4.1 the general layout of the UNILAC is shown. Two ion source terminals ("north terminal" and "south terminal") with various types of ion sources generate a wide range of ion beams for the UNILAC. For most beam dynamics simulations, the reference particle for high current ion beams in the UNILAC is uranium. The particle energy behind the source is 2.2 $\frac{\text{keV}}{\text{u}}$. For uranium beams, the U^{4+} species is produced. Following the ion source, the beam is transported through the low energy beam transport section LEBT and matched to the following RFQ. The RFQ is a 9 m long IH-type RFQ that accelerates the beam up to 120 $\frac{\text{keV}}{\text{u}}$ [20]. A medium energy beam transport section MEBT then provides the transverse and longitudinal matching to the following IH-DTL cavities. This MEBT consists of a magnetic quadrupole doublet lens and a so called Superlens, which is a short 11-cell RFQ that is operated as a buncher [3]. The following IH-DTL consists of two tanks (IH-1 and IH-2) with a total voltage of 91 MV that increase the beam energy to 1.4 $\frac{\text{MeV}}{\text{u}}$. This first part of the UNILAC from the ion source to the end of the second IH-type cavity is called the high current injector HSI [31, 33]. It provides high

current ion beams at a low duty factor. To increase the acceleration efficiency, the beam is stripped at 1.4 $\frac{\text{MeV}}{\text{u}}$ with a gas stripper to a much higher charge state (for uranium from U^{4+} to U^{28+}) [34]. Behind the stripper the generated charge states are separated by a charge state separator which consists of two 15° and one 30° bending dipoles. Charge state separation is achieved by their different trajectories in the dipoles. An Alvarez DTL is the final acceleration stage of the UNILAC, which accelerates the beam to a final energy of 11.4 $\frac{\text{MeV}}{\text{u}}$. At this energy the beam can be injected into the SIS18 synchrotron. Behind the Alvarez DTL there are additional single gap resonators for adjustment of the final beam energy for experiments that directly use the UNILAC beam. In addition to the HSI, the UNILAC also has a second injector for high duty factor low current beams of highly charged ions, which is called the high charge state injector HLI. The proton beam for FAIR will be provided by a 70 mA dedicated proton linac [32].

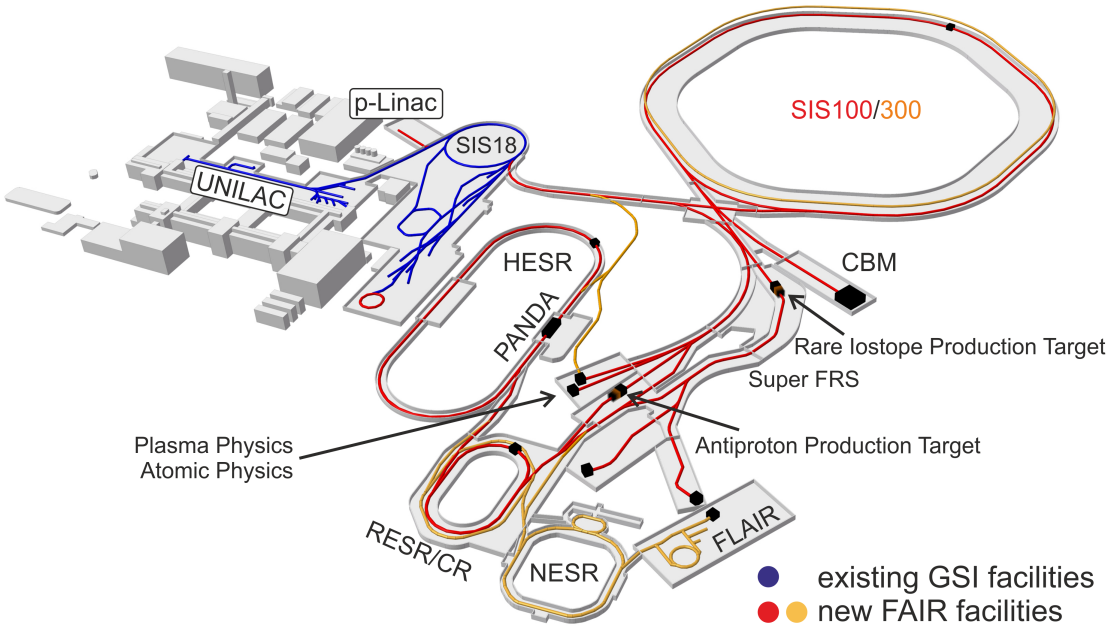

Figure 4.2: Layout of the GSI with new FAIR complex (courtesy of FAIR/GSI).

The new "Facility for Antiproton and Ion Research" FAIR at the GSI site will expand the existing accelerator structure by five new circular accelerators and a large number of new experiments (see Figure 4.2). Planned experiments for FAIR are grouped in four categories namely APPA, CBM, NuSTAR and PANDA. As a first stage, the existing SIS18 synchrotron will accelerate protons from 70 MeV to

4 GeV and heavy ions (U^{28+}) from 11.4 $\frac{\text{MeV}}{\text{u}}$ to 0.2 $\frac{\text{GeV}}{\text{u}}$. Following the SIS18, the next acceleration stage will be the new SIS100 synchrotron. It has a circumference of 1083.6 m and the beam rigidity is 100 Tm. Protons will be accelerated from 4 GeV to a final energy of 29 GeV in the SIS100. Heavy ions (U^{28+}) will be accelerated from 0.2 $\frac{\text{GeV}}{\text{u}}$ to a final energy of 2.7 $\frac{\text{GeV}}{\text{u}}$. The goal for FAIR operation is to provide $4 \cdot 10^{13}$ protons and $5 \cdot 10^{11}$uranium ions per pulse for experiments [1, 35].

4.1 UNILAC Beam Requirements for FAIR

To achieve the high heavy ion intensities necessary for FAIR, the UNILAC has to provide unprecedented beam currents. With the reference ion U^{28+}, the mass to charge ratio is $\frac{A}{q} = 8.5$ for the poststripper linac of the UNILAC. The beam requirements for injection into the SIS18 are summarized in Table 4.1 as defined in the Baseline Technical Report [1]. The beam is injected into the SIS18 synchrotron by multi-turn injection to fill the transverse acceptance with $100 - 200\,\mu\text{s}$ beam pulses from the UNILAC [36] at a low duty cycle.

Table 4.1: Parameters for the U^{28+} beam behind the poststripper linac for SIS18 injection [1].

Parameter	FAIR requirement
Beam current	15 emA
Beam energy	11.4 $\frac{\text{MeV}}{\text{u}}$
Total number of ions	$2.7 \cdot 10^{11}$
Transverse 90 % emittance	$7\,\pi$ mm mrad
Normalized emittance	1.1 mm mrad
Macro pulse length	$100 - 200\,\mu\text{s}$
Repetition rate	2.7 Hz

4.2 Multi-Turn Injection

Since the emittance of the injected linac beam is much smaller than the available phase space of the synchrotron, a multi-turn injection scheme is used. While the horizontal beam emittance of the UNILAC is in the order of $5 - 10\,\text{mm mrad}$, the available horizontal phase space of the SIS18 synchrotron is 150 mm mrad, this is called the acceptance. In general, the beam is injected into the synchrotron by bending its trajectory using an electrostatic septum until it coincides with the synchrotron beam path. This beam path however is displaced from the ideal beam path in the synchrotron by using so called dipole bumper magnets (see Figure 4.3). The key mechanism of multi-turn injection is, that this displacement x_{disp} of the synchrotron beam is slowly reduced during the injection of the linac beam, while the injected beam trajectory is not changed. This way, when the synchrotron beam has circled around to the injection point, the injected beam will not collide with the beam already stored in the synchrotron. In addition to this, the focusing lattice of the synchrotron is set in such a way, that the horizontal angle of the stored beam at the injection point differs from the injected beam trajectory. Therefore, it is possible to fill the horizontal phase space of the synchrotron with multiple turns of the injected linac beam.

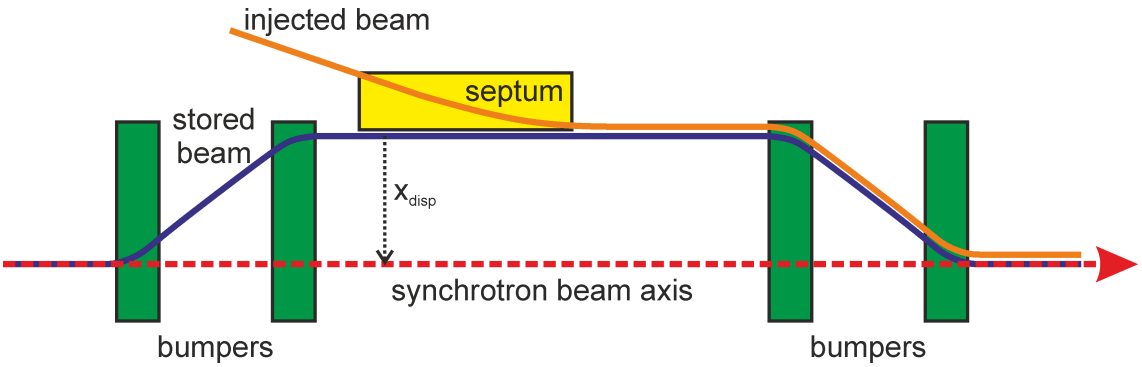

Figure 4.3: Sketch of the multi-turn injection using bumper magnets and an electrostatic septum.

For the example of FAIR operation, the injection of U^{28+} at an energy of 11.4 $\frac{\text{MeV}}{\text{u}}$ into the SIS18 is foreseen. In this case, the beam revolution time τ in the SIS18 is $\tau = 4.7\,\mu\text{s}$. A maximum number of allowed turns for the injection is estimated by

$$N_{\text{turn}} = \frac{A_x}{\epsilon_x} = \frac{150\,\text{mm mrad}}{\epsilon_x}, \tag{4.1}$$

where A_x is the horizontal acceptance of the synchrotron and ϵ_x is the horizontal emittance of the injected beam. In reality, however, the actual number of turns possible for a given beam emittance is smaller. This is due to the fact, that because of the packing problem, it is not possible to fill the full phase space with the injected beam. The number of injected ions during a loss-free multi-turn injection can be calculated by

$$N_{\mathrm{part}} = \frac{I_{\mathrm{linac}}}{q} \cdot N_{\mathrm{turn}} \cdot \tau, \tag{4.2}$$

with I_{linac} being the beam current of the injector linac and q being the charge of the injected ions. For SIS18, the maximum number of turns is estimated to $N_{\mathrm{turn}} = \frac{150\,\mathrm{mm\ mrad}}{7\,\mathrm{mm\ mrad}} \approx 21.4$. Therefore, a linac beam with a beam current of $I_{\mathrm{linac}} = 15\,\mathrm{mA}$ within an emittance of $\epsilon_x = 7\,\mathrm{mm\ mrad}$ would result in $N_{\mathrm{part}} = \frac{15\,\mathrm{mA}}{28e} \cdot 21 \cdot 4.7\,\mu\mathrm{m} = 3.3 \cdot 10^{11}$. Consequently, the original design value of $2.7 \cdot 10^{11}$ particles injected into SIS18 [1] can be achieved with just 17 turns. This would correspond to a total injection time of 80 µs. Assuming almost loss-free injection of the SIS18 beam into the new SIS100, a total particle number of $1 \cdot 10^{12}$ is reached in SIS100 when four SIS18 spills are injected. Further considerations in combination with simulated particle distributions can be found in Chapter 6.2.2.

5 MEBT Upgrade

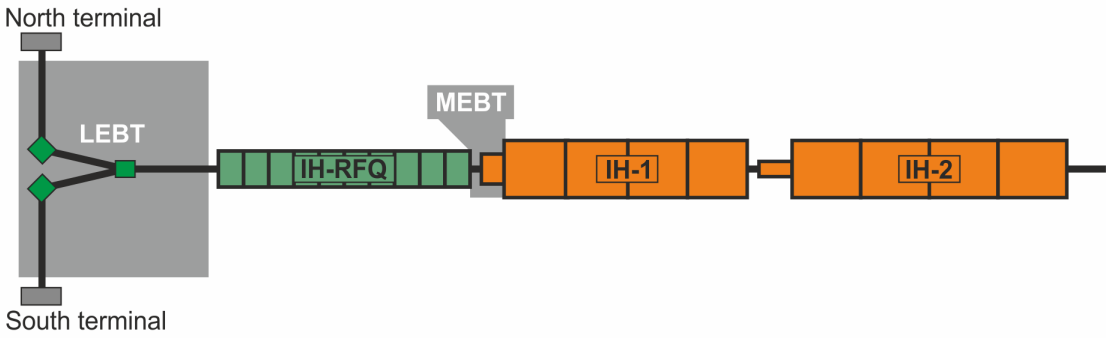

Figure 5.1: Sketch of the existing High Current Injector at GSI UNILAC.

In this section a conventional matching section is proposed as replacement for the existing medium energy beam transport section (MEBT) of the GSI UNILAC (see Figure 5.1). An upgrade is necessary to reach the high beam current of 18 mA required for FAIR operation. This requirement might be relaxed due to the development of a much more efficient gas stripper based on a pulsed H_2 jet [37]. However, until now the highest achieved current behind the HSI is 8.7 emA U^{4+} (6 emA reported in [37]). Measured losses in the existing MEBT and IH-DTL at these high currents are in the order of 20 %. This shows the importance of eliminating bottlenecks in the HSI, which can be achieved with a new matching section. In the following, both the existing MEBT and the new MEBT section will be described. Simulations showing the limitations of the existing Superlens will be shown. Furthermore, simulations for the new MEBT design will be described in detail and a comparison of the two designs is presented.

5.1 Existing Superlens MEBT

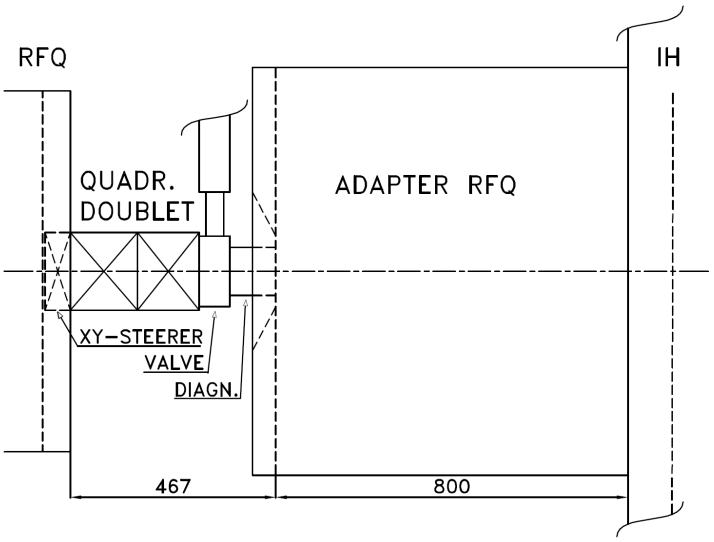

Figure 5.2: Layout of the existing Superlens MEBT of the GSI High Current Injector [3].

The existing MEBT consists of a quadrupole doublet lens followed by a so called "Superlens" which is a ten cell RFQ operated at -90° phase for transverse and longitudinal focusing [3, 31]. It was the first 3D focusing lens built for a linear accelerator. In Figure 5.2, the layout of this 1.4 m long Superlens MEBT is shown. The working principle of the Superlens is illustrated in Figure 5.3, where the transverse and longitudinal beam envelopes for a uranium beam are shown as they pass the MEBT. In Figure 5.3(a) the beam is first focused by the quadrupole doublet lens and then the periodic focusing of the Superlens RFQ follows. In Figure 5.3(b) the ability of the Superlens to also focus the beam in phase along with transverse focusing is shown. Even though this 3D focusing lens provides compact matching between the RFQ and the IH-DTL, it also restricts the flexibility of this section. In the Superlens, all three planes x,y and z are coupled and therefore focusing can only be changed by one parameter, the inter-vane voltage. Consequently, if transverse and longitudinal input of the matching section change independently, correct matching to the IH-DTL can not be preserved. In 2008/2009 the RFQ of the UNILAC was upgraded by replacing the modulated rods with a new design, based on improved beam dynamics [2]. The aim of this upgrade was to increase the acceptance of the RFQ and allow higher beam currents with improved transmission.

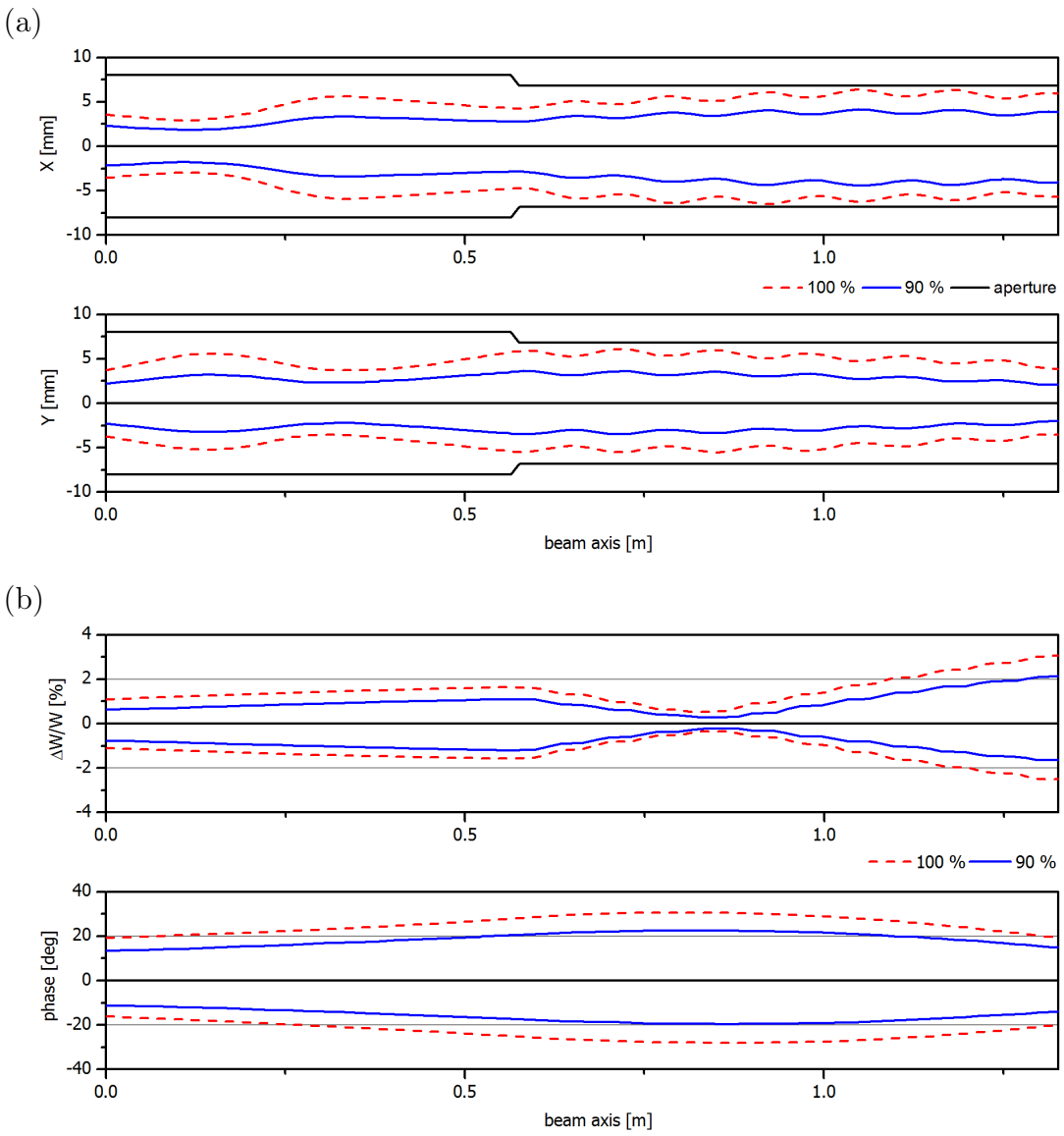

Figure 5.3: Beam envelopes of the Superlens MEBT in the transverse plane (a) and the longitudinal plane (b). Based on the initial RFQ design from 1996 [31, 38].

With this upgrade, the beam output parameters of the RFQ changed. Due to the increased divergence of the beam in both transverse planes, the existing matching section becomes a bottleneck for the beam and significant losses occur in the doublet lens and the Superlens RFQ. Additionally, the quality of matching to the following IH-DTL is decreased. Therefore, a new matching section was designed to provide optimal matching for the new RFQ and improve operational flexibility in case of future RFQ alterations.

5.1.1 Limitations of the Superlens MEBT

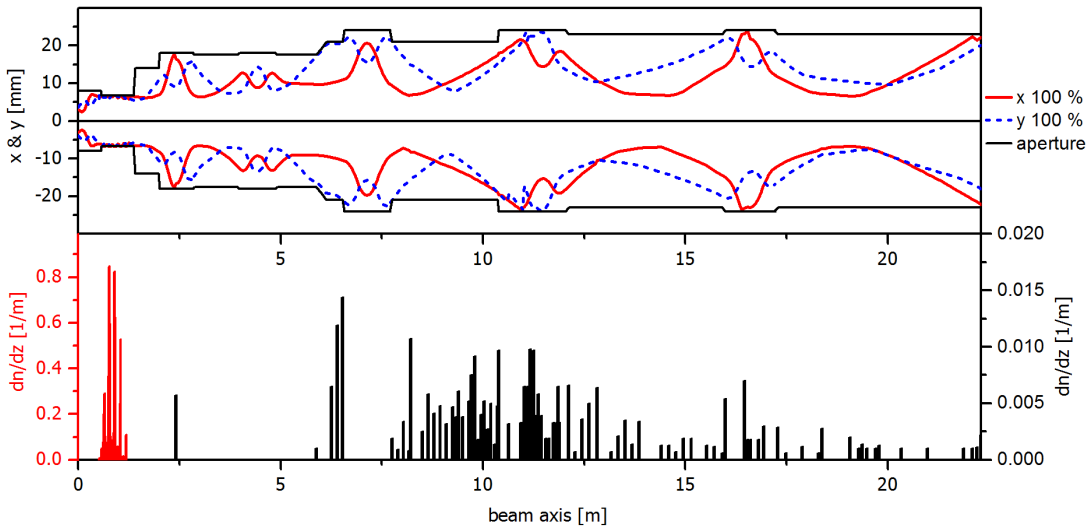

Figure 5.4: Distribution of losses for the Superlens MEBT and IH1+2 of the HSI. Top: 100 % beam envelopes in x and y; bottom: Particle losses dn/dz on two different scales for the Superlens and IH-DTL.

The Superlens MEBT was designed for the original HSI RFQ [20]. Particle output distributions for the original 1996 RFQ and the upgraded 2009 RFQ are shown in Figure 5.5 and Figure 5.6, respectively. Comparing the two, the most notable difference is a larger emittance for the new RFQ and a large difference in the longitudinal orientation of the beam. Additionally, a significant increase of divergence in the $x - x'$ plane is obvious. This leads to significant losses in the Superlens due to the small aperture of the Superlens rods and insufficient focusing of the quadrupole doublet. The following calculations to investigate those bottlenecks were performed with the simulated output distribution of the 2009 RFQ [2]. For a 20.75 mA U^{4+} beam, the transmission of the Superlens is only 90.45 %, overall transmission behind the IH-DTL is 87.60 %. In Figure 5.4 the distribution shows that the majority of losses occur within the Superlens when particles hit the rods. In addition, further losses in the HSI IH1 and IH2 occur due to a transverse and longitudinal mismatch of the beam. Emittance growth in the HSI is increased compared to the original design due to the mismatch between RFQ and IH-DTL. The output emittances for 18 emA and 20.75 emA U^{4+} are summarized in Table 5.1. Significant emittance growth occurs already in the Superlens section in all three planes and continues in the IH-DTL. A clear indicator for longitudinal mismatch is the emittance blow up

in the IH-DTL in the longitudinal plane from 0.3 to 1.7 $\frac{\text{keV}}{\text{u}}$ns. Due to these obvious limitations of the existing MEBT section, especially with regard to unprecedented high current operation for FAIR, a new matching section was designed to provide improvement in transmission, emittance growth and operational flexibility for the whole HSI.

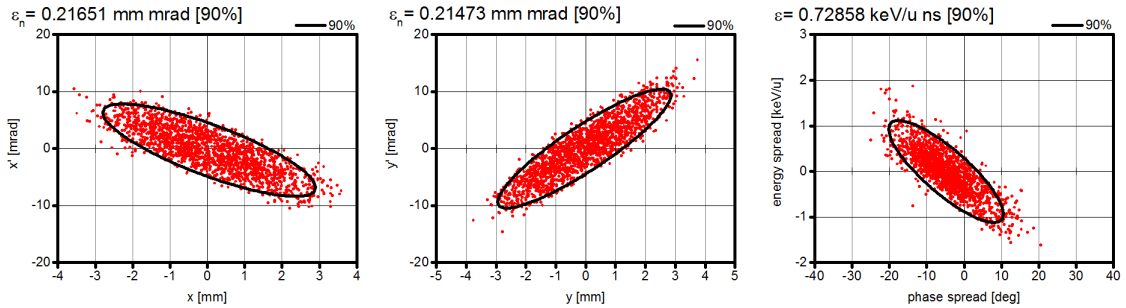

Figure 5.5: Simulated particle output distribution for the original HSI RFQ as built in 1996 (1789 macroparticles).

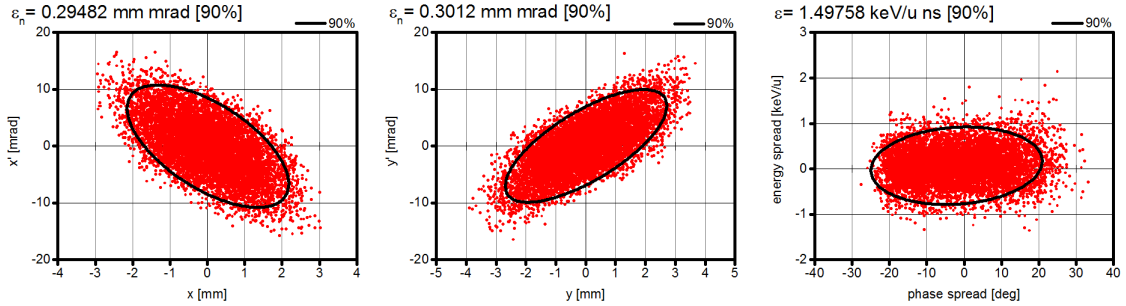

Figure 5.6: Simulated particle output distribution for the upgraded HSI RFQ after the upgrade in 2009 (8300 macroparticles).

Table 5.1: Simulation results for the Superlens MEBT with and without the subsequent IH-DTL tanks. The 2009 RFQ distribution is used.

U^{4+}Beam current [mA]		20.75	18	20.75	18
Output of	**2009 RFQ**	**Superlens**		**IH 2**	
Transmission [%]		90.45	92.64	87.60	89.70
$\epsilon_{\text{n,rms}}$ $x - x'$ [mm mrad]	0.066	0.112	0.107	0.181	0.175
$\epsilon_{\text{n,rms}}$ $y - y'$ [mm mrad]	0.069	0.093	0.090	0.158	0.162
ϵ_{rms} ϕ-W [$\frac{\text{keV}}{\text{u}}$ns]	0.325	0.362	0.354	1.371	1.667

5.2 Layout of the new MEBT Section

A new MEBT has been developed in this work motivated by the drawbacks of the existing design, as mentioned in the preceding section. The new MEBT consists of two magnetic quadrupole triplet lenses, a two gap 36 MHz buncher and an xy-steerer behind the RFQ (see Figure 5.7). Additional drift space for beam diagnostics and a vacuum valve is also taken into account. The positions of the quadrupoles, the buncher cavity and the additional drift spaces were optimized to provide optimal matching to the IH-DTL. By reducing the design to four types of quadrupoles instead of six as previously published in [4] by the author of this work, only four power supplies are needed for the lenses and only four types of quadrupoles will have to be built. This reduces production cost while keeping the original performance of the design.

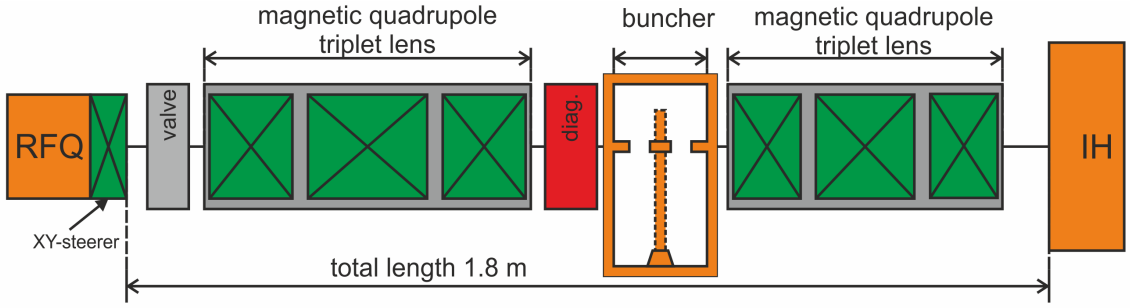

Figure 5.7: Sketch of the new MEBT section for the UNILAC HSI.

The quadrupoles are designed for a maximum gradient of 91.5 T/m which corresponds to 1.1 T at the pole tip for an aperture radius of 11 mm + 1 mm beam pipe. By using a spiral buncher cavity, the diameter of the buncher cavity at 36 MHz will only be around 0.5 m. Mechanical and operational parameters of the new MEBT section are summarized in the following Table 5.2. The total length of the new MEBT section is 1.8 m, which is 40 cm longer than the existing Superlens MEBT. Therefore, the IH-DTL following the MEBT has to be moved down on the beamline to make room for the new MEBT. The feasibility of this was confirmed by internal investigations at GSI. A detailed magnet design was already developed at GSI and the buncher specifications were agreed upon. The specifications were finalized in cooperation with GSI Darmstadt and are ready for tendering as of February 2016.

Table 5.2: Parameters for the new MEBT section.

Total length	1.8 m	
	Triplet 1	**Triplet 2**
Effective length [mm]	160 / 230 / 160	130 / 190 / 130
Aperture diameter [mm]	22	22
Effective gradient [T/m]	91.5 / 91.5 / 85	91.5 / 91.5 / 89
Integrated gradient [T]	14.64 / 21.045 / 13.6	11.9 / 17.39 / 11.57

Buncher Cavity	
Length [mm]	200
Aperture Diameter [mm]	1.66
RF Frequency [MHz]	36.136
Period Length [mm]	66.6
Number of Gaps	2
Effective Gap Voltage [kV]	225
On Axis Field [MV/m]	6.08

5.2.1 Simulation Results

The MEBT was designed in LORASR [39, 23] using a Waterbag distribution modeled after the 2009 output distribution. It was generated by using the Twiss parameters and RMS emittances from the simulated RFQ distribution. RMS emittances and also 90 % emittances of the generated Waterbag distribution are very similar to the original distribution. This shows, that a Waterbag distribution is a reasonable assumption for modeling the RFQ output beam. Simulations with the design distribution show no losses for the MEBT and IH-DTL. Overall, simulation results with the Waterbag distribution and the simulated RFQ distribution agree well.

The following simulations of the new MEBT were performed for 18 mA U^{4+}, which is the requirement for FAIR operation of the HSI [1]. Figure 5.8 (a) shows the transverse envelopes of the MEBT section. At the entrance of the IH-DTL, the beam is converging in $x - x'$ and slightly diverging in $y - y'$. This corresponds to the matching conditions of the original design of the IH-DTL [40].

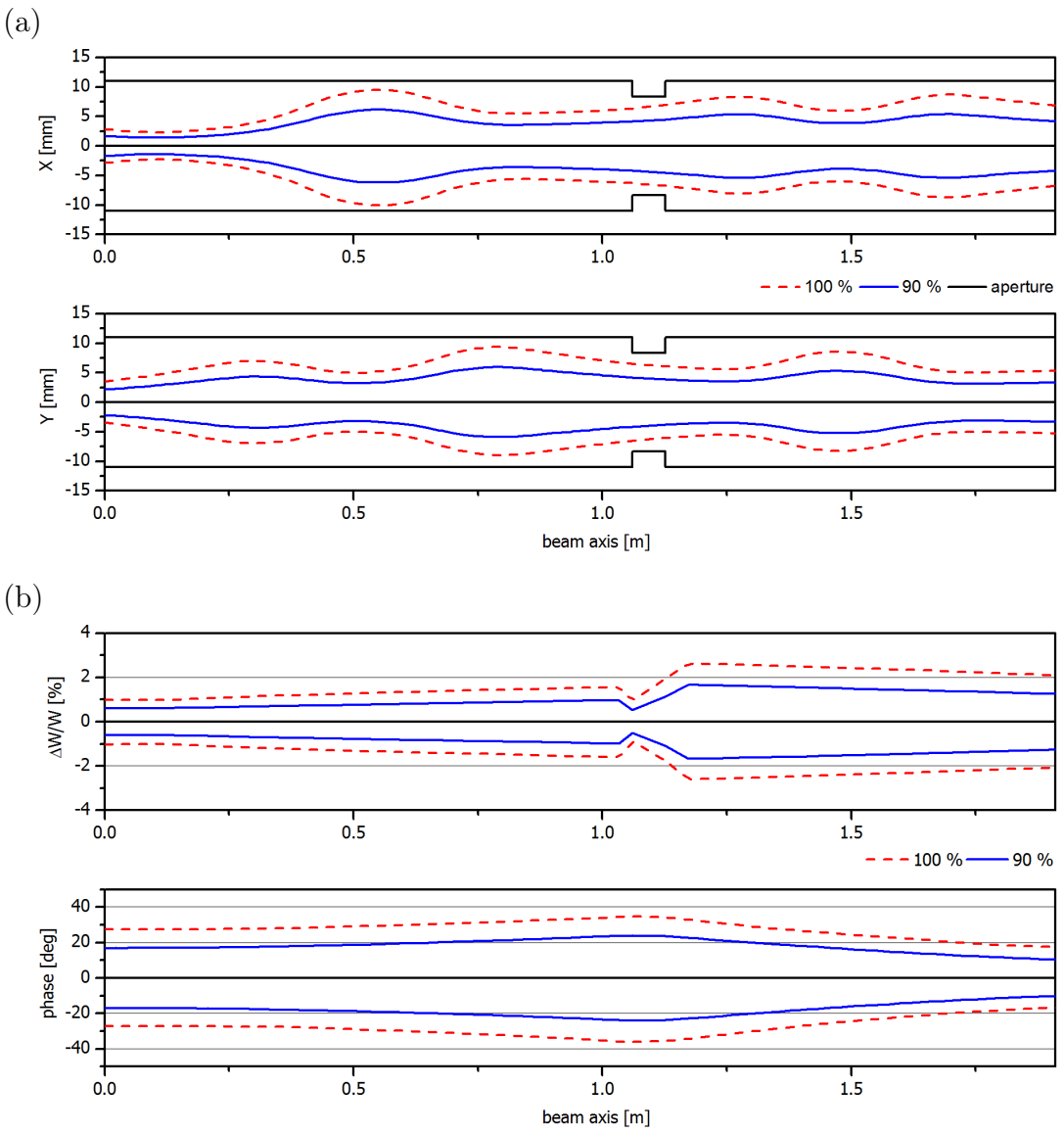

Figure 5.8: Beam envelopes of the MEBT section in the transverse plane (a) and the longitudinal plane (b).

Since the new MEBT has two triplet lenses and a buncher instead of only one doublet lens and a Superlens as the existing section, a higher flexibility with respect to the RFQ output is provided. Additional flexibility is gained since in this design the transverse and longitudinal focusing are separated and can therefore be tuned independently. The longitudinal beam envelopes in Figure 5.8(b) show how the buncher works to focus the beam phase and energy, matching the requirements of the following IH-DTL. To achieve the optimum matching conditions, the position of the buncher was shifted and the buncher voltage was varied. The presented setup

is the result of this optimization to best fit the IH-DTL input acceptance in the longitudinal plane. This optimized matching scheme of the new MEBT significantly improves the beam dynamics in the IH-DTL. Using the Waterbag design distribution, full transmission in the MEBT and also the following two IH-DTL tanks was achieved.

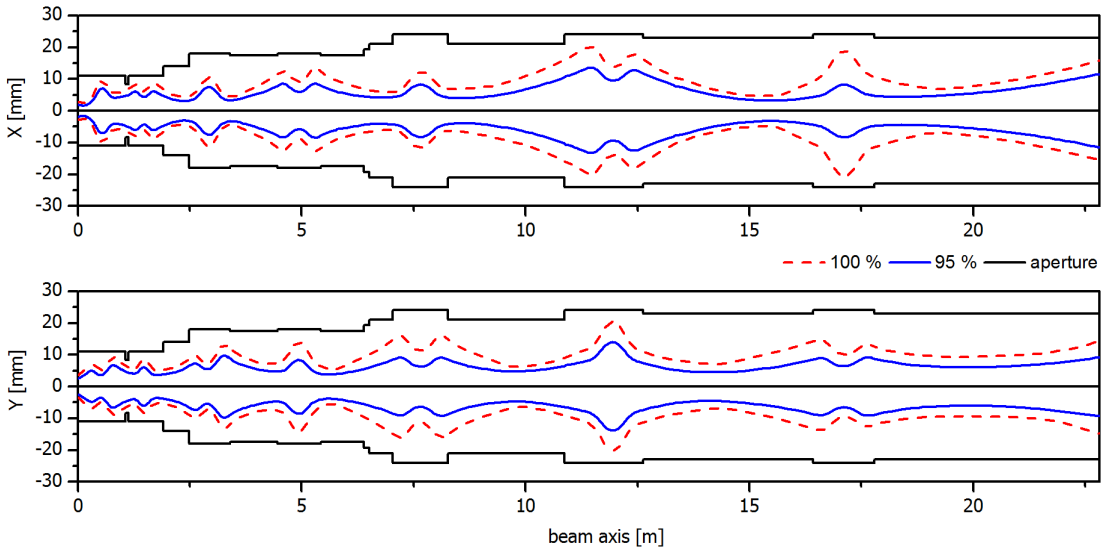

Figure 5.9: Transverse beam envelopes for the HSI IH-DTL with the new MEBT section for a beam current of 18 mA U^{4+}.

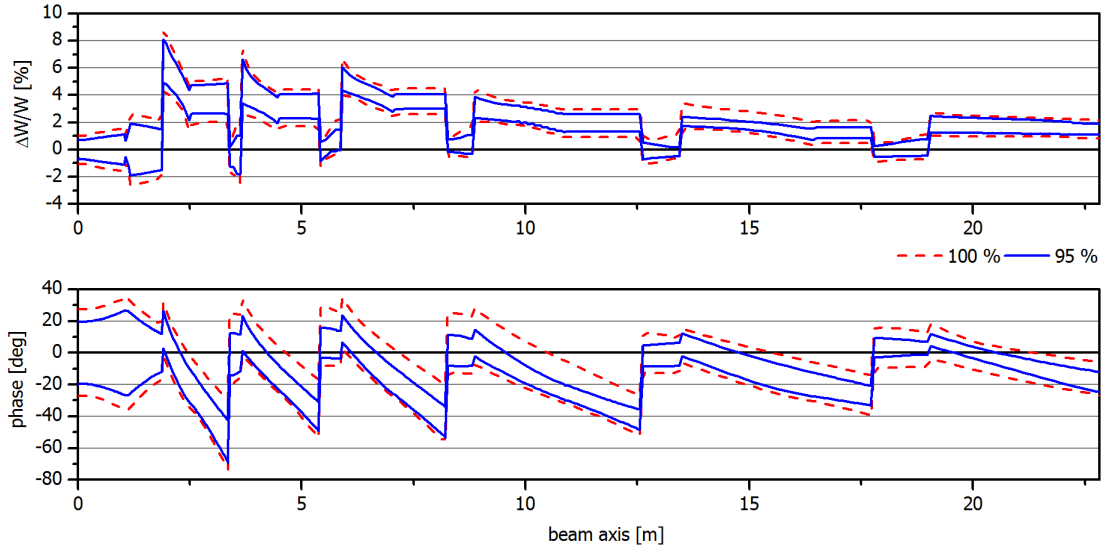

Figure 5.10: Longitudinal beam envelopes for the HSI IH-DTL with the new MEBT section for a beam current of 18 mA U^{4+}.

The transverse and longitudinal beam envelopes for the IH-DTL with the new MEBT are shown in Figure 5.9 and Figure 5.10, respectively. Good aperture clearance close to the original design of the IH-DTL can be seen for the transverse beam envelopes in Figure 5.9. This shows that with proper matching, the IH-DTL can perform well after the 2009 RFQ upgrade. As can be seen in Figure 5.10, the longitudinal beam envelopes are well confined throughout the whole linac. Hence, the injection into the IH-DTL is well within the longitudinal acceptance of the KONUS lattice in IH 1 and IH 2. If the beam were not matched to the KONUS lattice, the 100 % phase and energy envelopes would widen significantly along the linac resulting in particles with excessive energy and phase. These particles would then be lost at some point in the linac or the following transport section.

5.2.2 Comparison of Superlens and new MEBT

Output of	**Matching section**		**HSI (behind IH 2)**	
	Superlens	**new MEBT**	**Superlens**	**new MEBT**
Transmission [%]	90.45	99.99	87.6	99.39
$\epsilon_{\mathrm{rms}}(x-x')$ [mm mrad]	0.112	0.071	0.181	0.118
$\epsilon_{\mathrm{rms}}(y-y')$ [mm mrad]	0.093	0.073	0.158	0.134
$\epsilon_{\mathrm{rms}}(\phi-W)$ [$\frac{\mathrm{keV}}{\mathrm{u}}$ns]	0.362	0.341	1.371	0.508
$\Delta\epsilon_{\mathrm{rms}}(x-x')$ [%]	68.3	7.5	173.4	77.6
$\Delta\epsilon_{\mathrm{rms}}(y-y')$ [%]	35.3	6.5	129.4	95.6
$\Delta\epsilon_{\mathrm{rms}}(\phi-W)$ [%]	11.1	4.8	321.5	56.1
$B_{x,90\,\%}$ [$\frac{\mathrm{mA}}{\mathrm{mm\ mrad}}$]	36.1	66.2	20.3	39.1

Table 5.3: Comparison of simulation results for the Superlens MEBT and new MEBT section for a beam current of 20.75 mA U^{4+}. $B_{x,90\,\%}$ is the beam brilliance in the horizontal plane.

For the comparison of both the Superlens MEBT and the new MEBT followed by the two IH-DTL tanks of the HSI, both were calculated using the same simulated RFQ output distribution from the 2009 RFQ upgrade (see Figure 5.6). The calculations were performed with 20.75 mA U^{4+} beam current since the available RFQ particle distribution was calculated for this value. For the new MEBT, the results

show significant improvement in the emittance growth along the IH-DTL (see Table 5.3). This is a direct result of the improved matching between RFQ and IH-DTL with the new MEBT section. In contrast to the new MEBT, the Superlens MEBT already shows significant emittance growth of 68.3 % and 35.3 % in $x - x'$ and $y - y'$ respectively, directly behind the Superlens. At this point, the new MEBT section only shows minimal emittance growth of 7.5 % and 6.5 % in $x - x'$ and $y - y'$ respectively. The longitudinal emittance growth of the IH-DTL including the Superlens is 321.5 %, showing evidence for a mismatch of the longitudinal beam parameters. This value is reduced to just 56.1 % by the proposed new MEBT section. With the existing Superlens MEBT, losses of almost 10 % already occur in the matching section. Additional losses in the two IH-DTL tanks result from input mismatch at the IH-DTL entrance. Therefore, the simulated total transmission of the HSI from the beginning of the MEBT to the exit of the IH-DTL is only 87.6 % for the existing section. In contrast, the new MEBT section shows a total transmission of 99.39 % behind the IH-DTL. Remaining losses in the new MEBT section can be attributed to a few, outlying particles in the simulated RFQ distribution.

In summary, the horizontal beam brilliance of the HSI is improved by 93 % with the new MEBT section. The beam brilliance at the HSI exit with the new MEBT is even higher than the beam brilliance that is achieved directly behind the existing Superlens. Replacing the existing Superlens MEBT with the new MEBT proposed in this work would be a big step towards higher beam currents, fulfilling FAIR requirements with the HSI.

6 Poststripper IH-DTL

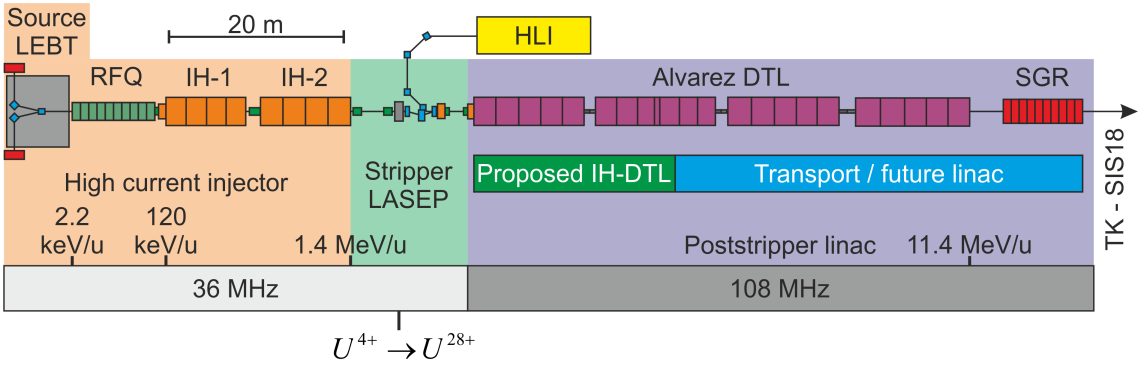

Figure 6.1: Layout of the UNILAC showing the different lengths of the existing Alvarez-DTL and the proposed new IH-DTL.

The poststripper linac section of the GSI UNILAC is positioned behind the gas stripper at 1.4 MeV/u particle energy (layout shown in Figure 6.1). It is used to accelerate the beam coming from the HSI after stripping to U^{28+} from 1.4 MeV/u to 11.4 MeV/u which is the common injection energy for the SIS18 synchrotron.

The existing poststripper linac is an Alvarez DTL that was commissioned in 1975 and extended in 1985. Consequently, its first two tanks are more than 40 years old. In the last ten years the number of drift tube failures in the Alvarez has increased significantly along with other age related issues such as corrosion of the cooling channels in the tanks [41]. Therefore a replacement of the Alvarez section is inevitable to provide a reliable injector for FAIR. The motivation for the presented poststripper linac design was to provide an efficient replacement option for the existing poststripper linac at the GSI UNILAC. For the role of a dedicated FAIR injector, the UNILAC has to provide short high current pulses to the SIS18 synchrotron (100 - 200 µs pulse length, 15 mA U^{28+} beam current, 2.7 Hz).

In the following a linac based on 108 MHz IH-type cavities and the KONUS beam dynamics concept is proposed [5] as a replacement of the existing Alvarez DTL. With the proposed IH-DTL, a lot of additional space is left in the UNILAC tunnel,

paving way for possible future upgrades of the UNILAC to reach higher energies (see Figure 6.1). The poststripper IH-DTL proposed in this work is designed as a dedicated injector for FAIR. This chapter consists of a description of the linac layout (Chapter 6.1), beam dynamics simulations (Chapter 6.2) and detailed error studies (Chapter 6.3).

6.1 Layout

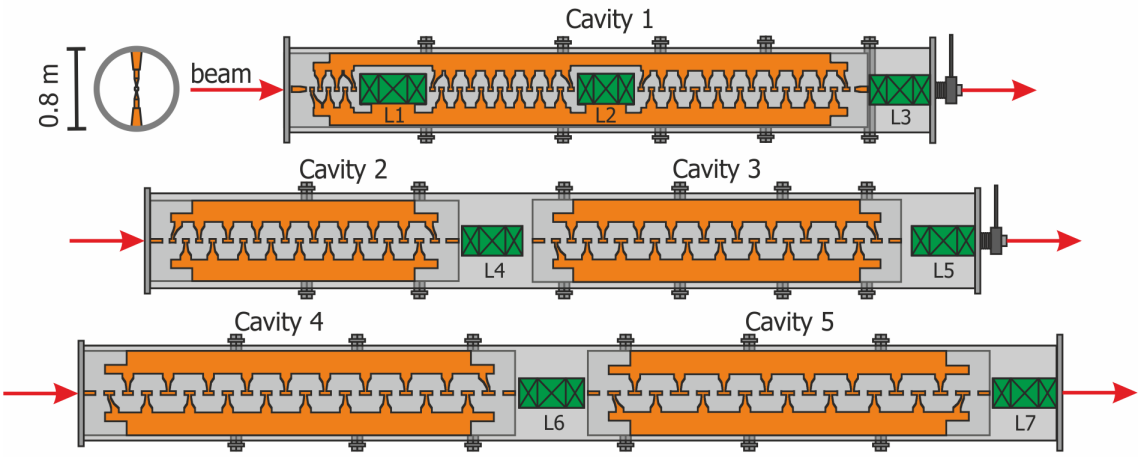

Figure 6.2: Layout of the poststripper IH-DTL.

The proposed poststripper linac design consists of five 108 MHz IH-DTL cavities and seven quadrupole triplet lenses, as shown in Figure 6.2. It can be operated by the existing UNILAC RF amplifier structure well within power limits [8, 42]. To achieve this, the first cavity is designed with two internal lenses, a technology that has proven reliable in several linacs built in the last decades (e.g. HSI [31] and HLI [43] at GSI UNILAC, the HIT Heidelberg [19], NICA at JINR Dubna [44]). A U^{28+} beam is accelerated in the poststripper linac from 1.4 MeV/u to 11.4 MeV/u, which equals to a total accelerating voltage of 85 MV. With a total linac length of 22.8 m, the average accelerating gradient of the design is 3.73 MV/m. In Table 6.1, the main parameters of the linac are summarized. The whole linac was developed with the in-house beam dynamics code LORASR [39, 23] and the cavity design was done with CST Microwave Studio[1] (see Chapter 7). Cross-checks of the beam dynamics

[1] https://www.cst.com/products/cstmws

and error studies were performed with the beam dynamics code TraceWin[2].

Table 6.1: Design parameters of the poststripper IH-DTL.

Total length	22.8 m
Operating frequency	108.408 MHz
Machine avg. accelerating gradient	3.73 MV/m
Number of cavities	5
Number of quadrupole triplets	7
Beam properties	
Reference particle	U^{28+}
Mass over charge ratio	$A/q \leq 8.5$
Injection energy	1.4 MeV/u
Exit energy	11.42 MeV/u
Cavities	
Cavity lengths	2.75 to 4.89 m
Inner diameter	69.6 to 81 cm
Aperture diameter	25 mm
Gap lengths	3.85 to 10.2 mm
Avg. on-axis field	6 to 11.3 MV/m
Quadrupole Triplets	
Triplet lengths	45 to 56 cm
Outer singlet lengths	12.2 to 14.4 cm
Inner singlet lengths	20.5 to 26.9 cm
Aperture diameter	36 mm
Magnetic field gradients	45 to 54.4 T/m
Pole tip fields	0.87 to 1.03 T

To provide a reliable and durable machine design, the design limits were chosen to be state of the art values. For example, the maximum on axis electric field in the IH-cavities is just above 11 MV/m which is considered safe for an IH-type structure

[2]http://irfu.cea.fr/Sacm/logiciels/index3.php

at this frequency [18]. Additionally, quadrupole magnetic fields are kept below 1.1 T at the pole tip. This provides some operational margin, since tip fields of 1.3 T are possible using existing pulsed magnet technology.

6.1.1 Modular Cavity Concept

The linac is divided into three separate mechanically rigid sections (as shown in Figure 6.2). In addition, each tank section is divided into short modules of $<$1.5 m length to allow copper plating and easy alignment of the modules with drift tubes and lenses. At the operating frequency of 108.408 MHz, the cavity inner diameters are in the range of $0.7 - 0.8$ m. For the first cavity an example of two mechanical modules is shown in Figure 6.3. While the second module of tank one contains only drift tubes, the third module houses an internal quadrupole triplet and the following drift tubes. The concept of dividing a cavity into cylindrical tank modules has been successfully used for example for the 36 MHz HSI-RFQ at GSI UNILAC [20], which has similar tank dimensions as the poststripper IH-DTL. Accurate alignment of such cavity modules is possible within transverse tolerances of less than 0.1 mm.

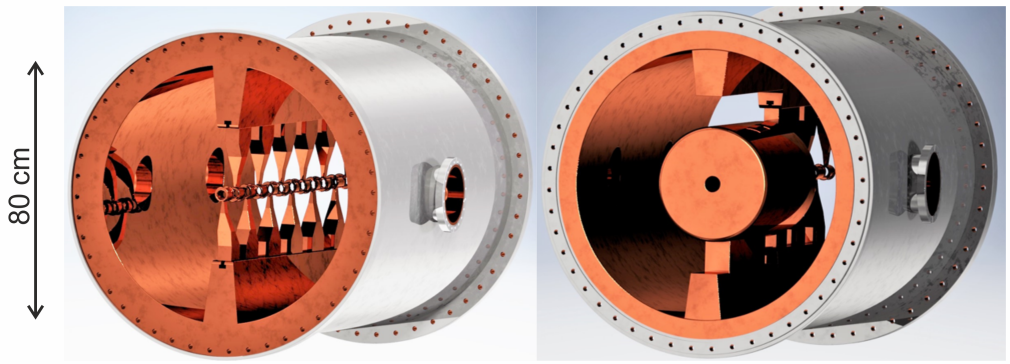

Figure 6.3: Tank modules two (left) and three (right) of tank one (renderings courtesy of D. Bänsch, Goethe University Frankfurt).

6.2 Beam Dynamics

The beam dynamics design is based on the KONUS beam dynamics concept. Starting in front of the first quadrupole triplet, the first drift tube section is a zero degree section without rebunching gaps. All subsequent six sections are KONUS sections with four to six rebunching gaps and 10 to 17 gaps with zero degree synchronous phase. In this design, the beam is injected into the zero degree sections with an excess energy of two to six percent relative to the geometric virtual synchronous particle (for details on the KONUS beam dynamics, see Chapter 3). Design and optimizations of the linac beam dynamics were performed with LORASR. A cross-check with TraceWin was also performed followed by error studies to define tolerances for manufacturing and alignment (see Chapter 6.2.4 and 6.3).

6.2.1 Simulations of the Reference Design

In the following simulations, the beam dynamics of the IH-type linac developed in this work are examined. These simulations were performed for a beam current of 15 emA U^{28+} with $5 \cdot 10^5$ macro particles distributed by a Waterbag distribution (see Figure 6.4). During the design phase, the number of simulated particles was typically $1 \cdot 10^4$ to reduce computation time. All relevant simulation and input parameters are summarized in Table 6.2. The average macro pulse current in these simulations is 15 emA, while the equivalent bunch current, which determines the space charge in the particle bunch, is 45 emA. This is due to the fact, that the HSI operates at 36 MHz instead of 108 MHz and therefore only each third bucket in the poststripper linac contains a particle bunch at 108 MHz. Taking into account the

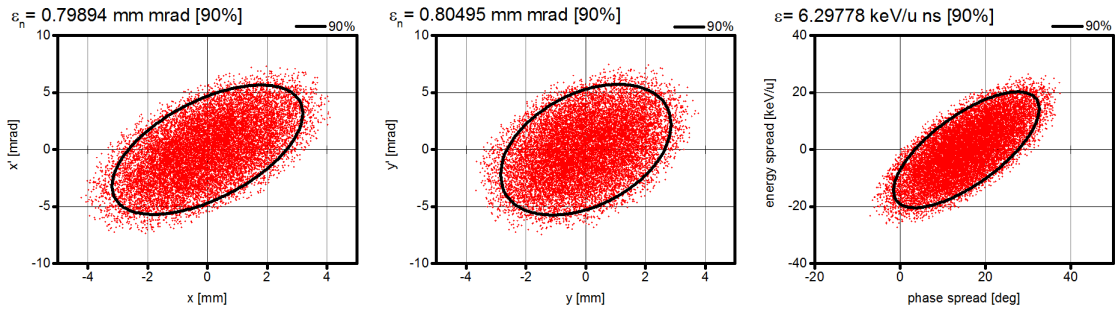

Figure 6.4: Input particle distribution for the poststripper IH-DTL. Only $1.5 \cdot 10^4$ of the total $5 \cdot 10^5$particles are shown for better visibility of the density distribution.

actual RFQ output distribution from 2009 (Chapter 5), simulations of the HSI with the new MEBT section were performed to acquire realistic beam emittance values as a basis for the poststripper linac input beam. To account for emittance growth in the gas stripper and in the following charge state separator, the HSI output emittances were increased by 50 % in the transverse and by 200 % in the longitudinal plane [45]. The resulting particle distribution, used to design and optimize the linac is shown in Figure 6.4 with the RMS emittances stated in Table 6.2.

Table 6.2: Simulation and input parameters for the IH-DTL LORASR simulations.

Simulation parameters	
Operating frequency	108.408 MHz
Number of macro particles	$5 \cdot 10^5$
Particle distribution	6D Waterbag
3D PIC grid dimensions	128 x 128 x 128 cells
Input beam properties	
Ion species	U^{28+}
Mass over charge ratio	A/q = 8.5
Beam current (macro pulse average)	15 emA
Beam current (bunch equivalent)	45 emA
$\epsilon_{\mathrm{rms}}(x - x' \ \& \ y - y')$	0.192 mm mrad
$\epsilon_{\mathrm{rms}}(\phi - W)$	1.549 keV/u ns
	14.39 MeV deg

Transverse Beam Dynamics

Based on magnetic quadrupole triplet lenses, the focusing lattice provides strong focusing of the beam over several meters. This allows for the use of efficient IH-type cavities with lengths in the range of $3 - 5\,\mathrm{m}$. The transverse focusing of the triplet lenses was optimized with a constant phase advance approach to improve the beam emittance and aperture clearance (further details follow in Chapter 6.2.3). These optimizations showed, that the linac should be divided into two groups of focusing sections[3]. Therefore, the first three sections and the remaining three section are

[3]The sections are numbered consistent with the lens numbering, meaning that section 1 starts in the center of L1 and ends in the center of L2 and so on.

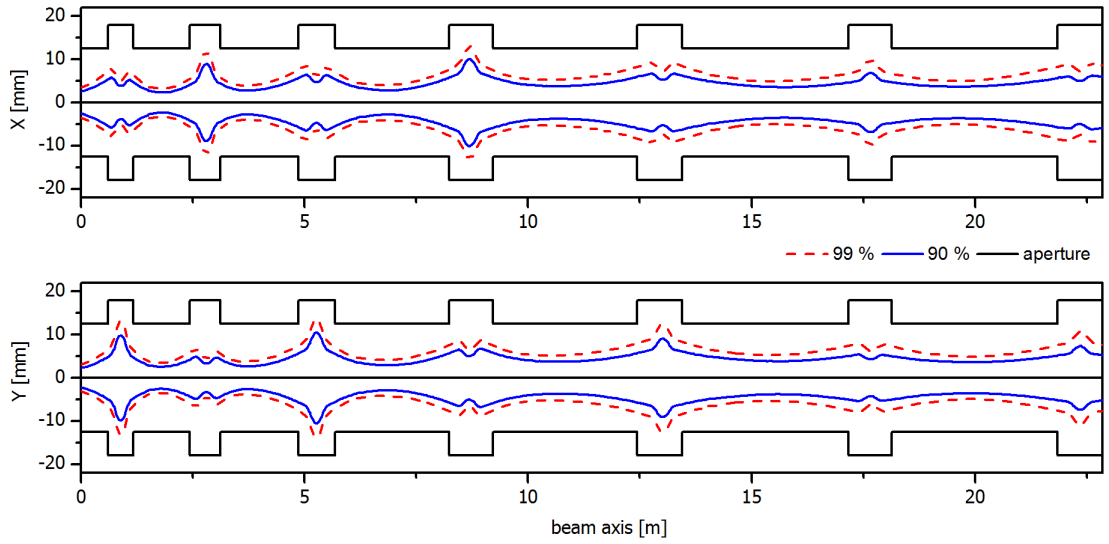

Figure 6.5: Transverse beam envelopes of the poststripper IH-DTL.

grouped together. An optimal phase advance of $\sigma = 80°$ (depressed tune including space charge) was found for the first three sections. For the last three sections, a phase advance of $\sigma = 60°$ was determined to be optimal. This way, emittance growth is reduced and aperture filling is relaxed in the later sections. In Figure 6.5, the resulting beam envelopes are shown for the reference design. Due to sufficient aperture clearance, no losses are observed even with the high accuracy simulation involving $5 \cdot 10^5$ macro particles. The limits of the design regarding misalignment and operating errors are investigated in error studies in the following Chapter 6.3.

Longitudinal Beam Dynamics

The longitudinal beam dynamics were optimized for low emittance growth and reasonably high acceptance. In the first two sections, the surplus energy of the bunch center is set to 6 % and 5.5 % and then reduced to below 4 % and gradually decreased in each following section. In Figure 6.6, the bunch center motion for the whole linac is shown. Each data point represents the center of mass of the particle bunch in each gap. In the first sections, a relatively high injection surplus energy is required to provide sufficient longitudinal beam focusing in the zero degree section, while keeping them short enough to allow stable transverse beam transport at low energies. All sections are optimized for a stable beam acceleration with low emittance growth. The acceptance of the design could be increased further by decreasing

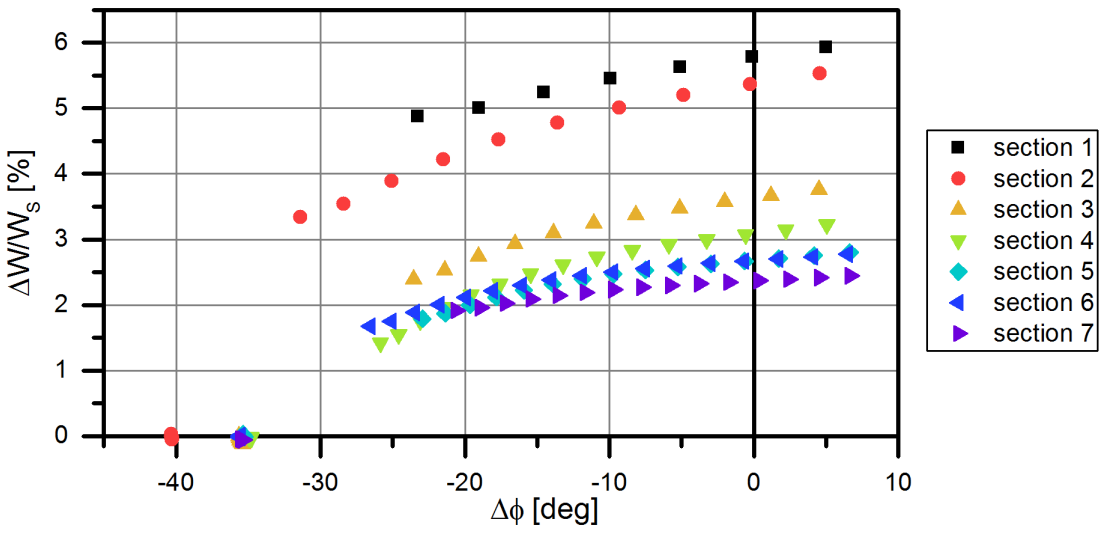

Figure 6.6: Bunch center motion of the poststripper IH-DTL.

the starting phases of the zero degree sections, but this would sacrifice acceleration efficiency. Therefore the design is always a trade-off between longitudinal acceptance and acceleration efficiency. In Figure 6.7, the longitudinal beam envelopes show the typical jumps in energy and phase of a KONUS design, expressing the changing definition of the virtual synchronous particle. The energy difference $\Delta W/W_s$ alternates between surplus energy in the zero degree sections and $W - W_s = 0$ for the rebunching sections. In the zero degree sections the bunch center phase decreases to about -50° in the first two sections and -30° in all the following sections. However, it has to be noted that, at the end of each zero degree section, the beam passes through a quadrupole triplet which means a drifting beam in the longitudinal plane. Therefore the minimum phase within an accelerating gap is around -30° as also shown in the bunch center motion plot (Figure 6.6). The expansion of the beam in the energy- and phase-regime is shown as centered beam envelopes in Figure 6.8. The centered beam envelopes show, that the beam is well confined in phase and energy, proving that the longitudinal focusing is working as expected.

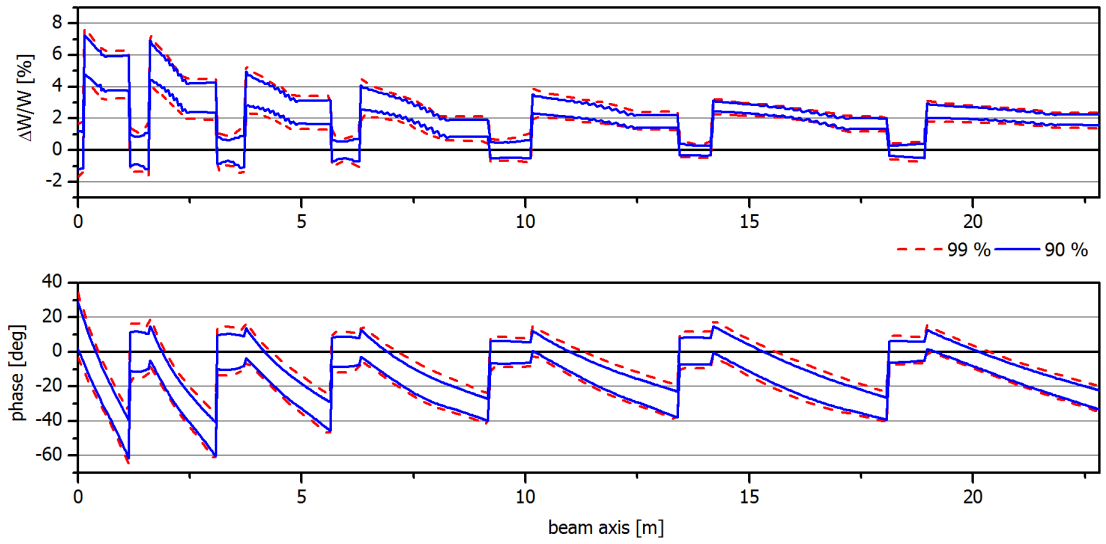

Figure 6.7: Longitudinal beam envelopes of the poststripper IH-DTL. Bunch energy relative to the virtual synchronous particle (top), bunch phase relative to the virtual synchronous particle (bottom).

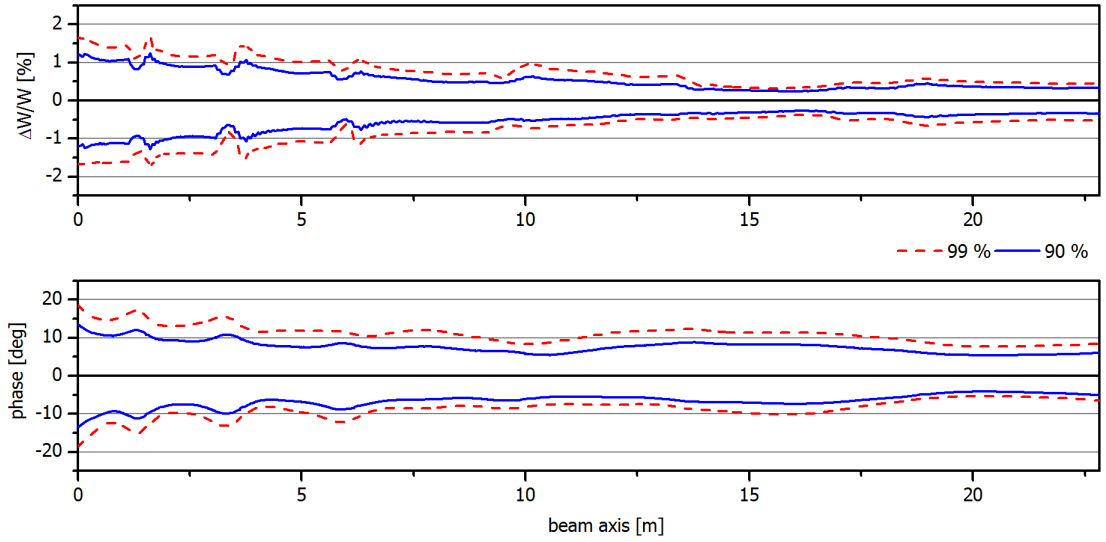

Figure 6.8: Centered longitudinal beam envelopes of the poststripper IH-DTL. Bunch energy (top), bunch phase (bottom).

Beam Quality

A key parameter to judge the quality of a particle beam in accelerators is the beam emittance. Therefore a minimization of emittance growth along the linac is the goal of most optimization performed on the design. For the linac design developed in this work, the simulated RMS emittance growth for a beam passing the whole linac is 27.5 % and 25.8 % in the transverse planes $x - x'$ and $y - y'$ respectively and 11.1 % in the longitudinal plane (see Figure 6.11). These values result from the optimization of the transverse and longitudinal focusing scheme to minimize RMS emittance growth.

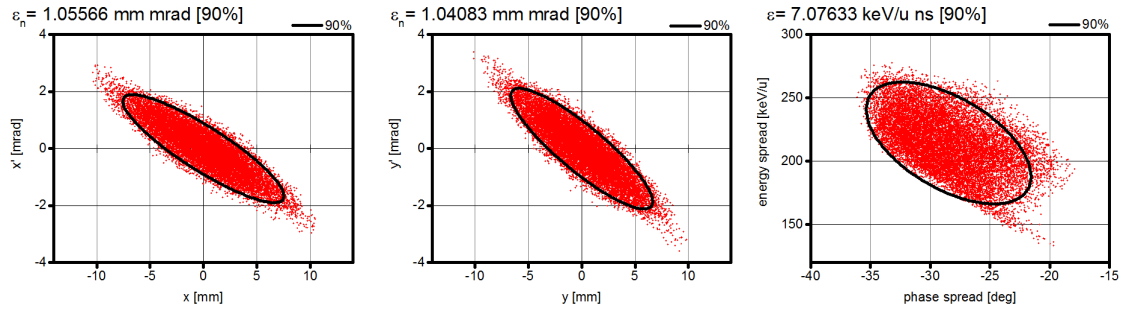

Figure 6.9: Output particle distribution for the poststripper IH-DTL. Only $1.5 \cdot 10^4$ of the total $5 \cdot 10^5$particles are shown for better visibility of the density distribution.

In Figure 6.9, the output particle distributions for all three planes are shown. The beam quality, that can be achieved with the new poststripper IH-DTL, can also be judged qualitatively from these plots. In the transverse planes, almost no deviation from their original ellipse form is visible. However, the emittance growth in the transverse plane leads to a slight elongation of the particle distribution by particles on the edge of the distribution. Due to the optimized longitudinal beam dynamics, the longitudinal plane also shows low emittance growth and a small "tail" only. Still some particles are shifted towards more positive phases leaving the output distribution with a relatively sharp boundary on the negative phase side and smeared out towards more positive phases. Histograms of the phase plane comparing the input beam distribution and the output distribution are shown in Figure 6.10, illustrating the effect. Finally, the presented design proves that, with careful optimization, the KONUS beam dynamics concept is not at a disadvantage regarding emittance growth compared to other concepts. While the complexity of the longitudinal beam dynamics is an issue in designing such a KONUS linac, the finished design can be

operated in the same way as every other structure, only dependent on correct phase and field amplitude settings. The progression of RMS emittance growth along the linac is shown in Figure 6.11. While the majority of emittance growth appears in the first half of the linac, the overall progression of emittance growth shows a smooth profile without discontinuities.

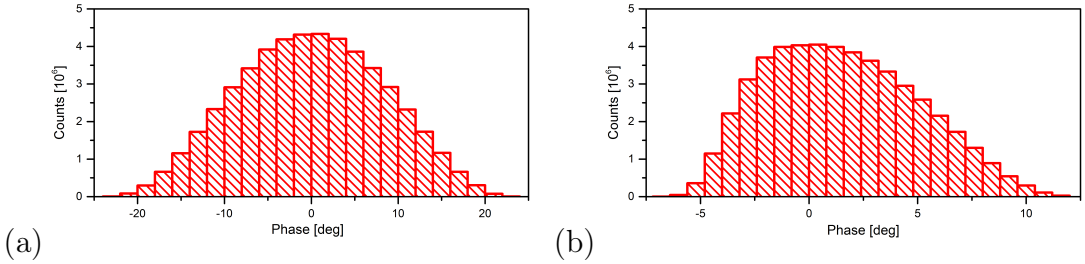

Figure 6.10: Histograms of the particle phase distribution at the input (a) and the exit (b) of the linac. A shift towards more positive phases is visible for the accelerated beam behind the linac.

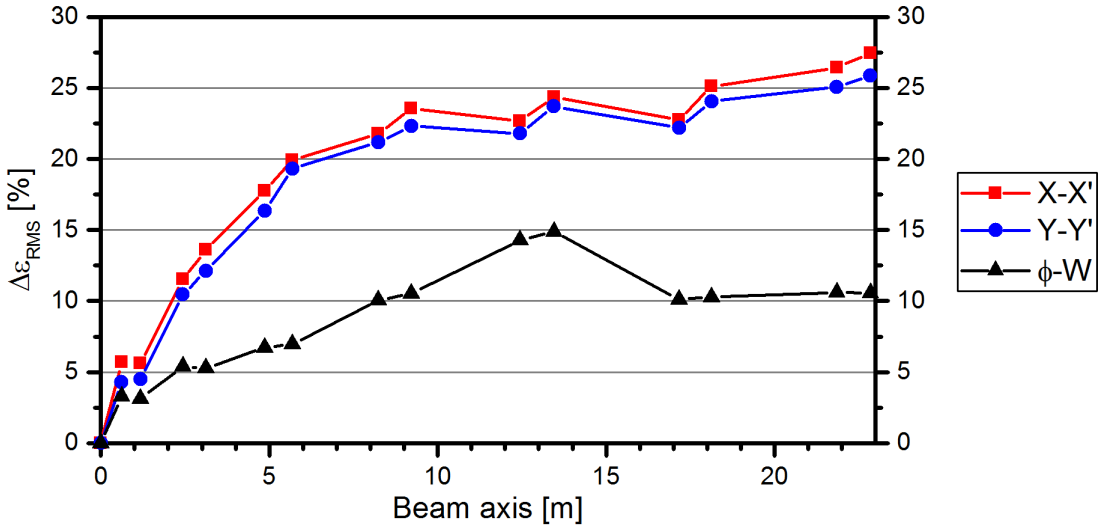

Figure 6.11: RMS emittance growth progression for the whole IH-DTL.

6.2.2 Multi-Turn Injection Parameters

For the multi-turn injection of the UNILAC beam into the SIS18 synchrotron, the key parameters are the horizontal beam emittance and the beam current contained therein (see Chapter 4.2). In Figure 6.12, the beam current for partial horizontal emittances of the output distribution calculated in Chapter 6.2.1 (compare Figure 6.9) is shown. In this case, the absolute beam emittance is shown instead of the normalized emittance.

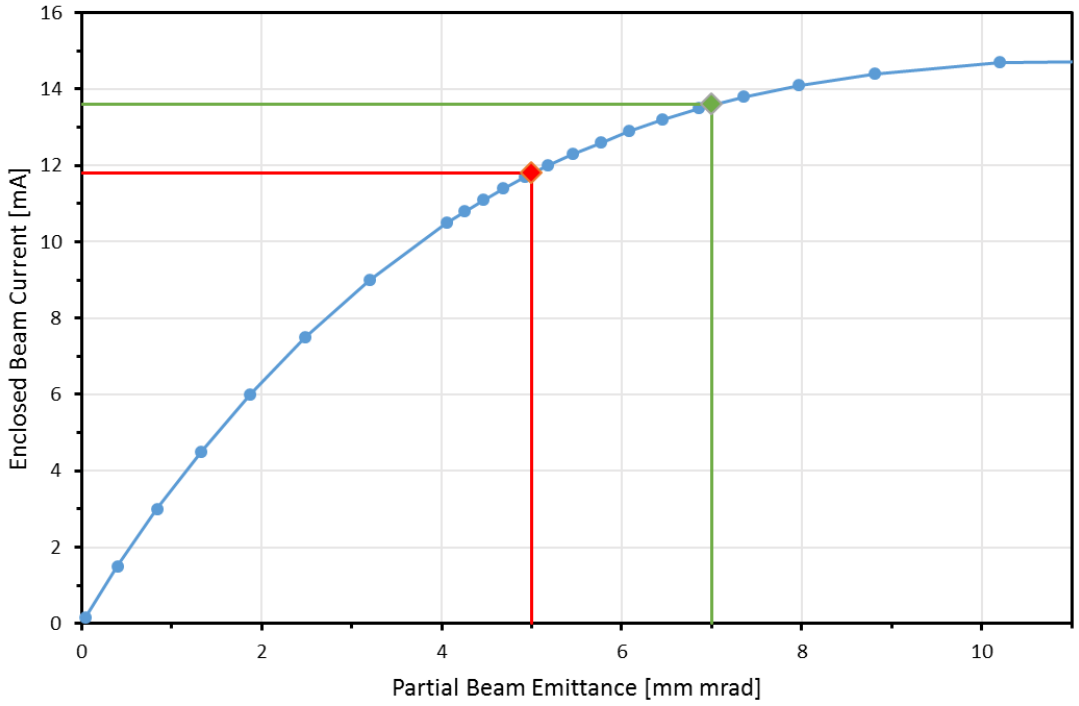

Figure 6.12: Beam current for different partial beam emittances of the horizontal output particle distribution from the IH-DTL. The horizontal emittances 5 mm mrad and 7 mm mrad with the corresponding beam currents are marked by the red and green lines, respectively.

Table 6.3: SIS18 injection parameters for the proposed poststripper IH-DTL.

Partial Emittance	Enclosed Current	N_{injected}	N_{turn} limit
5 mm mrad	11.8 mA	22	30
7 mm mrad	13.6 mA	19	21

The injection parameters for 5 mm mrad and 7 mm mrad horizontal beam emittance are summarized in Table 6.3. To get $N_{\mathrm{part}} = 2.7 \cdot 10^{11}$ uranium ions injected into the SIS18, the multi-turn injection needs 22 turns for the small emittance case ($\epsilon_x = 5\,\mathrm{mm\ mrad}$) and 19 turns for the larger emittance ($\epsilon_x = 7\,\mathrm{mm\ mrad}$), assuming lossless injection. In case of the small emittance, the neccessary number of turns is much lower than the theoretical limit for injection. Therefore, it might be beneficiary to collimate the beam to use only a smaller fraction to fill the SIS18 to the space charge limit.

The positive effects of beam collimation in the transfer line before injection into SIS18 have been studied experimentally at GSI [36, 46]. In first collimation experiments with 2 mA U^{28+} beams that had a horizontal emittance of $\epsilon_x = 6.8\,\mathrm{mm\ mrad}$, a total of 20 turns could be injected with 99 % efficiency.

Further experiments were performed with U^{28+} beams of up to 2.4 mA beam current and a horizontal beam emittance of 5 to 7 mm mrad. The particle losses during the SIS18 injection were significantly reduced by cutting away about 25 % of the injected beam. Due to the improved injection efficiency using collimation, it was possible to extract more particles after acceleration in SIS18 than without collimation, using the same UNILAC beam.

In November 2012, a total of $3.2 \cdot 10^{10}$ U^{28+} ions were extracted after acceleration in SIS18 [36].

6.2.3 Influence of Phase Advance on Beam Quality

Experience gained during the design of the linac showed, that is is beneficiary to keep a constant phase advance in both transverse planes along the whole structure. This way a stable beam envelope is almost guaranteed and usually no significant emittance growth is observed.

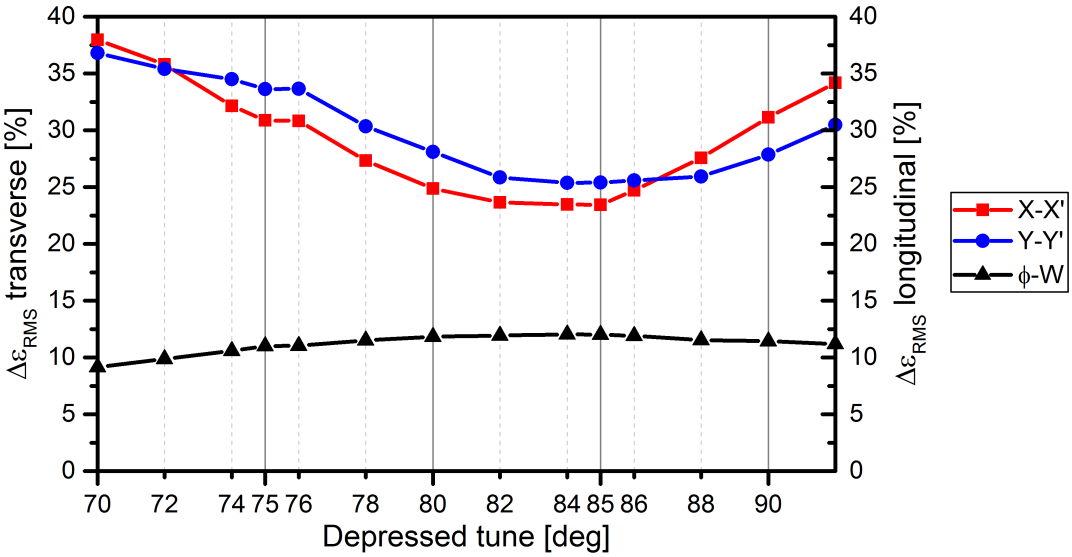

Figure 6.13: RMS emittance growth of the IH-DTL for different phase advances.

To further investigate the influence of the transverse focusing on beam emittance, dedicated studies were performed for the poststripper IH-DTL. In the following, results for different constant phase advance settings are presented. Beam dynamics simulations in this chapter were performed with LORASR and with a self-written MATLAB[4] script. The MATLAB script is used to find the correct lens gradients for a predefined phase advance in each section of the linac. By iteratively running LORASR in batch mode, reading in the resulting phase advance and automatically adjusting the lens gradients, the desired phase advance value is found. This process runs until a satisfying accuracy is reached. In case of the linac under investigation, with a minimum step size of 0.01 T/m, an accuracy of $\pm 0.5°$ can be achieved. For the whole linac structure, the phase advance σ was varied from $\sigma = 70°$ to $\sigma = 92°$ for a beam current of 15 mA. Due to losses, occurring in the triplet aperture at higher phase advances, the simulations are limited to $\sigma \leq 92°$. In this study, the simulations were performed using a Waterbag distribution with 1000 macro particles to achieve

[4]https://de.mathworks.com/products/matlab.html

manageable computation times due to the high number of iterations necessary. For the particle distributions, the same Twiss parameters and emittances as in the design of the linac (Chapter 6.2.1) were used.

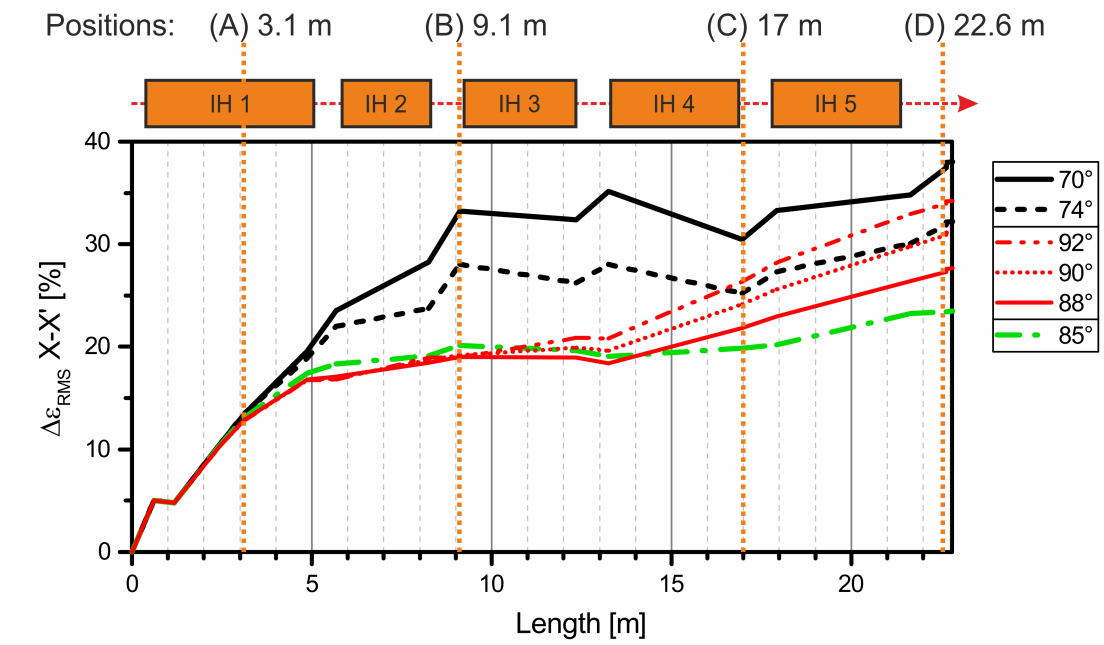

Figure 6.14: Emittance growth progression in the $x - x'$ plane along the linac for different phase advances. For low phase advance (black lines), optimal phase advance (green line) and high phase advance (red lines). The positions (A) to (D) correspond to the positions of the following Figures 6.15 and 6.16.

The results show, that the transverse emittance at the linac output is dependent on the phase advance of the focusing elements. At $\sigma = 70°$, the emittance growth is 38 % and 37 % in $x - x'$ and $y - y'$, respectively (see Figure 6.13). This is the highest value in this study. At the other extreme with $\sigma = 92°$ the emittance growth is 34 % and 30.5 % in $x - x'$ and $y - y'$, respectively. In the range of $82° \leq \sigma \leq 86°$, the optimal phase advance is found with an emittance growth of around 25 % in both planes. For the investigated phase advance values, the quadrupole gradients range from $B'(\text{min/max}) = 48\ \text{T/m} - 54\ \text{T/m}$ for $\sigma = 70°$ to $B'(\text{min/max}) = 53\ \text{T/m} - 57\ \text{T/m}$ for $\sigma = 92°$. In Figure 6.14 the emittance growth progression along the linac is shown for different constant phase advances. For phase advances $\sigma < 85°$, the shapes of the emittance growth progressions along the linac are similar to each other. Only the magnitude of the emittance growth decreases with

increasing phase advance. A sudden change from this behavior appears for $\sigma > 85°$, in which case the emittance growth stays relatively constant with increasing phase advance until the end of cavity three but then a sudden increase in emittance growth is observed.

Position (A) behind L2 at 3.1 m total length $W_{(A)} = 2.71\ \frac{\mathrm{MeV}}{u}$

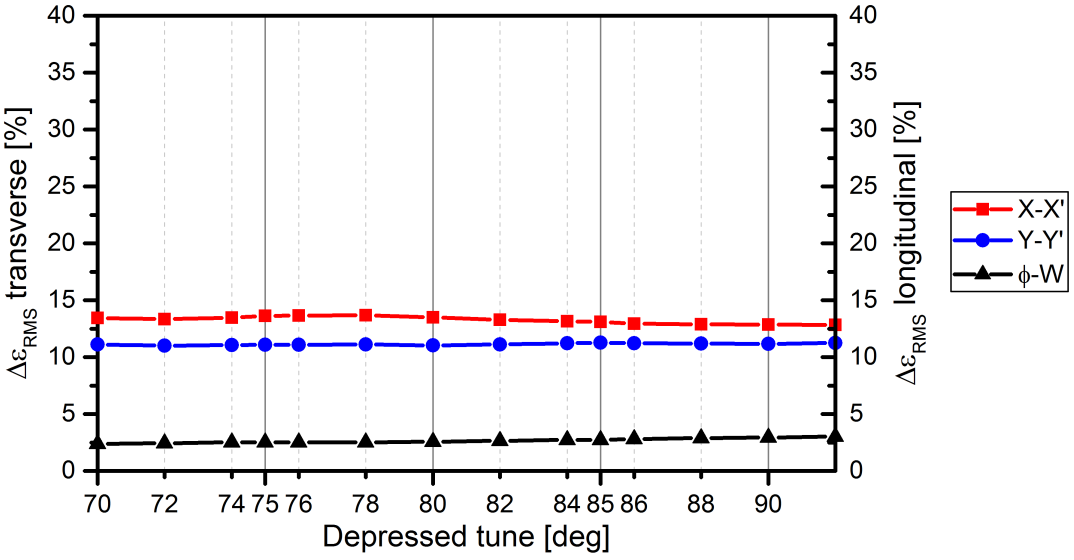

Position (B) behind L4 at 9.1 m total length $W_{(B)} = 5.41\ \frac{\mathrm{MeV}}{u}$

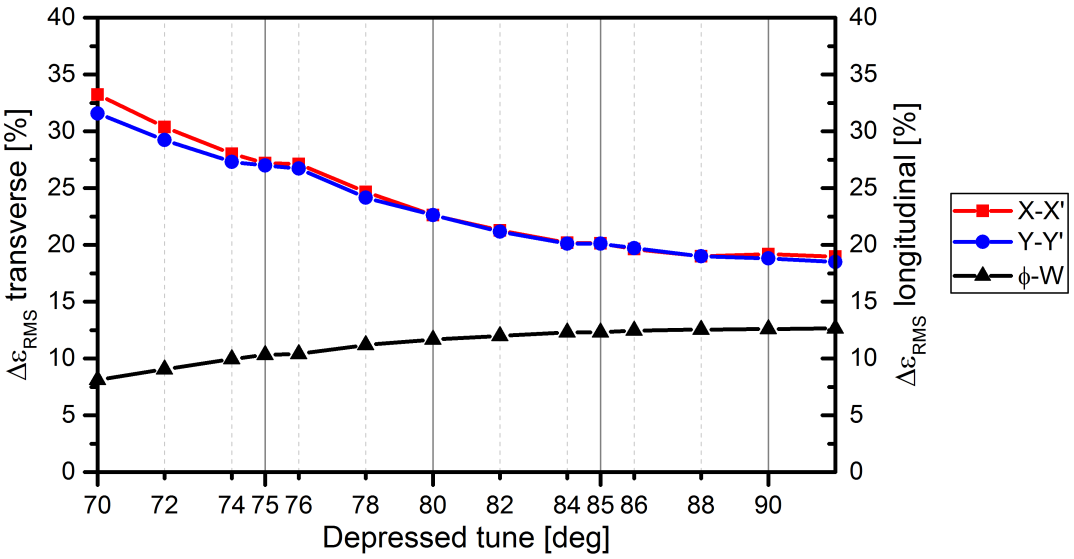

Figure 6.15: Emittance growth for different phase advances at positions (A) and (B) defined in Figure 6.14.

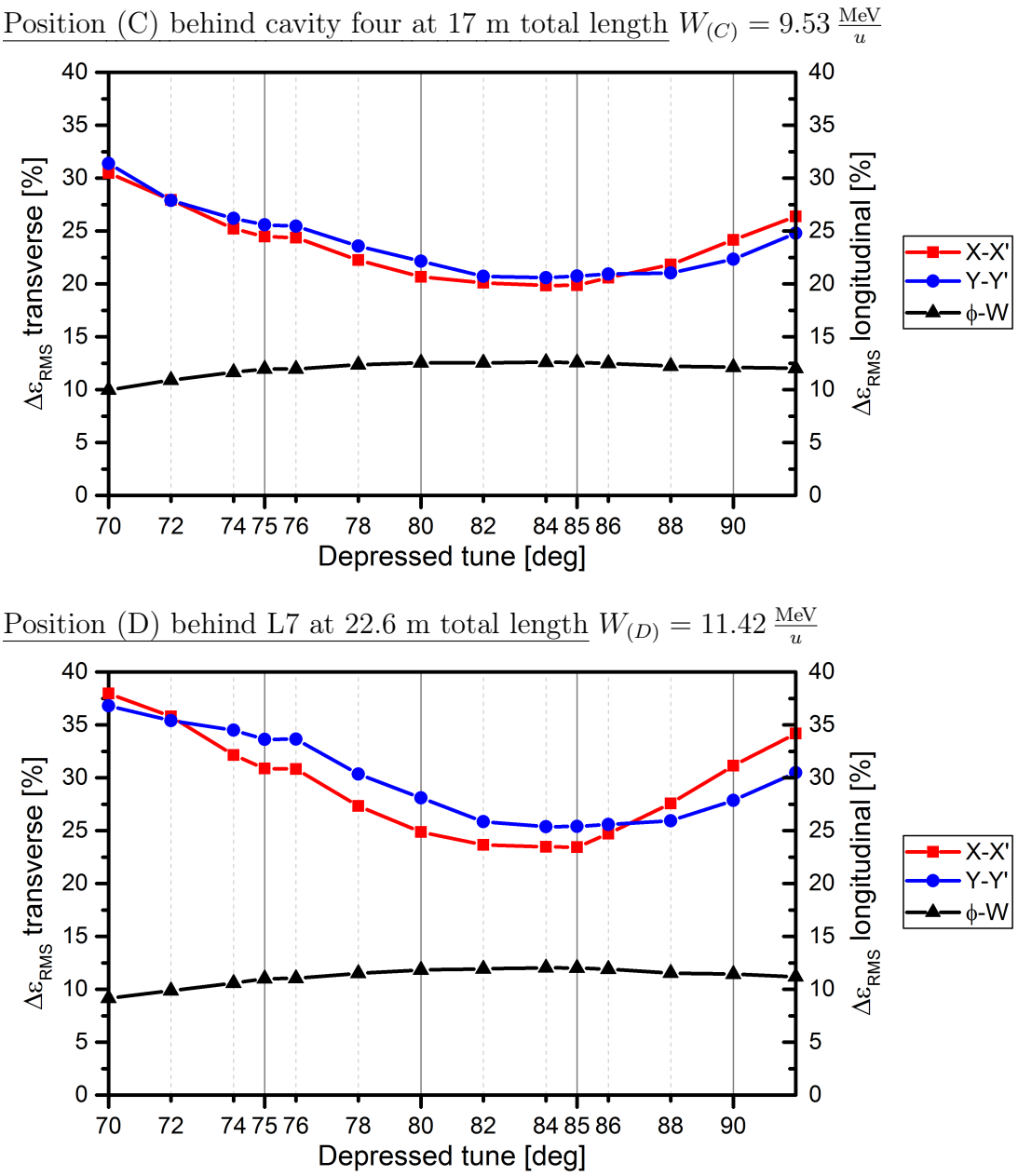

Figure 6.16: Emittance growth for different phase advances at positions (C) and (D) defined in Figure 6.14.

In Figures 6.15 and 6.16, the behavior behind different sections of the linac with respect to the phase advance is shown. For better orientation, the positions (A) to (D) along the linac for these plots are marked in Figure 6.14. The first position (A) is behind the second internal triplet lens L2 (compare Figure 6.2) of the first cavity at 3.1 m total length (Figure 6.15). Here the emittance growth is almost independent of

the phase advance. Following this, the second position (B) is in front of cavity three (Figure 6.15), where a strong dependence on the phase advance becomes apparent. A clear trend of decreasing transverse emittance growth for growing phase advance is observed at this position. Positions (C) and (D) are behind cavities four and five, respectively. The transverse emittance growth in those last sections causes the emittance growth curve to rise up again for $\sigma > 85°$ (Figure 6.16). Furthermore, the last position (D) shows the overall behavior of the linac as also shown in Figure 6.13.

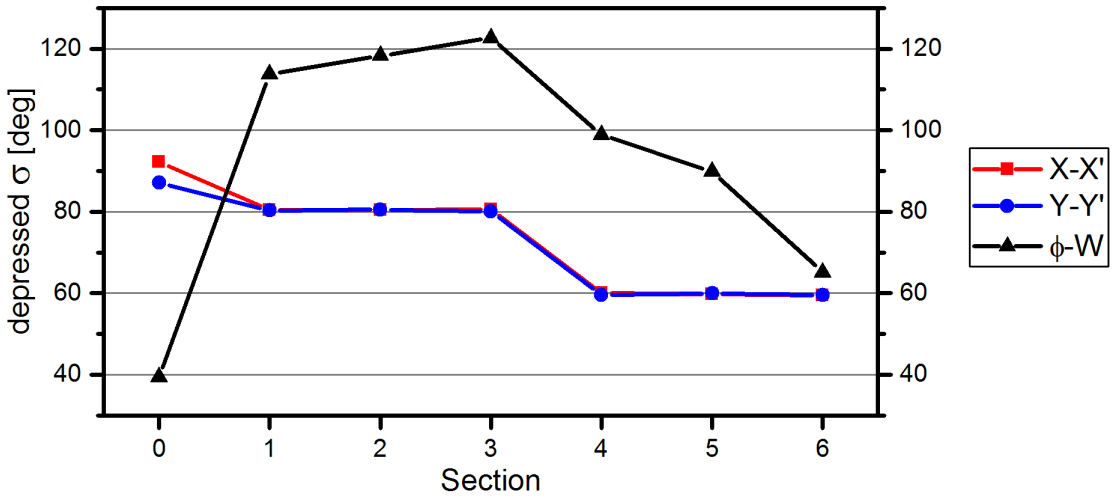

Figure 6.17: Phase advance plot for the final linac design with two different phase advance settings $\sigma_{1-3} = 80°$ and $\sigma_{4-6} = 60°$ for the first and second half of the linac.

In summary, the linac seems to be divided into two differently behaving regimes of transverse beam dynamics. While the first half of the linac benefits high phase advances for low emittance growth, the second half of the linac behaves in the opposite way. For the second half of the linac, the emittance growth is almost constant for low phase advance and rises rapidly above $\sigma = 85°$. As a consequence of this behavior, the focusing scheme of the linac was chosen to be $\sigma_{1-3} = 80°$ for the first three sections of the linac (ending with lens L4) and $\sigma_{4-6} = 60°$ for the remaining three sections (ending with lens L7) as shown in Figure 6.17. This way the emittance growth is further reduced to 22 % (for 1000 macro particles) by taking into account the specific behavior of the linac sections (see Figure 6.18). The resulting final emittance growth calculated with $5 \cdot 10^5$ particles is just 27 % (see Chapter 6.2.1). Another benefit of this configuration is that the beam envelope is

smaller in the last triplets due to the lower phase advance and therefore provides a bigger margin for errors.

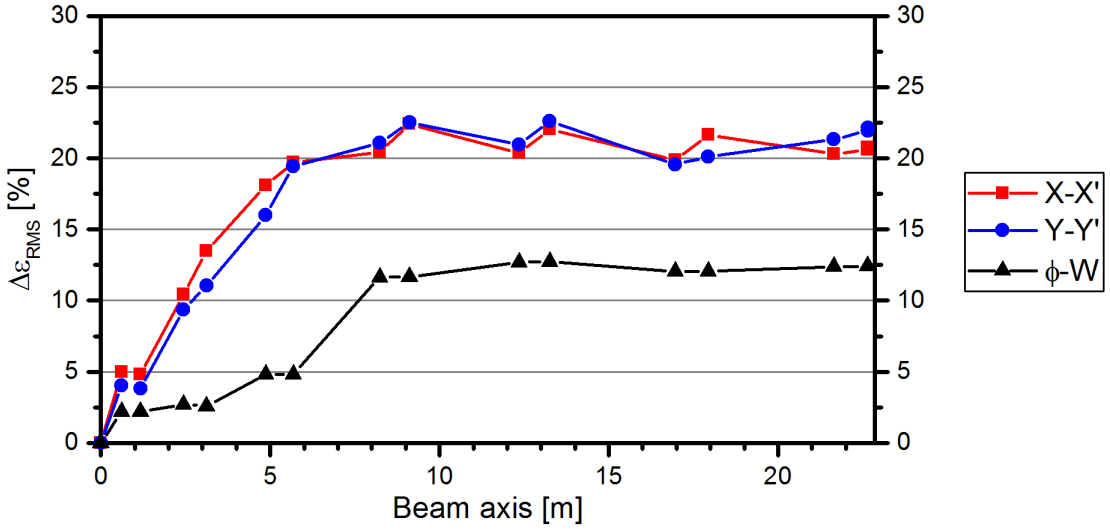

Figure 6.18: Corresponding emittance growth progression for the two sections phase advance approach.

6.2.4 TraceWin Simulations

For the purpose of cross-checking the beam dynamics results of the linac design, they were also calculated with the widely used TraceWin[5] code. The following simulations were performed for a 15 emA U^{28+} beam with $5 \cdot 10^5$ macro particles distributed by a Waterbag distribution with the same parameters as in Chapter 6.2. All relevant simulation and input parameters are summarized in Table 6.4. To assure high accuracy of the simulation results, the PICNIC[6] (3D) space charge solver was used with a 30 x 30 x 30 mesh cells within five RMS widths of the beam [47]. Particles outside of the mesh see the space charge potential of an equivalent Gaussian beam inside the mesh boundaries.

Table 6.4: Simulation and input parameters for the IH-DTL TraceWin simulations.

Simulation parameters	
Operating frequency	108.408 MHz
Number of macro particles	$5 \cdot 10^5$
Particle distribution	6D Waterbag
3D PIC grid dimensions	30 x 30 x 30 cells
Grid boundaries	$5 \cdot \sigma_{X/Y/Z}$
Input beam properties	
Ion species	U^{28+}
Mass over charge ratio	A/q = 8.5
Beam current (pulse average)	15 emA
Beam current (bunch equivalent)	45 emA
$\epsilon_{\mathrm{rms}}(x - x' \ \& \ y - y')$	0.19 mm mrad
$\epsilon_{\mathrm{rms}}(\phi - W)$	1.55 keV/u ns
	14.43 MeV deg

[5] http://irfu.cea.fr/Sacm/logiciels/index3.php
[6] PICNIC: "Particles In Cells Numerical Integration between Cubes"

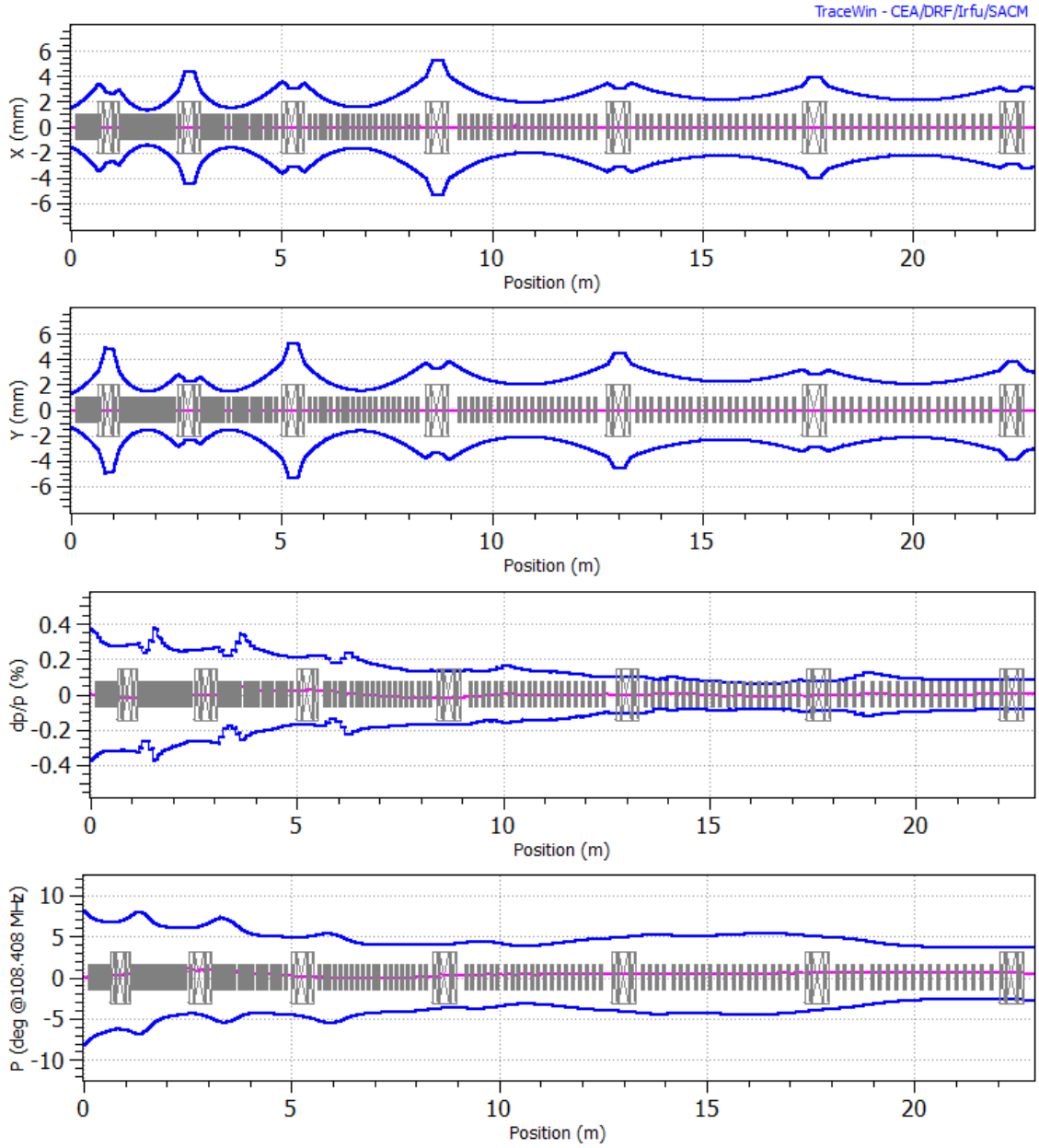

Figure 6.19: RMS beam envelopes for the transverse and longitudinal planes.

The transverse beam envelopes for one RMS width of the beam are shown in Figure 6.19. They match well in shape with the beam envelopes calculated using LORASR in Figures 6.5 and 6.8. In addition to plotting beam envelopes, TraceWin allows for plotting of the particle densities over the whole simulation range. In Figure 6.20, the resulting plots of the transverse and longitudinal particle densities are shown. This way additional observations on the beam dynamics are possible.

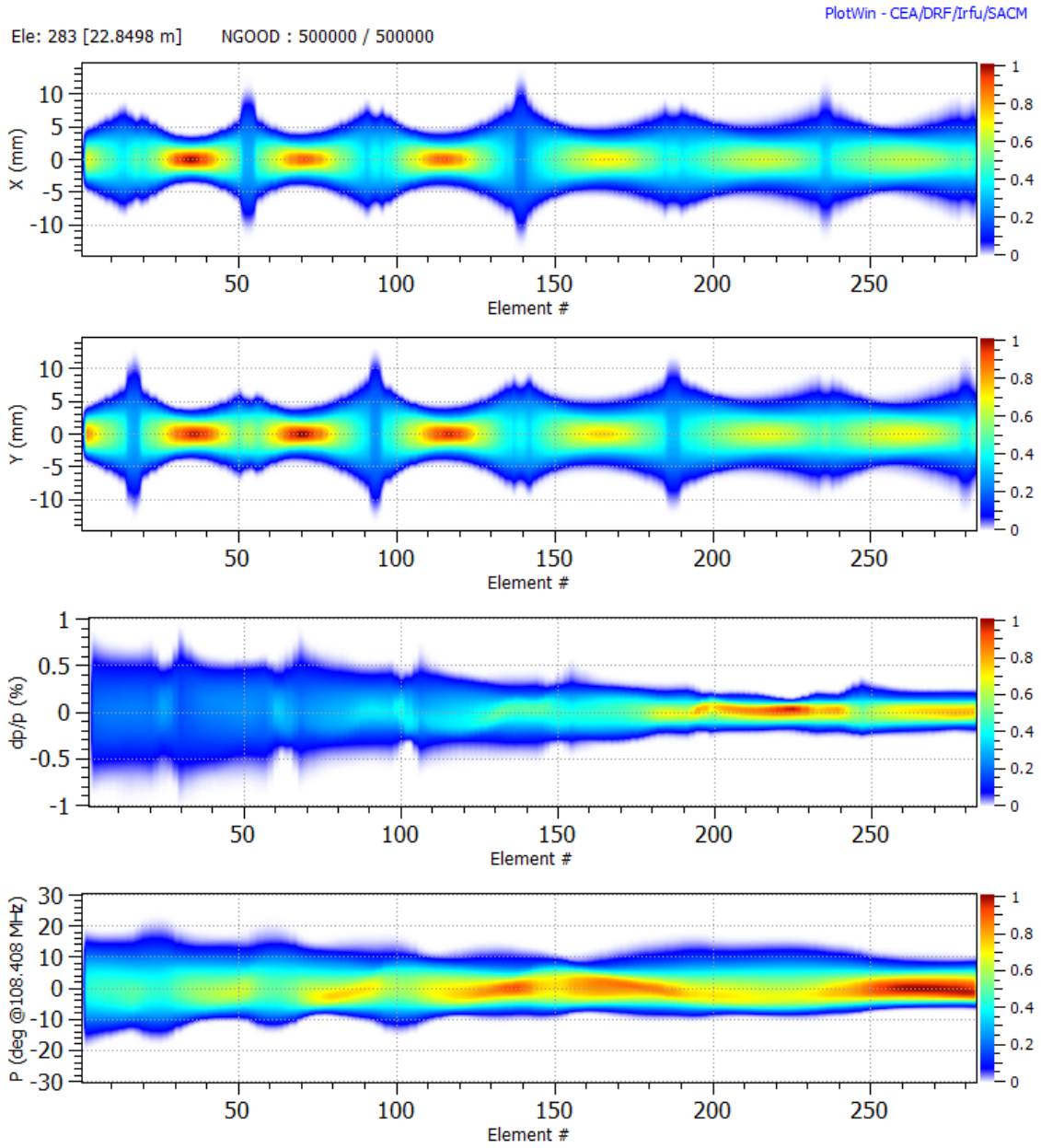

Figure 6.20: Particle densities for the transverse and longitudinal planes calculated with $5 \cdot 10^5$ particles.

For example, from the transverse density plots, the decreased phase advance for the last three sections is much more obvious due to the decreased core density between the triplet lenses. From Figure 6.21 it is obvious, that the RMS emittance growth progression calculated with TraceWin differs quite a bit from the LORASR simulations (see Figure 6.11). Nevertheless, the resulting transverse emittance growth value of $\Delta\epsilon_{\mathrm{x/y,rms}} = 23\,\%$ is close to the value calculated with LORASR

($\Delta\epsilon_{x,rms} = 27.5\,\%$ and $\Delta\epsilon_{y,rms} = 25.8\,\%$). In the TraceWin simulations, a sudden increase by a factor of two in emittance is observed between sections four and five that is not observed in LORASR simulations (see Figure 6.11). Interestingly, this transverse emittance growth coincides with a decrease in longitudinal emittance, hinting towards a possible emittance transfer in the second half of the linac. Looking at the particle distribution at the exit of the linac, the overall result is similar to that of the LORASR simulations, even the smearing out of the longitudinal particle distribution towards more positive phases is reproduced.

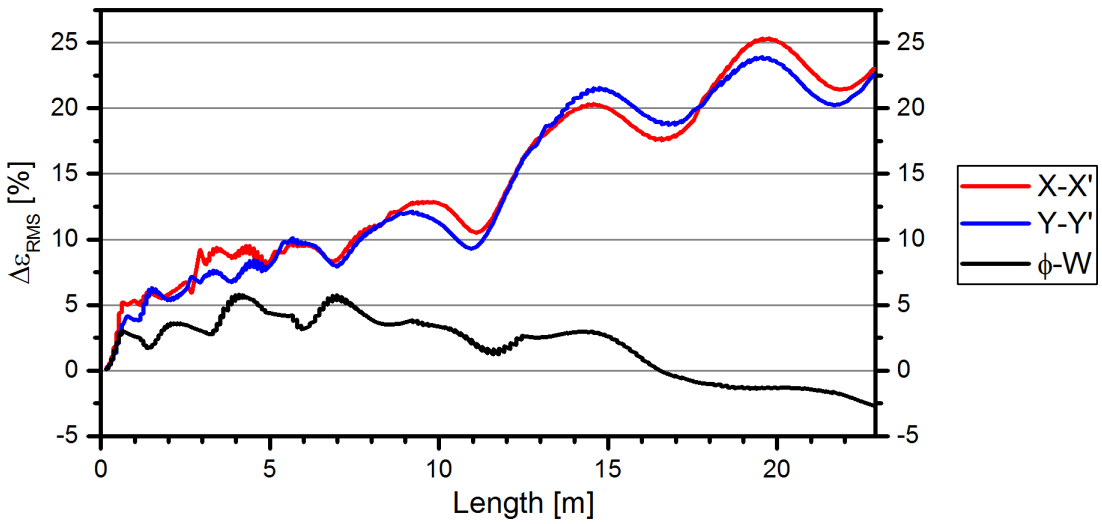

Figure 6.21: RMS emittance growth progression for the IH-DTL calculated with TraceWin.

As seen in Figure 6.22, the most obvious difference in the transverse particle distribution to the LORASR simulations (compare Figure 6.9), is the formation of additional extending features at the ellipse waist. Possible reasons for the differences between the two codes' results are manifold. First of all, the TraceWin calculations were performed using a thin accelerating gap approximation while LORASR uses parametric field maps and calculates 30 steps for each accelerating gap in contrast to just one step in TraceWin simulations. Secondly, the different space charge routines may be another reason for differences in the results. While both codes use a 3D PIC solver, the definition of the calculated mesh is different. In LORASR a mesh with symmetrical dimensions (e.g. 128x128x128 mesh cells in $x/y/z$ respectively) is generated, limited in space by the aperture of the drift tubes and the half period length for each gap. In TraceWin the mesh can also be chosen to have symmetrical

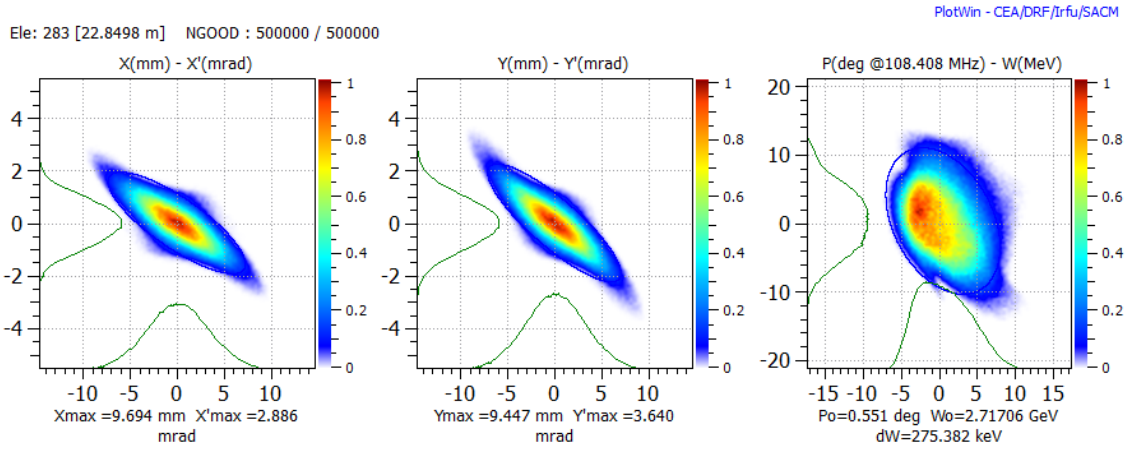

Figure 6.22: Output particle distribution for the poststripper IH-DTL with $5 \cdot 10^5$ particles.

numbers of mesh cells. The boundaries of the PIC mesh are defined by multiples of the beams RMS widths in all the dimensions (e.g. $3.5 \cdot \sigma$ in $x/y/z$), while outside of the PIC grid space charge forces of an equivalent Gaussian beam are calculated.

In summary, the overall results of the simulations with LORASR and TraceWin agree well while some differences in the exact structure of the beam occur due to differences in the calculation methods. Both codes, however, confirm a stable beam acceleration for this KONUS lattice.

6.3 Error Studies

Error studies play an important role in the design of particle accelerators. Usually the design of a linac is calculated with a perfectly matched input distribution well within the acceptance of the linac. In addition, all element positions and orientations as well as RF-phases and -amplitudes are assumed to be without error. This way the performance of the linac is usually judged by the achieved transmission and emittance growth of these ideal simulations. This however can only be the first step when judging the quality of a linac design. A real world accelerator has to deal with all kinds of imperfections. The manufacturing of magnetic lenses and RF-cavities typically includes tolerances in the order of $50 - 100\,\mu m$. Additionally, the components' alignment during assembly of the linac also includes some margin of error also in the 100 µm range. An example for a random distribution of quadrupole alignment errors is shown in Figure 6.23.

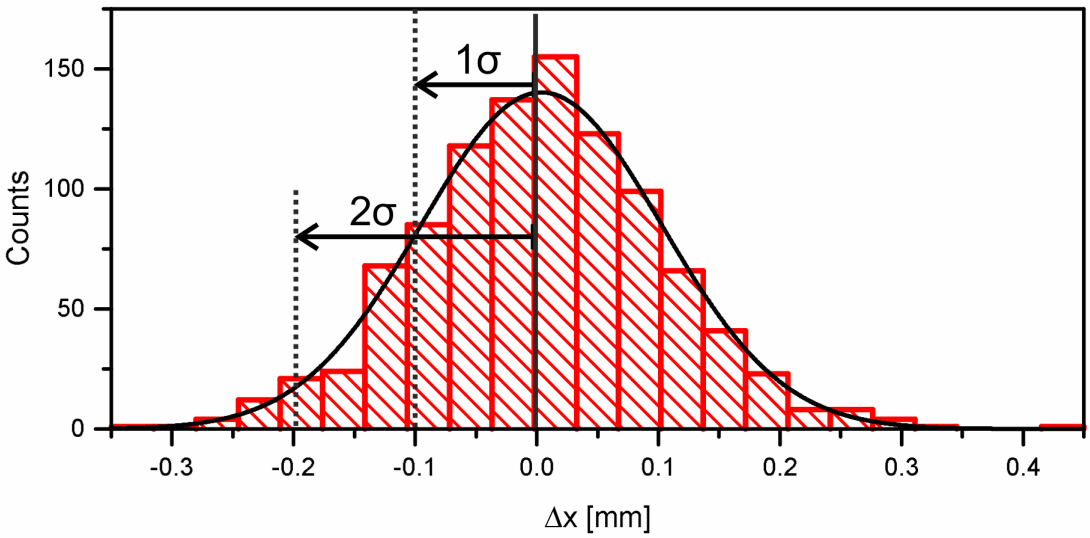

Figure 6.23: Gaussian error distribution with $N = 1000$ for $\Delta x_{quad} = 0.2\ mm$ (2σ).

Further sources for errors are the RF-phase and -amplitude settings and the alignment of drift tubes in the cavities, influencing the individual gap voltages. Furthermore the impact of an erroneous beam injection has to be considered as well. An investigation of the behavior of a linac under such conditions is key to defining tolerances for manufacturing and alignment of components. Thus, extensive error studies using multi-particle simulation codes is good practice in the linac design process. In the following, error studies for the poststripper IH-DTL are presented. As

a first step, the influence of individual component errors is investigated. Based on those results, simulations with multiple different component errors are performed. Additionally the influence of corrective steering elements is also investigated.

6.3.1 Simulation Parameters

All following error studies simulations were performed with TraceWin in multi-particle mode (PARTRAN). The number of macro particles was chosen to be $N_{\text{part}} = 10^4 - 10^5$. Again, the space charge solver used in TraceWin is PICNIC (3D), however due to the lower particle number, a mesh of 14x14x14 cells (in $x/y/z$) was used. The randomized errors were generated for $N_{\text{run}} = 1000$ different linac error settings and are distributed by Gaussian normal distributions (see Figure 6.23). This means, that for each error type, $N_{\text{run}} = 1000$ simulations of the linac were performed with different random errors for each simulation run. All error values stated in the following chapters are the two RMS value 2σ of the Gaussian distribution for the corresponding component (e.g. $\Delta x = \pm 100\,\mu\text{m}$ means $2 \cdot \sigma_x = 100\,\mu\text{m}$). To define tolerances based on these simulations, it is reasonable to allow the maximum error to be within 2σ of the simulated distribution, corresponding to 95.45 % of all errors generated.

Combining the number of runs and the number of particles per simulation, the following error studies were performed with a total number of calculated particles from $N_{\text{total}} = 10^7$ to 10^8. Parameter sweeps for different isolated errors were calculated with the lower $N_{\text{total}} = 10^7$, using only $N_{\text{part}} = 10^5$ macro particles, since only the sensitivity to the different error types and their magnitude was of interest. Combined runs with an ensemble of errors were calculated with high $N_{\text{total}} = 10^8$ with $N_{\text{part}} = 10^6$ macro particles to provide reliable statistics for the resulting particle losses and emittance growth values. All results shown in the following are calculated relative to the output of the normal simulation without errors.

6.3.2 Influence of Different Error Types

Table 6.5: Investigated error types for the poststripper IH-DTL.

Error Type	**Range** (2σ)	**Linac Sensitivity**
Quadrupole Lenses		
Singlet displacement (x/y)	$0-200\,\mu m$	high sensitivity (losses)
Singlet rotation ($\phi_X/\phi_Y/\phi_Z$)	$0-7\,mrad$	low sensitivity
Gradient error dB'/B'_0	$0-2\,\%$	low sensitivity $\Delta\epsilon_{trans}$ / losses
Triplet displacement (x/y)	$0-600\,\mu m$	low sensitivity
Triplet rotation ($\phi_X/\phi_Y/\phi_Z$)	$0-4\,mrad$	high sensitivity (losses)
Cavities		
Cavity field dE/E_0	$0-1\,\%$	linear increase in energy jitter
Cavity phase $d\phi$	$0-2^\circ$	linear increase in energy jitter
Single gap field dE/E	$0-5\,\%$	high sensitivity $\Delta\epsilon_{long}$
Cavity displacement (x/y)	$0-1\,mm$	low sensitivity
Input Beam		
Beam displacement (x/y)	$\pm 2\,mm$	losses
Beam tilt (ϕ_X/ϕ_Y)	$\pm 4\,mrad$	losses and $\Delta\epsilon_{trans}$
Energy offset	$\pm 2\,MeV$	$\Delta\epsilon_{long}$ and ΔW
Phase offset	$\pm 5^\circ$	$\Delta\epsilon_{long}$ and ΔW

The first investigation in this error study is aimed at the sensitivity of the design to the different possible errors that can occur in a linac. Therefore for each error type a dedicated error study was performed. In these error studies, several calculations with increasing error magnitude were performed to find a limit for each single error type. The errors are always distributed by a Gaussian distribution as stated above (see Figure 6.23). These sensitivity error studies were performed without any steering correction in the linac to find the intrinsic limits of the design. The investigated error types and a short summary of the following results can be found in Table 6.5.

The biggest impact on particle losses were found to be the displacement of quadrupole singlets within the triplets and the rotation of the triplet itself, whereas singlet rotation and triplet displacement seem much less critical. Cavity field level errors and

input phase errors have an influence on the output energy and longitudinal emittance growth. In the following, the individual investigations will be described in detail.

6.3.3 Quadrupole Errors

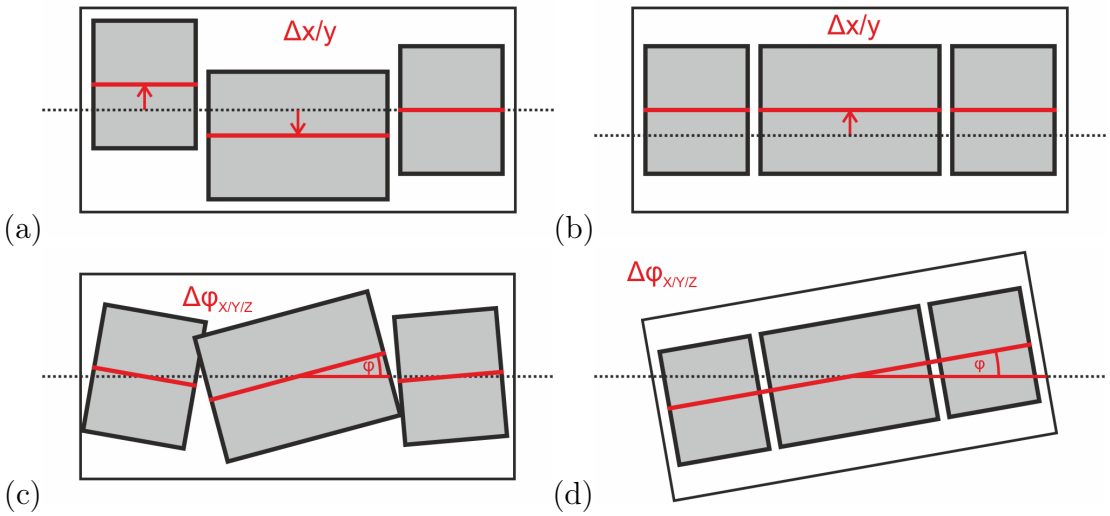

Figure 6.24: Definition of the different quadrupole error types: singlet displacement (a), triplet displacement (b), singlet rotation (c), and triplet rotation (d).

For a magnetic quadrupole triplet, a number of different errors can occur during manufacturing, alignment and operation. The first error type is the displacement in the horizontal and vertical direction (see Figure 6.24 (a) and (b)). This displacement can occur during the assembly of the triplet where the singlets making up the triplet can only be placed to a certain accuracy. Following that, during the assembly and alignment of the cavities, the triplet as a whole can only be positioned to a certain accuracy. The same is true for the rotation of the quadrupole singlets and triplets around all three axes (see Figure 6.24 (c) and (d)). This rotation of the triplet also includes the resulting displacement of the outer singlets. Another source for errors during operation is the variation of the quadrupole gradients which will also be investigated. Errors of the focusing quadrupole magnets can typically lead to additional emittance growth and particle losses. However, the longitudinal beam motion and linac output energy are not affected noticeably by magnet errors.

The displacement of quadrupole singlets was investigated up to $\Delta xy = \pm 200\,\mu\text{m}$

(see Figure 6.26). Until $\Delta xy = \pm 80\,\mu\text{m}$ displacement, the losses are close to zero and only reach $N_{\text{loss}}/N < 0.4\,\%$. At $\Delta xy = \pm 100\,\mu\text{m}$ displacement, the losses are at $N_{\text{loss}}/N = 1.38\,\%$ with a maximum additional emittance growth of $\Delta\epsilon_{\text{trans}} < 2.5\,\%$. Following that, the losses start to increase significantly beyond singlet displacements of $\Delta xy > \pm 120\,\mu\text{m}$ also leading to a reduction in emittance growth due to the significant scraping of outer particles. An example for significant losses due to large singlet displacement is shown in Figure 6.25.

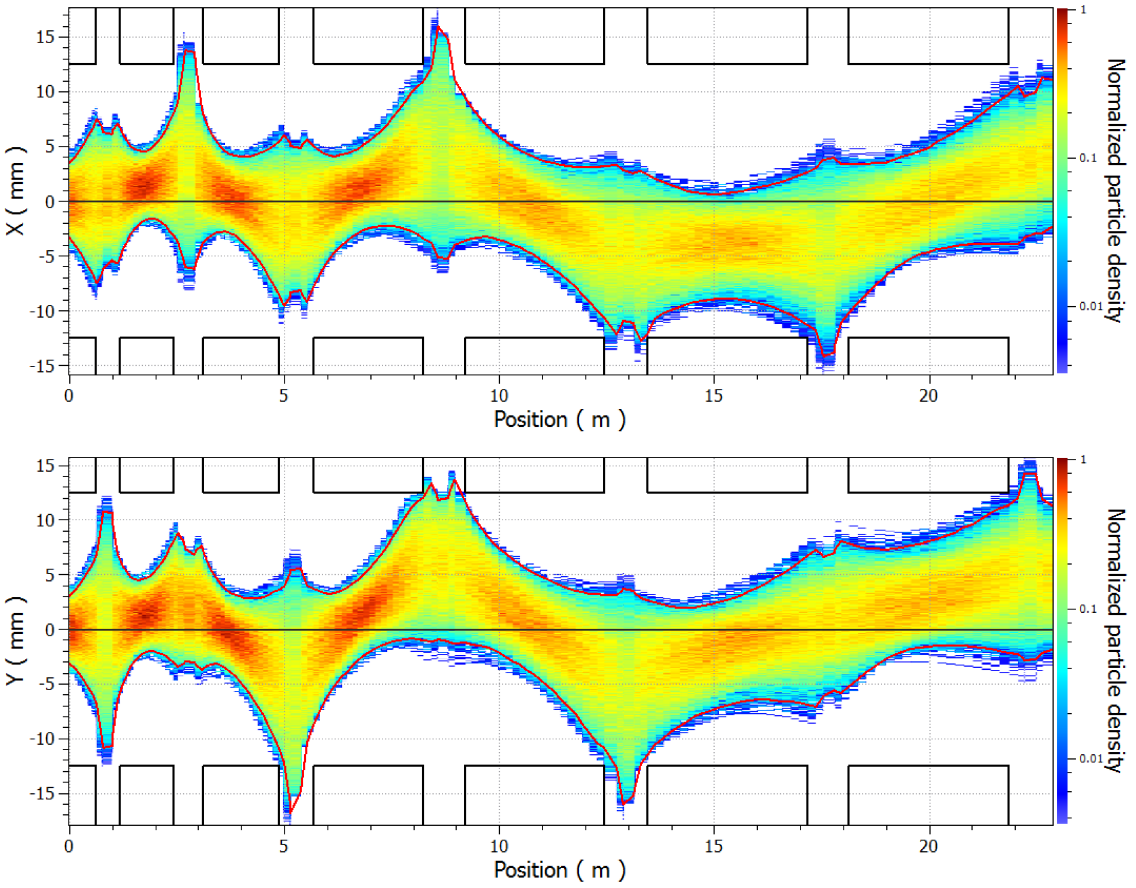

Figure 6.25: Particle densities for a scenario where significant losses are caused by large singlet displacement errors of up to $\Delta\phi_{x/y/z} = \pm 200\,\mu\text{m}$.

A rotation of the quadrupole singlets around all three axes was simulated with a maximum value of $\Delta\phi_{x/y/z} = \pm 7\,\text{mrad}\,(0.4°)$ (see Figure 6.27). The most significant influence of the quadrupole singlet rotation is an increased transverse emittance growth. Maximum losses at $\Delta\phi_{x/y/z} = \pm 7\,\text{mrad}$ are only $N_{\text{loss}}/N = 0.03\,\%$ and no losses are observed until $\Delta\phi_{x/y/z} = \pm 5\,\text{mrad}$. Therefore, losses can be neglected in this scenario. The transverse emittance growth stays below $\Delta\epsilon_{\text{trans}} = 3\,\%$ for rota-

tions $\Delta\phi_{x/y/z} < \pm 2\,\mathrm{mrad}$ and below $\Delta\epsilon_{\mathrm{trans}} = 5\,\%$ for $\Delta\phi_{x/y/z} < \pm 5\,\mathrm{mrad}$. Beyond that an almost linear increase of emittance growth is observed until a maximum value of $\Delta\epsilon_{\mathrm{trans}} = 17\,\%$ at $\Delta\phi_{x/y/z} = \pm 7\,\mathrm{mrad}$.

The magnetic field gradients B' in the quadrupoles were varied up to $\Delta B'/B'_0 = \pm 2\,\%$ of their design values (see Figure 6.28). For the maximum value of $\Delta B'/B'_0 = \pm 2\,\%$, losses of only $N_{\mathrm{loss}}/N = 2.15\,\%$ and a transverse emittance growth of $\Delta\epsilon_{\mathrm{trans}} = 5\,\%$ are observed. Gradient variations of below $\Delta B'/B'_0 = \pm 1\,\%$ have a negligible effect on beam dynamics.

A displacement of quadrupole triplets was investigated up to $\Delta xy = \pm 600\,\mu\mathrm{m}$ in the horizontal and vertical direction (see Figure 6.29). In contrast to the random displacement of quadrupole singlets, the displacement of the triplets is much less critical for the performance of the linac. Over the whole range of $\Delta xy = 0 - \pm 600\,\mu\mathrm{m}$ the additional transverse emittance growth is below $\Delta\epsilon_{\mathrm{trans}} = 1\,\%$ and therefore negligible. For triplet displacement of less than $\Delta xy = \pm 240\,\mu\mathrm{m}$ the losses are below $N_{\mathrm{loss}}/N = 0.1\,\%$. After that the losses grow to a maximum value of $N_{\mathrm{loss}}/N = 5.9\,\%$ for a triplet displacement of $\Delta xy = \pm 600\,\mu\mathrm{m}$. The alignment of triplet lenses can be achieved with an accuracy in the order of $\Delta xy = \pm 100\,\mu\mathrm{m}$, which is more than sufficient judging by the error studies performed.

Finally, the rotation of full quadrupole triplets was also studied for errors as large as $\Delta\phi = 4\,\mathrm{mrad}$. Losses are below $N_{\mathrm{loss}}/N = 0.05\,\%$ for triplet rotations of $\Delta\phi < 1.2\,\mathrm{mrad}$. For higher rotation angles losses increase slowly to $N_{\mathrm{loss}}/N = 1\,\%$ at $\Delta\phi = 2\,\mathrm{mrad}$. The highest value observed is $N_{\mathrm{loss}}/N = 19.4\,\%$ for the maximum rotation value of $\Delta\phi = 4\,\mathrm{mrad}$.

Singlet displacement Δxy up to 200 µm

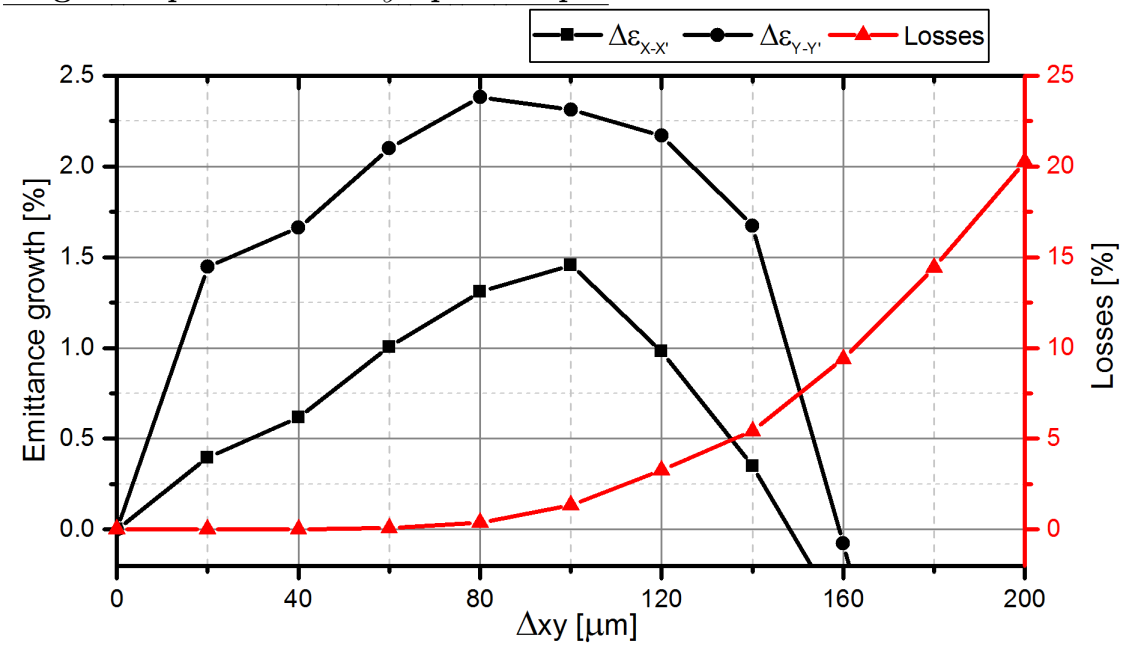

Figure 6.26: Results of error studies for the displacement of quadrupole singlets.

Singlet rotation errors $\Delta\phi_{x/y/z}$ up to 7 mrad

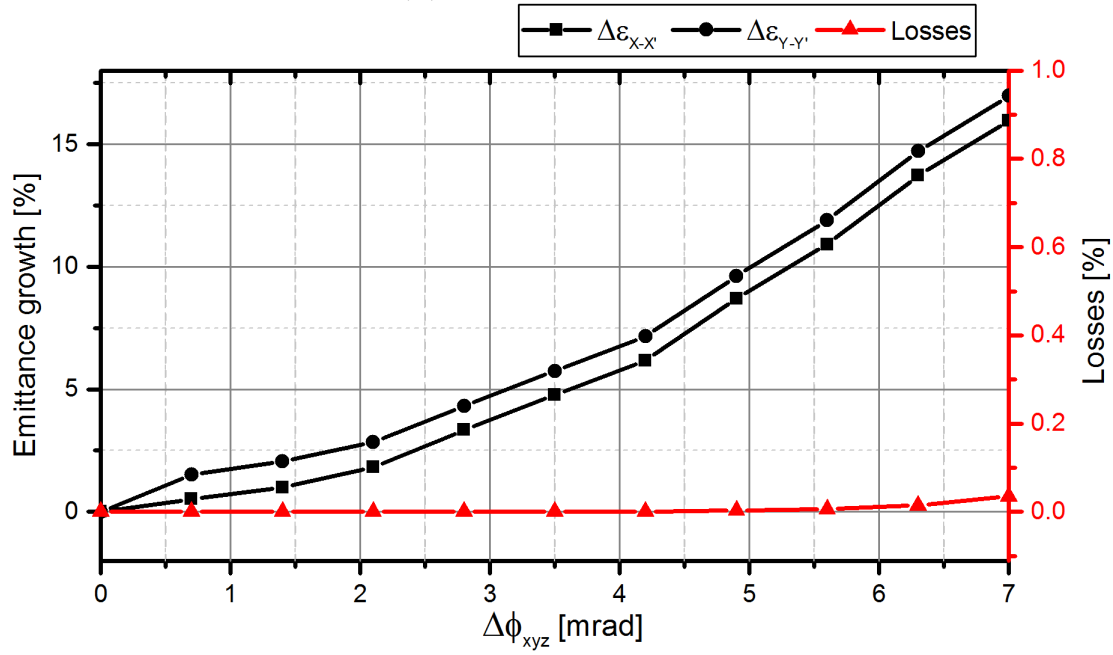

Figure 6.27: Results of error studies for the rotation of quadrupole singlets.

Singlet gradient errors $\Delta B'/B'_0$ up to 2 %

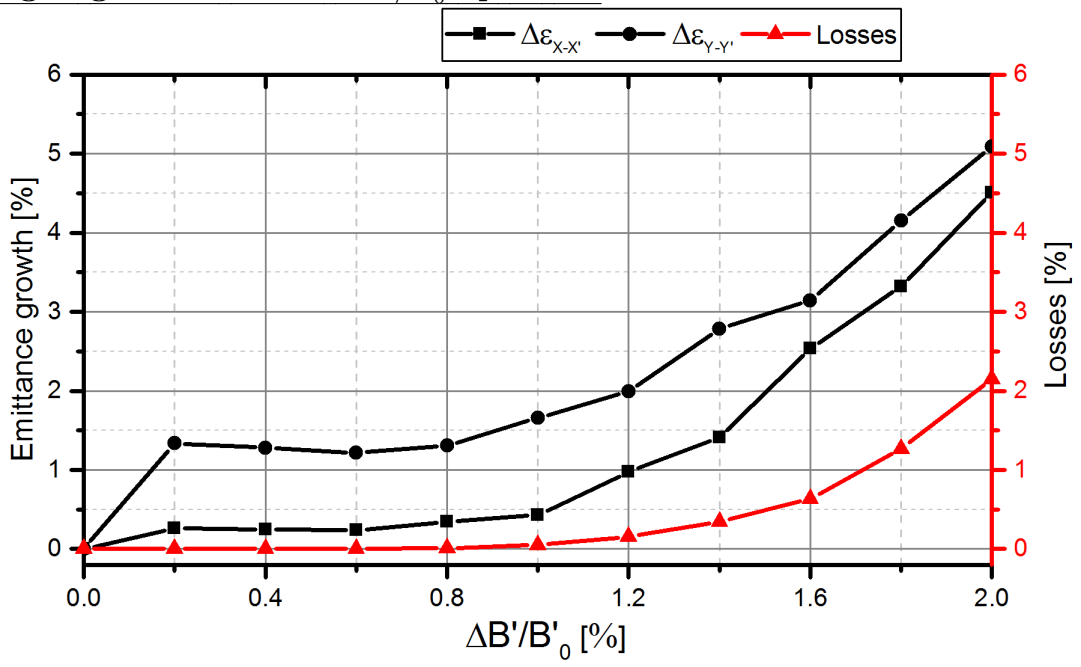

Figure 6.28: Results of error studies for gradient variation dB'/B'_0.

Triplet displacement Δxy up to 600 µm

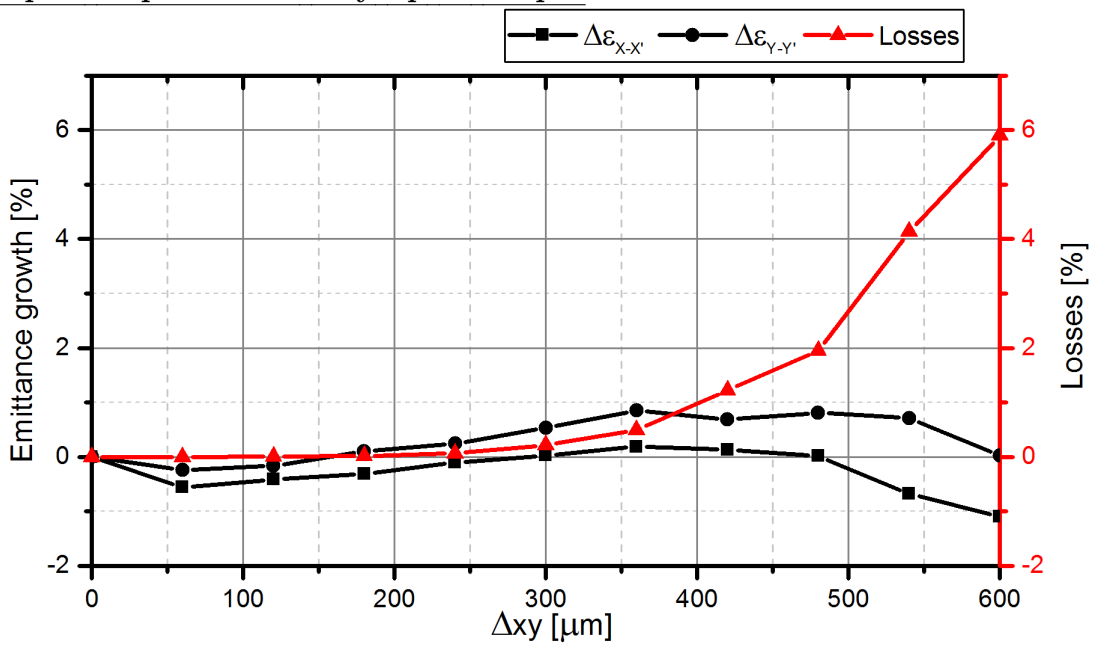

Figure 6.29: Results of error studies for the displacement of quadrupole triplets.

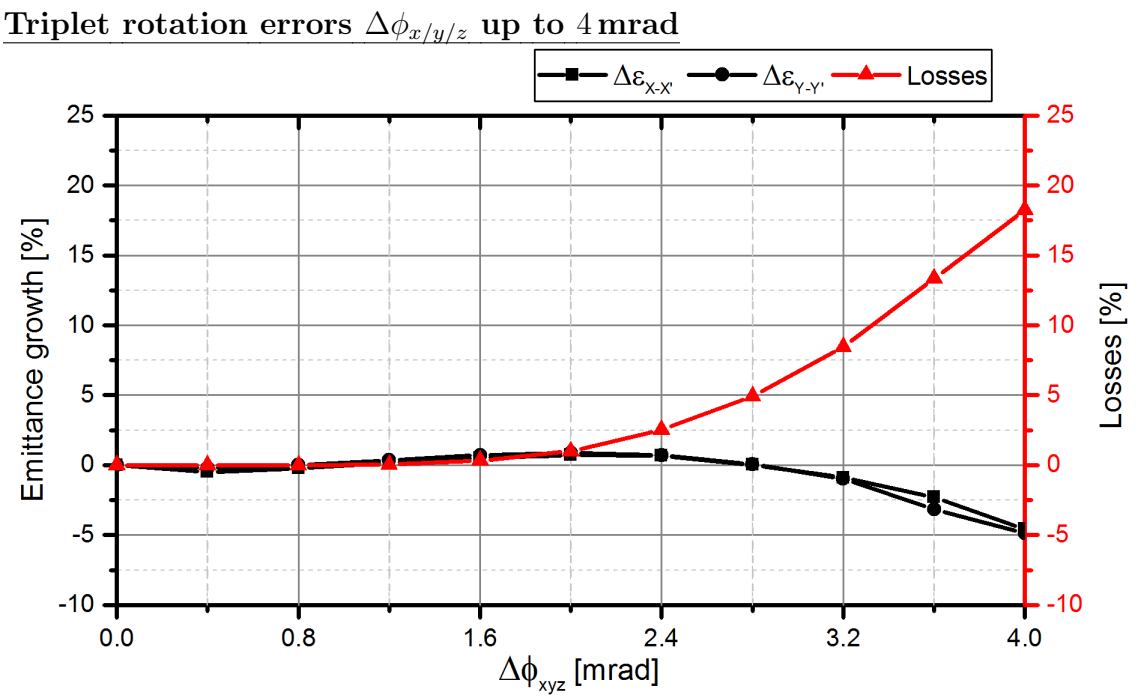

Figure 6.30: Results of error studies for the rotation of quadrupole triplets.

Some interesting details were revealed by the investigation of individual contributions from the different error types of the seven magnetic triplet lenses. The most critical value by far is the accurate positioning of the quadrupole singlets within $\Delta xy < \pm 80\,\mu\text{m}$ towards the beam axis of each triplet. Therefore the requirements for manufacturing the magnets should be very strict. A rotation of the individual singlets, however, is not critical in terms of losses. For $\Delta\phi = \pm 7\,\text{mrad}$ rotation accuracy losses of only $N_{\text{loss}}/N = 0.03\,\%$ were calculated. Yet, significant emittance growth can be introduced by large rotation angles. Allowing a singlet rotation of $\Delta\phi < 1\,\text{mrad}$ ensures low emittance growth in addition to the low losses. The differentiation between singlet and triplet errors revealed, that triplet displacement is not a critical parameter. Even for a triplet displacement of $\Delta xy = 360\,\mu\text{m}$ the calculated losses lie below $N_{\text{loss}}/N = 0.5\,\%$. Therefore a typical required accuracy of $\Delta xy = \pm 100\,\mu\text{m}$ will be more than sufficient to ensure reliable operation. In contrast, the rotation angle of the quadrupole triplets has an important influence on the beam dynamics. Rotation angles of less than $\Delta\phi = 1.6\,\text{mrad}$ should be achieved to keep loss contribution low. Higher values can lead to significant losses. The accuracy of the magnetic gradient in the triplets is a non critical parameter. Values of much less than $\Delta B'/B'_0 = \pm 0.7\,\%$ should be easily achieved by the magnet controls.

In summary, the most critical errors for quadrupole triplet lenses are the displacement of the individual singlets and the rotation of the triplets as a whole. In Table 6.6 the error limits are summarized that are considered "safe". The criteria for this is that only losses lower than $N_{\text{loss}}/N = 0.5\,\%$ and additional emittance growths lower than $\Delta\epsilon_{\text{trans}} = 2\,\%$ are allowed. It should be noted, that these limits are the result of simulations without steerer corrections. With the use of steerer corrections, much larger errors can be tolerated (see section 6.3.7).

Table 6.6: Summary of lens error tolerances of the linac based on simulations.

Parameter	**Safe Limit**	**Limitation**
Singlet displacement (x/y)	80 µm	Losses $< 0.5\,\%$
Singlet rotation $(\phi_X/\phi_Y/\phi_Z)$	1 mrad	$\Delta\epsilon_{\text{trans}} < 2\,\%$
Gradient error dB'/B'_0	0.7 %	Losses $< 0.5\,\%$, $\Delta\epsilon_{\text{trans}} < 2\,\%$
Triplet displacement (x/y)	360 µm	Losses $< 0.5\,\%$
Triplet rotation $(\phi_X/\phi_Y/\phi_Z)$	1.6 mrad	Losses $< 0.5\,\%$

6.3.4 Cavity Errors

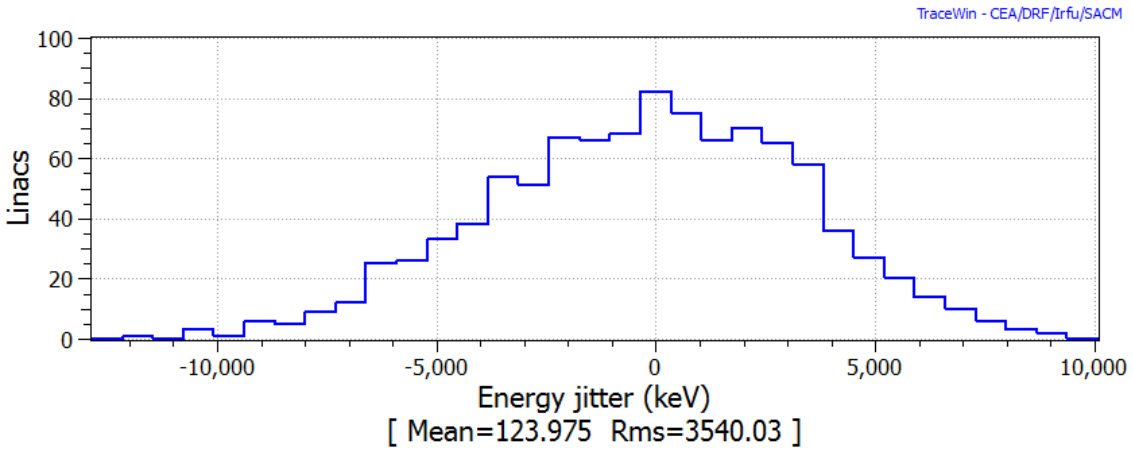

Figure 6.31: Distribution of linac output energies for 1000 runs and a maximum cavity field variation of $\Delta E/E_0 = \pm 1\,\%$.

For the RF-cavities of the linac, four types of errors were investigated. When the cavity is placed into the beamline during assembly of the linac, accurate positioning towards the beam axis is necessary. The possible displacement of cavities in the

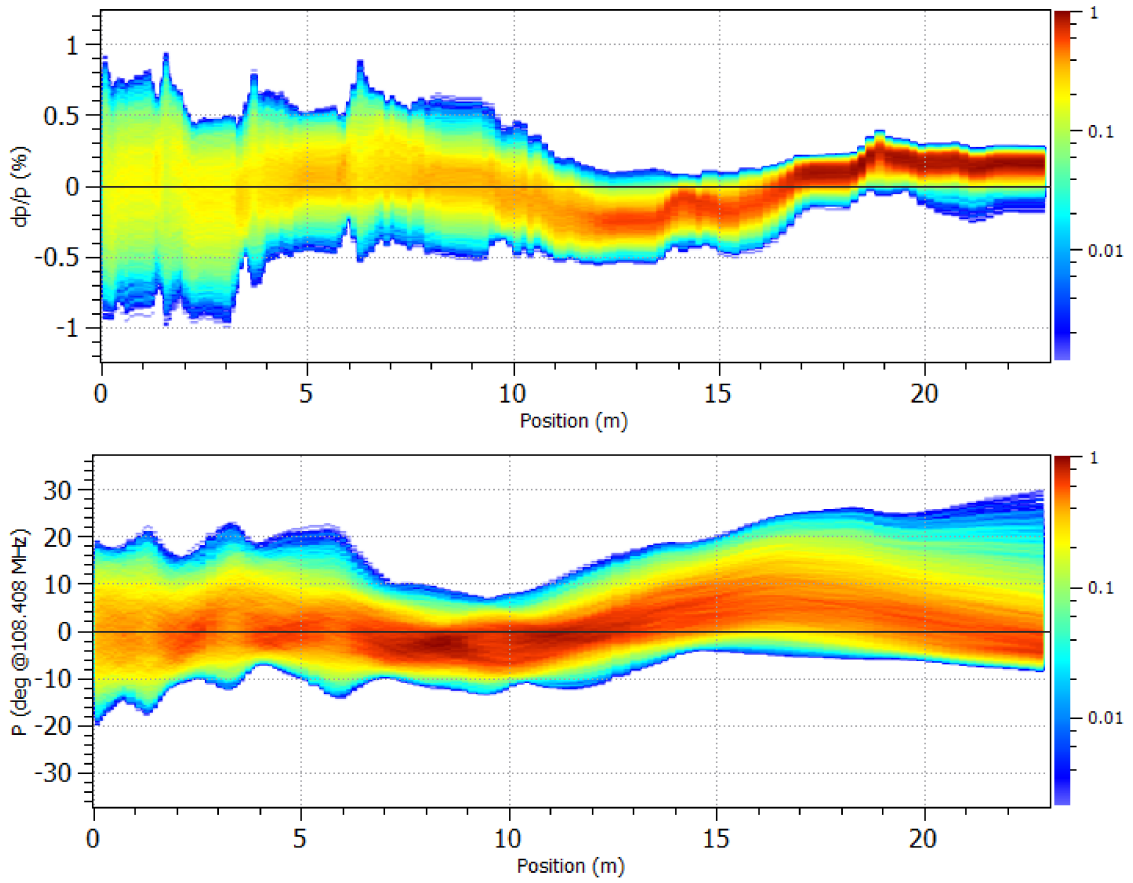

Figure 6.32: Longitudinal particle densities for a scenario with gap field errors of up to $\Delta E_{\mathrm{gap}}/E_{\mathrm{gap},0} = \pm 5\,\%$.

horizontal and vertical plane was investigated in this error study. Additional sources of error during operation of the linac are the cavity field level and the cavity RF-phase. Also the variation of gap voltages due to inaccuracies in the positioning of the drift tubes was investigated. Cavity displacement can have an influence on transverse emittance growth and lead to particle losses. Errors in the cavity field, phase and gap voltage have an influence on the linac exit energy and on longitudinal emittance growth. The influence on the linac exit energy can be related to the statistic energy jitter of the error studies simulations. The energy jitter corresponds to the RMS value of the distribution of all output energies of the 1000 simulation runs performed for each data point. An example for this energy distribution is shown in Figure 6.31.

Cavity field levels were varied in these errors studies by a maximum of $\Delta E/E_0 = \pm 1\,\%$ (see Figure 6.33). The resulting additional longitudinal emittance growth is $\Delta\epsilon_{\mathrm{long}} = 5.14\,\%$ for the highest field error of $\Delta E/E_0 = 1\,\%$. This leads to a

maximum energy jitter of $\Delta W_{\mathrm{rms}} = 3.54\,\mathrm{MeV}$, which is 1.3 ‰ of the linac output energy. In the investigated parameter range, the energy jitter scales linearly with the field variation. Cavity phase errors were investigated up to a maximum error of $\Delta\phi = \pm 2^{\circ}$ (see Figure 6.34). The maximum emittance growth is $\Delta\epsilon_{\mathrm{long}} = 5.67\,\%$ for a phase error of $\Delta\phi = \pm 2^{\circ}$. With increasing phase error, the energy jitter also increases linearly. A maximum energy jitter of $\Delta W_{\mathrm{rms}} = 2.98\,\mathrm{MeV}\,(1.1\,‰)$ is observed. For each cavity, voltage errors of the individual gaps were investigated up to $\Delta E_{\mathrm{gap}}/E_{\mathrm{gap,0}} = \pm 5\,\%$ (see Figure 6.35). At random gap voltage errors of below $\Delta E_{\mathrm{gap}}/E_{\mathrm{gap,0}} = \pm 2\,\%$ the effects on beam quality are moderately low with longitudinal emittance growth of less than $\Delta\epsilon_{\mathrm{long}} = 2\,\%$ with an energy jitter of $\Delta W_{\mathrm{rms}} = 1.88\,\mathrm{MeV}\,(0.7\,‰)$ which again scales linearly with error magnitude. For $\Delta E_{\mathrm{gap}}/E_{\mathrm{gap,0}} = 3\%$ the additional longitudinal emittance growth is $\Delta\epsilon_{\mathrm{long}} = 5.93\,\%$. Beyond that, significant emittance growth of $\Delta\epsilon_{\mathrm{long}} = 10 - 35\,\%$ is possible, and therefore gap field errors of more than $\Delta E_{\mathrm{gap}}/E_{\mathrm{gap,0}} = \pm 3\,\%$ are not acceptable. An example for large gap field errors that lead to strong influence on the longitudinal beam motion is shown in Figure 6.32.

The results for a cavity displacement of up to $\Delta xy = \pm 1000\,\mu\mathrm{m}$ show that this is the least sensitive error type (see Figure 6.36). Even for a maximum displacement of $\Delta xy = \pm 1000\,\mu\mathrm{m}$ the simulated losses are below $N_{\mathrm{lost}}/N = 0.05\,\%$ and additional transverse emittance growth is below $\Delta\epsilon_{\mathrm{trans}} = 3.5\,\%$.

Cavity field errors $\Delta E/E_0$ up to 1 %

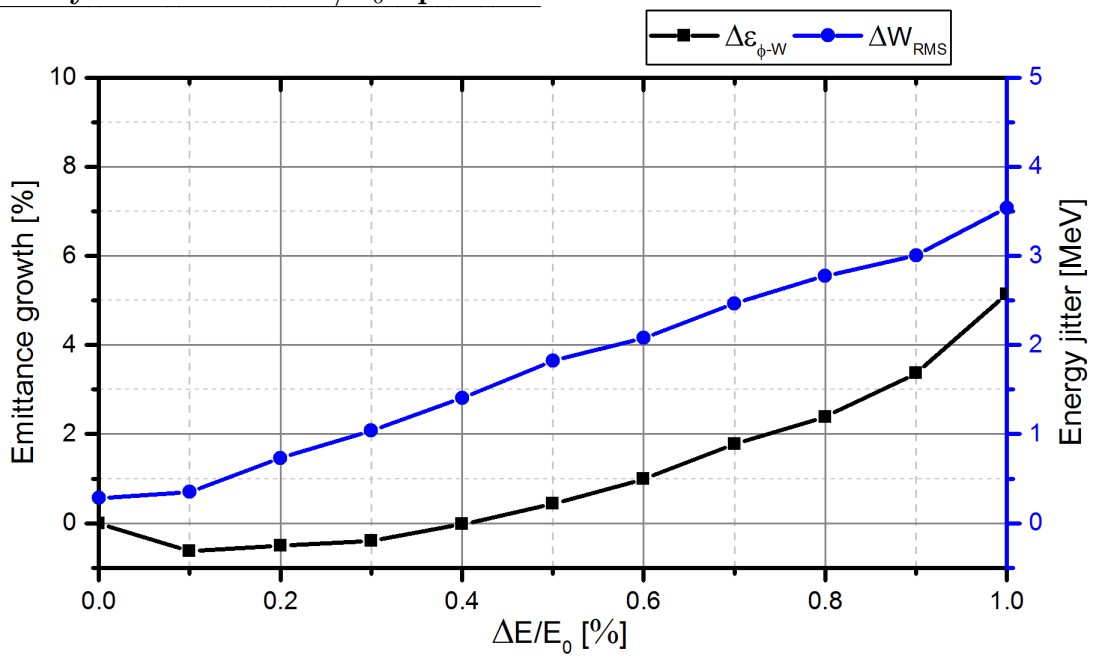

Figure 6.33: Results of error studies with cavity field level errors.

Cavity phase errors $\Delta\phi$ up to 2°

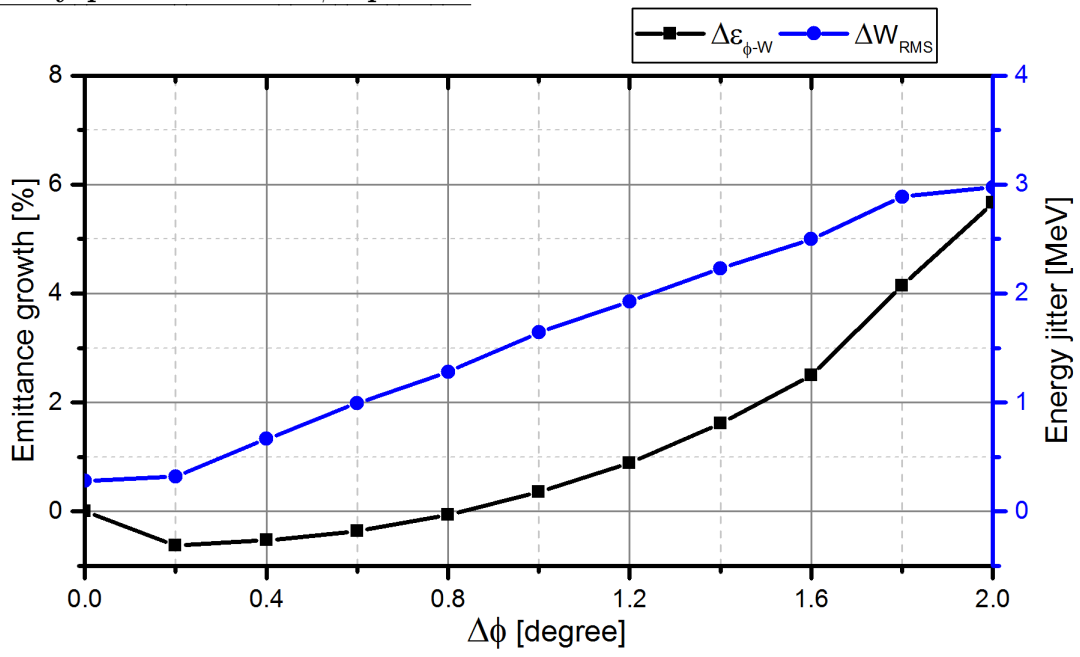

Figure 6.34: Results of error studies with cavity phase errors.

Gap field errors $\Delta E_{gap}/E_{gap,0}$ up to 5 %

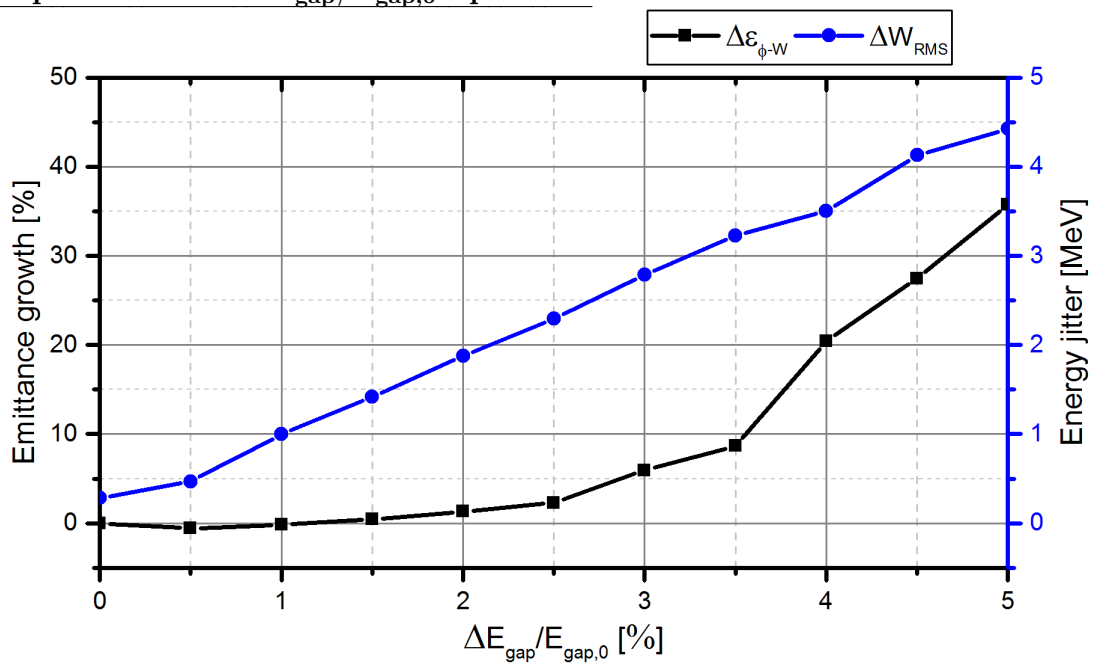

Figure 6.35: Results of error studies with gap field errors.

Cavity displacement Δxy up to 1000 µm

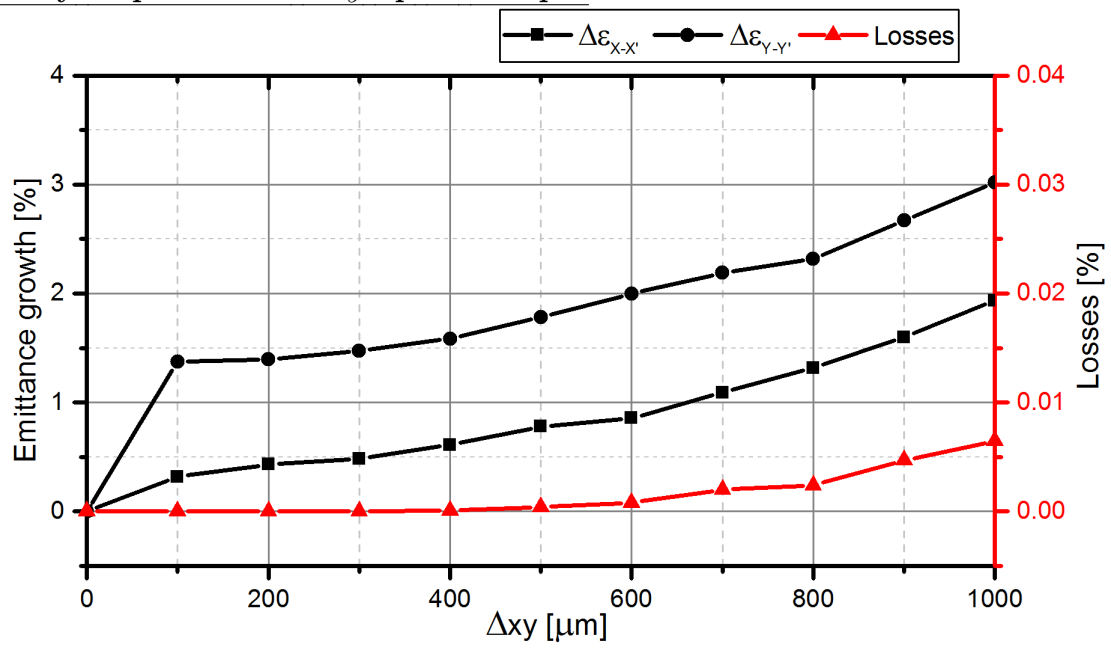

Figure 6.36: Results of error studies with cavity displacement.

Investigation of the different error types for cavities reveals, that on first glance the placement of the cavities is not a critical issue, even for large displacements of up to $\Delta xy = \pm 1\,\mathrm{mm}$. However, it is expected that in combination with errors in the focusing elements a large cavity displacement will increase losses significantly, since essentially the aperture in two directions is reduced if the cavity is shifted horizontally and vertically. Therefore accuracies in the $\Delta xy = \pm 100\,\mu\mathrm{m}$ range would still be advisable. All errors related to the RF field induce some longitudinal emittance growth and potentially shift the output energy in the per mille range. However, the shift in energy could be compensated as long as those errors are static. Dynamic field and phase errors are typically lower by orders of magnitude than the investigated values. For the definition of safe error values the allowed additional longitudinal emittance growth was defined as $\Delta\epsilon_{\mathrm{long/trans}} < 2\,\%$ (see Table 6.7). The energy jitter for the given safe values is stated as well.

Table 6.7: Summary of cavity error tolerances of the linac based on simulations.

Parameter	**Safe Limit**	**Limitation**	$\Delta W_{\mathrm{rms}}\,(‰\,of\,W_{\mathrm{out}})$
Cavity field $\Delta E/E_0$	0.7 %	$\Delta\epsilon_{\mathrm{long}} < 2\,\%$	2.47 MeV (0.91 ‰)
Cavity phase $\Delta\phi$	1.4°	$\Delta\epsilon_{\mathrm{long}} < 2\,\%$	2.23 MeV (0.82 ‰)
Gap voltage $\Delta E_{\mathrm{gap}}/E_{\mathrm{gap},0}$	2 %	$\Delta\epsilon_{\mathrm{long}} < 2\,\%$	1.88 MeV (0.69 ‰)
Cavity displacement (x/y)	600 µm	$\Delta\epsilon_{\mathrm{trans}} < 2\,\%$	—

6.3.5 Input Beam Errors

The influence of the input beam parameters on the ideal linac model without errors was investigated to find the limitations of the design with respect to fluctuations and misadjustments of the injection. The input beam energy was varied by $\Delta W_{\mathrm{in}} = \pm 2\,\mathrm{MeV}$ which is 6 ‰ of the injection energy of $W_{\mathrm{in}} = 333.2\,\mathrm{MeV}$. One resulting effect is a maximum shift in output energy of $\Delta W_{\mathrm{neg}} = -2.6\,\mathrm{MeV}$ and $\Delta W_{\mathrm{pos}} = 4.2\,\mathrm{MeV}$ (see Figure 6.37 (a)). Significant emittance growth in the longitudinal plane of up to $\Delta\epsilon_{\mathrm{long}} = 41.4\,\%$ is observed for $\Delta W_{\mathrm{in}} = -2\,\mathrm{MeV}$ and $\Delta\epsilon_{\mathrm{long}} = 18.5\,\%$ for $\Delta W_{\mathrm{in}} = +2\,\mathrm{MeV}$. Below $\Delta W_{\mathrm{in}} = \pm 1\,\mathrm{MeV}$ the additional emittance growth stays below $\Delta\epsilon_{\mathrm{long}} = 6\,\%$. For a changed input phase of $\Delta\phi_{\mathrm{in}} = \pm 5°$ the influence on the output beam energy is in the same range with $\Delta W_{\mathrm{neg}} = -3.8\,\mathrm{MeV}$ and $\Delta W_{\mathrm{pos}} = 3.4\,\mathrm{MeV}$ (see Figure 6.37 (b)).

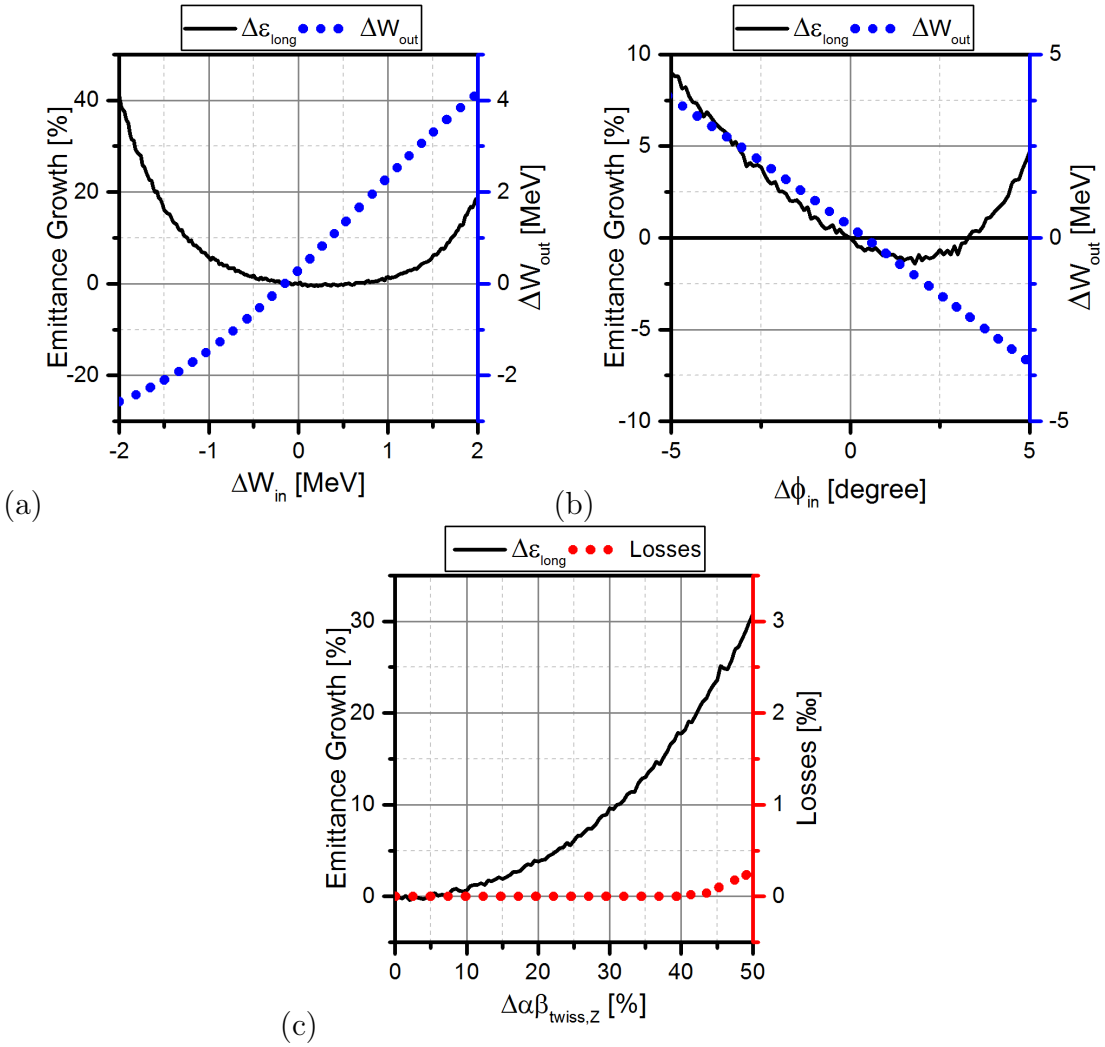

Figure 6.37: Results for longitudinal beam input errors. Energy offset (a) phase offset (b) and longitudinal mismatch (c).

Here the influence on additional longitudinal emittance growth is smaller and stays below $\Delta\epsilon_{\text{long}} = 9\,\%$ for the whole investigated parameter range. A longitudinal mismatching of the input beam ellipse was also investigated by changing the Twiss parameters α_{twiss} and β_{twiss} by up to $\Delta\alpha\beta_{\text{twiss}} = +50\,\%$ (see Figure 6.37 (c)). This results in rising emittance growth of up to $\Delta\epsilon_{\text{long}} = 30.8\,\%$ for a 50 % mismatch. Minimal losses occur beyond $\Delta\alpha\beta_{\text{twiss}} = +40\,\%$ but only reach a maximum of $N_{\text{lost}}/N = 0.028\,\%$. For a mismatch of up to 22.5 % the additional emittance growth stays below $\Delta\epsilon_{\text{long}} = 5\,\%$ without any losses.

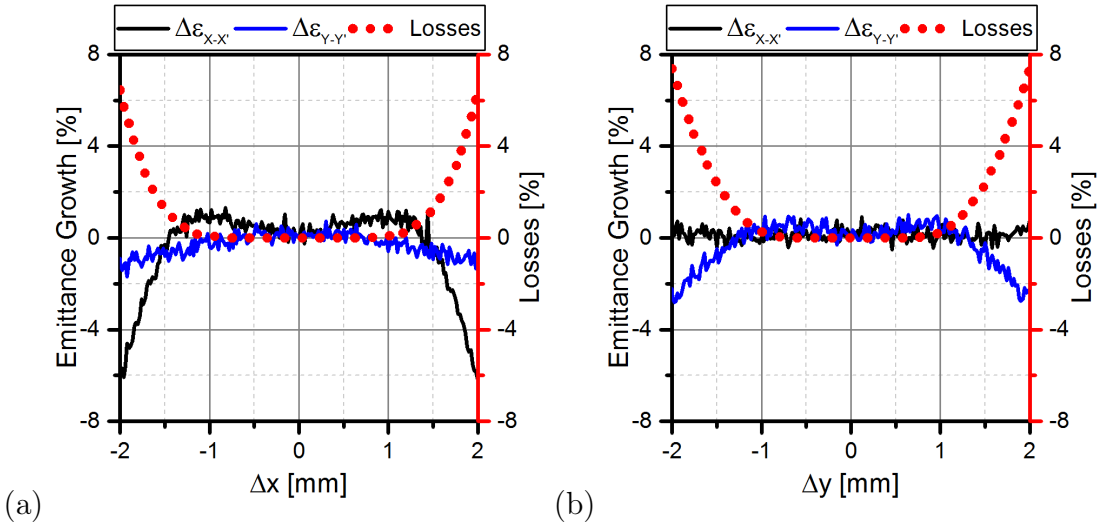

Figure 6.38: Emittance growth and losses for transverse beam input errors for horizontal displacement (a) and vertical displacement (b).

A transverse displacement of the beam in the horizontal and vertical direction, as well as the influence of a tilted input beam were investigated. Furthermore, a transverse mismatch in both planes was considered. The beam was displaced by up to $\Delta xy = \pm 2\,\mathrm{mm}$ in both planes independently (see Figure 6.38). For displacements $\Delta xy > 1\,\mathrm{mm}$ in both transverse directions, the results show significant losses in the linac. The decrease in emittance growth visible for large displacements in the plots is due to particle losses.

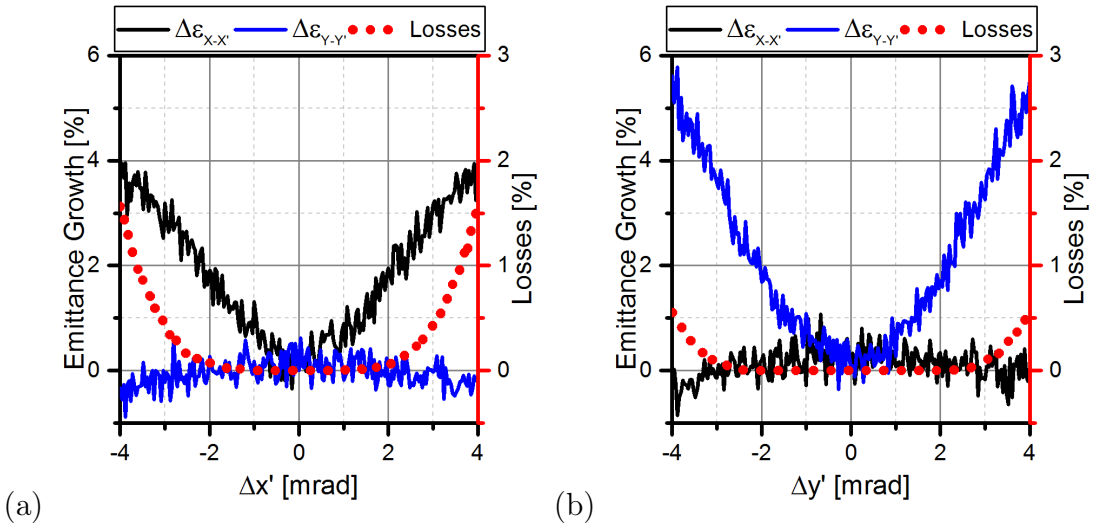

Figure 6.39: Emittance growth and losses for transverse beam input errors for horizontal deflection (a) and vertical deflection (b).

Tilting the input beam by $\Delta x'y' = \pm 4\,\mathrm{mrad}$ leads to slightly different results in the horizontal and vertical plane (see Figures 6.39). In the horizontal plane significant losses of up to $N_{\mathrm{lost}}/N = 1.5\,\%$ occur beyond $\Delta x' = \pm 2\,\mathrm{mrad}$. In the vertical plane losses occur beyond $\Delta y' = \pm 2.5\,\mathrm{mrad}$ but only reach $N_{\mathrm{lost}}/N = 0.5\,\%$. As a result, the additional emittance growth here is also a little higher than in the horizontal plane. Figure 6.40 shows a mismatch of the input beam of up to $\Delta\alpha\beta_{\mathrm{twiss}} = +50\,\%$ in the transverse planes. In the horizontal plane significant losses occur for $\Delta\alpha\beta_{\mathrm{twiss}} \geq 20\,\%$ and reach a maximum of $N_{\mathrm{lost}}/N = 2.3\,\%$. However, no losses are observed in the vertical plane and even a reduction of emittance growth with a minimum of $\Delta\epsilon_y = -2\,\%$ is found for $\Delta\alpha\beta_{\mathrm{twiss}} = 20 - 30\,\%$.

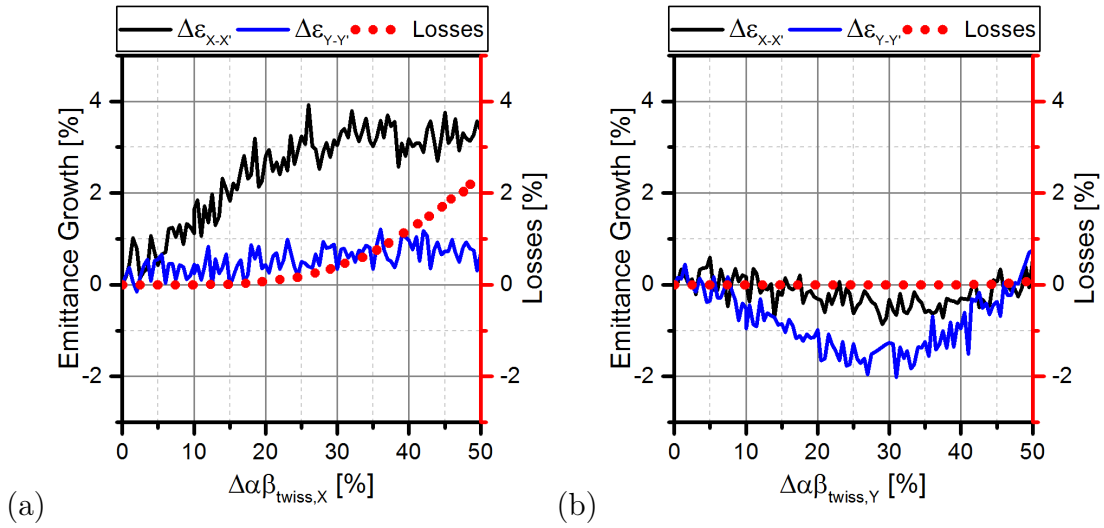

Figure 6.40: Emittance growth and losses for transverse beam input errors for horizontal mismatch (a) and vertical mismatch (b).

The investigation of the injected beam parameters shows good flexibility of the design while also showing some hard limits, that should not be exceeded. However, these limits might be mitigated by correction schemes for the transverse and longitudinal beam handling in case of static errors.

6.3.6 Simulations with Error Ensembles

In the previous Chapters 6.3.3 and 6.3.4, the individual influence of different error types was investigated and a set of "Safe values" for manufacturing and alignment tolerances of the linac was derived from the performed error studies. In this chapter, these values will be put to a test by running error studies with a combination

of these values along with two additional scenarios. Beam injection errors are not considered in this approach. As expected, the individual contributions of losses, emittance growth etc. cannot simply be added to gain the final result of a linac with combined errors. The reason being that for example the displacement of the magnetic lens triplet, the displacement of the magnetic lens singlets and the displacement of the cavities add up in the same direction and may therefore cause significantly higher losses than their individual contributions. To assure statistic soundness of the results, the simulations were performed with a higher number of particles. Therefore, the total number of calculated particles for each scenario is $N_{\text{total}} = 10^8$. All parameters for the three scenarios are shown in Table 6.8.

Table 6.8: Parameters for combined error runs.

	Run 1	**Run 2**	**Run 3**
Error Type	**Safe values**	**Adjusted triplet**	**Best case**
Quadrupole Lenses			
Singlet displacement (x/y)	80 µm	80 µm	50 µm
Singlet rotation $(\phi_X/\phi_Y/\phi_Z)$	1 mrad	1 mrad	1 mrad
Gradient error dB'/B'_0	0.7 %	0.7 %	0.1 %
Triplet displacement (x/y)	360 µm	100 µm	100 µm
Triplet rotation $(\phi_X/\phi_Y/\phi_Z)$	1.6 mrad	1 mrad	1 mrad
Cavities			
Cavity field $\Delta E/E_0$	0.7 %	0.7 %	0.1 %
Cavity phase $\Delta\phi$	1.4°	1.4°	0.1°
Gap voltage $\Delta E_{\text{gap}}/E_{\text{gap},0}$	2 %	2 %	1 %
Cavity displacement (x/y)	600 µm	600 µm	100 µm

A first set of parameters (Run 1) is called "Safe values" since it is a combination of the safe values defined in Chapter 6.3.3 and 6.3.4. The second run is called "Adjusted triplet" and includes the same error values as the first run except for the quadrupole triplet displacement and rotation which has been significantly reduced since the "Safe values" are much larger than the accuracy that can be achieved during alignment. Finally, the last set of values is called "Best case" with all errors reduced to the values that can typically be achieved during manufacturing and

alignment of linear accelerators [23, 32, 48]. In Figure 6.41, the average transmission for the three cases is shown. The red line indicating the "Safe values" run shows, as expected, the lowest transmission of the three with just 92.79 % average over a thousand runs. A much better result is seen for the "Adjusted triplet" setting (black line) with an average transmission of 98.47 %. This is already an acceptable value for error studies without steering correction. Finally, the "Best case" transmission shown by the green line illustrates how the linac would benefit from reducing all tolerances to their possible minimum. Here, the average transmission is 99.76 %. In Figures 6.42, 6.43 and 6.44 the distributions of simulation runs with respect to their transmissions are shown. In Figure 6.42, the distribution for the "Safe values" shows a very wide spread of transmissions with some runs even going as low as 70 %. The situation is already significantly improved in the "Adjusted triplet" scenario (see Figure 6.43) where transmissions below 95 % are already very rare. In Figure 6.44, the superiority of the "Best case" scenario is evident, since about 70 % of the runs show full transmission and transmissions below 99 % are rare.

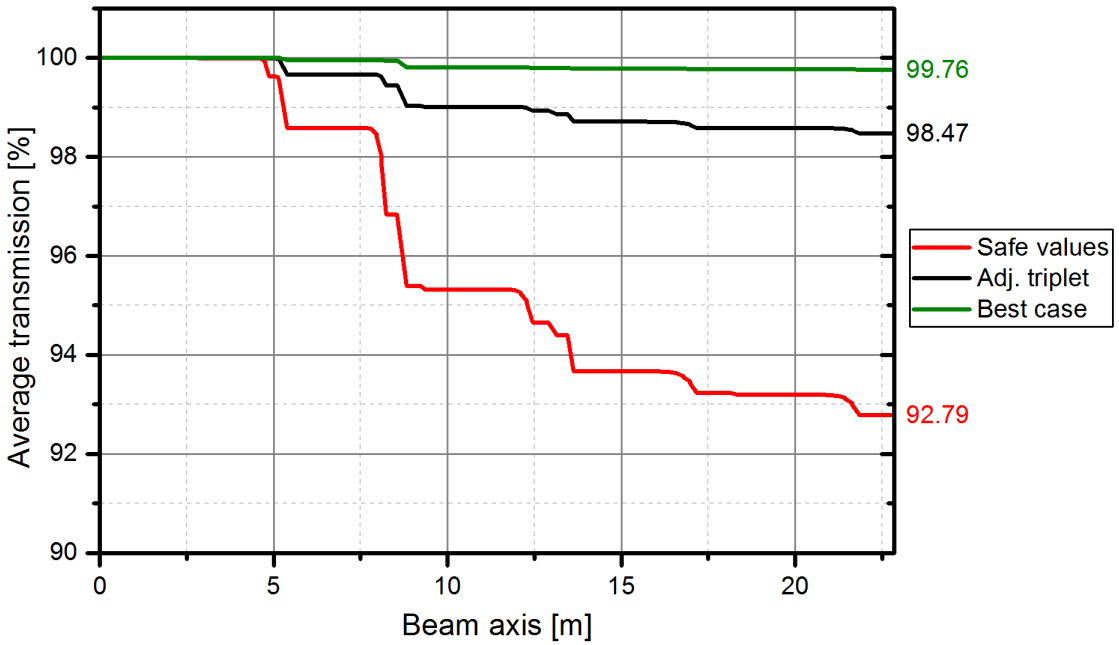

Figure 6.41: Average transmission for all three cases with combined errors.

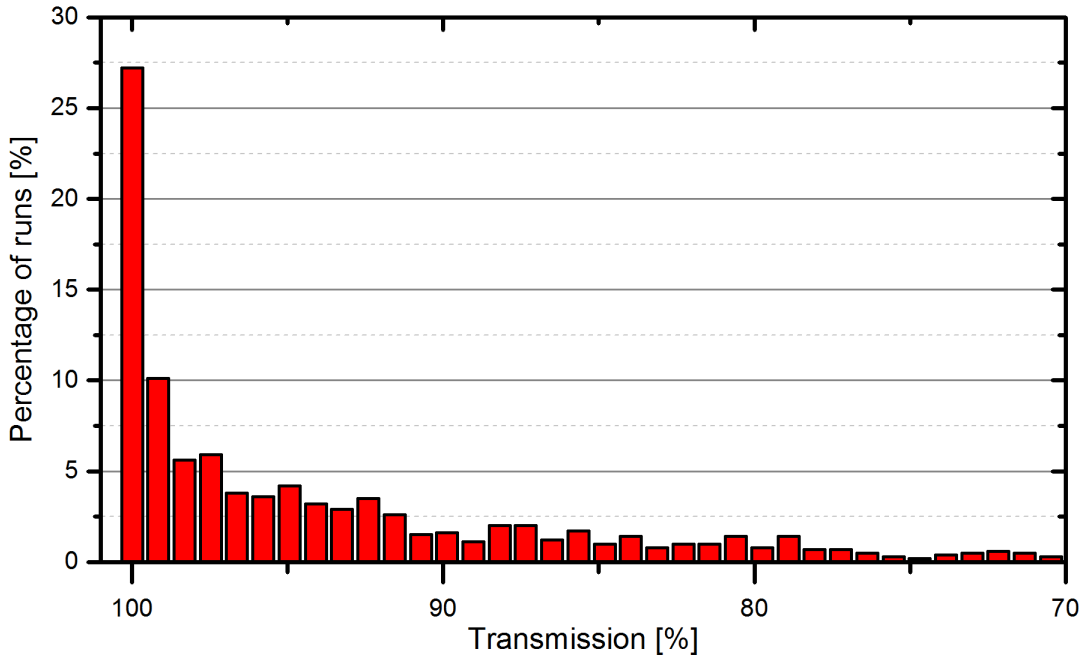

Figure 6.42: Distribution of particle transmissions for 1000 runs with random errors for the “Safe values” scenario.

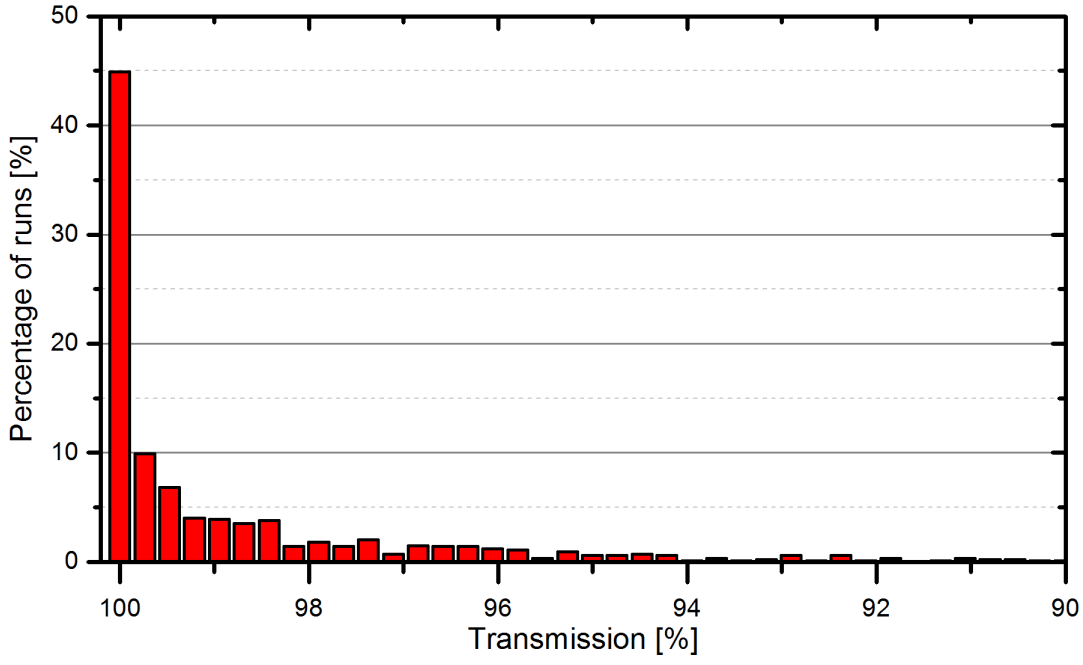

0

Figure 6.43: Distribution of particle transmissions for 1000 runs with random errors for the “Adjusted triplet” scenario.

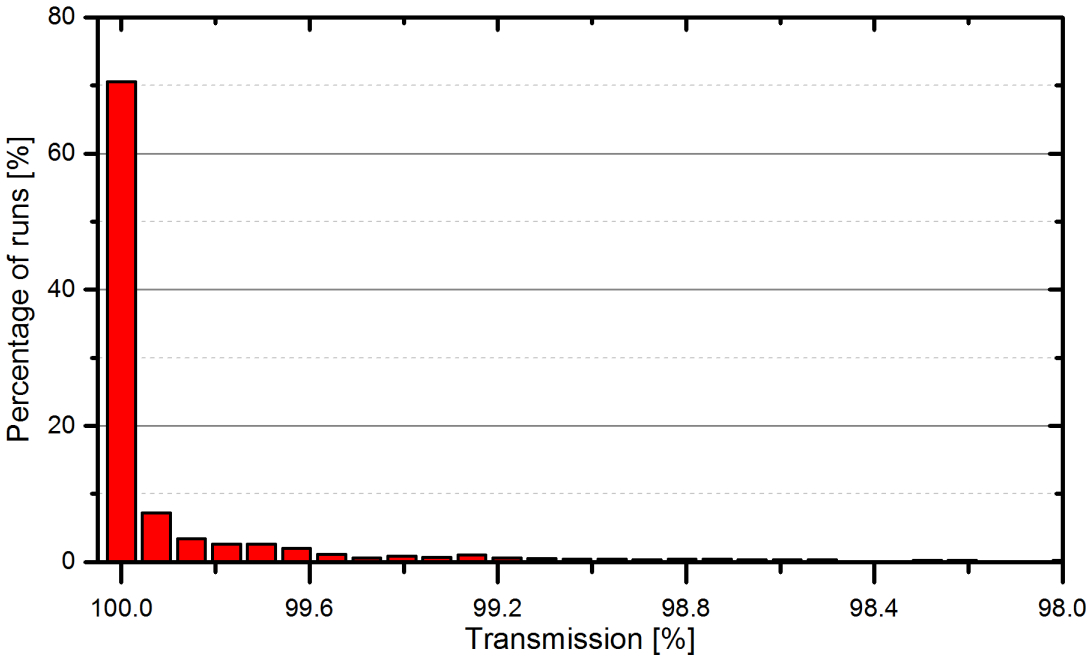

Figure 6.44: Distribution of particle transmissions for 1000 runs with random errors for the "Best case" scenario.

In summary, the investigation of combined errors shows clearly, that the single contributions add up to much larger losses than the sum of their individual contributions. The "Safe values" case would not be considered reasonable for an actual linac to be built, but the two more strict tolerance settings provide reasonable performance within a parameter range that can be achieved by manufacturers and during alignment and operation. A significant improvement of error tolerances, concerning the transverse focusing, is achieved with steering corrections, as presented in the next chapter.

6.3.7 Steering Strategies

In this chapter, different steering strategies for correction of the transverse beam motion will be discussed. Displacement and tilting of the beam along the linac due to bad injection parameters or errors in the linac can be compensated to a certain degree by including xy-steering magnets into the design. To find the right number of steerers and their positions, error studies with $N_{\text{total}} = 10^8$, including steering corrections using different steering strategies were performed. The corrective steering is applied for each single run of the error study by finding the correct steerer settings using the envelope calculation mode of TraceWin[7]. Each steerer is paired with a beam position monitor (BPM). The strategy used in these calculations is to set the steerers to center the beam at the position of their corresponding BPM (as illustrated in Figure 6.45 (a)). Using two consecutive steerers between triplet lenses, the beam can be put back on the beam axis by the first steerer and with the second steerer the beam is then set parallel to the beam axis (see Figure 6.45 (b)).

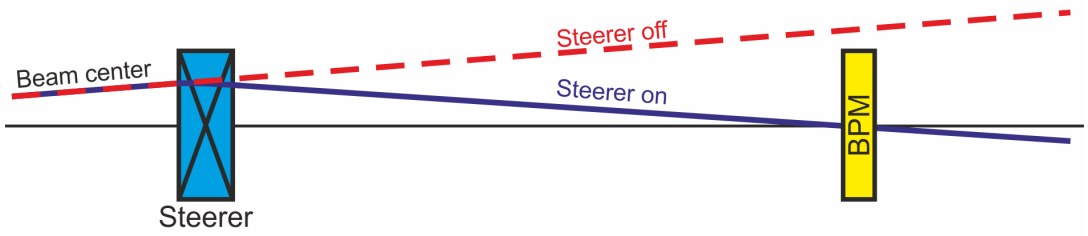

(a)

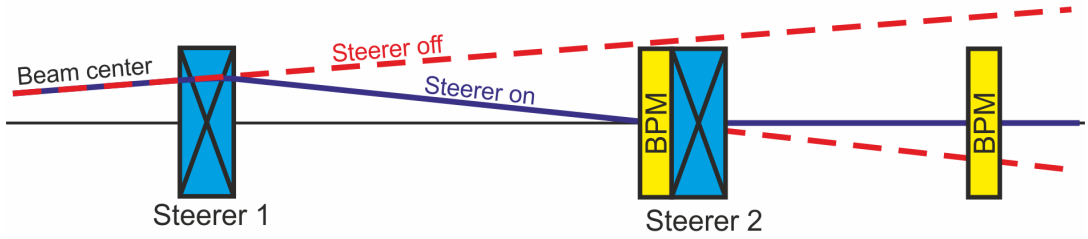

(b)

Figure 6.45: Working principle of the steering strategy used in the simulations for one steerer (a) and two consecutive steerers (b).

[7]In this case, no multi-particle simulations performed. The beam dynamics are calculated using only the beam envelopes. This saves a lot of computation time and is accurate enough to find solutions for steering corrections.

The first investigation is aimed at measuring the effectiveness of different steerer configurations to suppress component errors within the linac. Errors of the injected beam will also be considered later on. To benchmark the different steerer configurations, the simulations were performed with the "Safe values" error set (see Table 6.8) since this caused the highest losses and will therefore be the hardest to compensate. In Figure 6.46, the three steerer combinations that were investigated are shown. The first configuration features a steerer pair between the triplet lenses L4 and L5. In Addition to that, an additional steerer is positioned in front of lens L2 for the second configuration, where the corresponding BPM is positioned in front of L3. In the third configuration two steerer pairs are formed with steerers positioned at L2+L3 and L4+L5. The average transmissions of the different steerer configurations are shown in Figure 6.47.

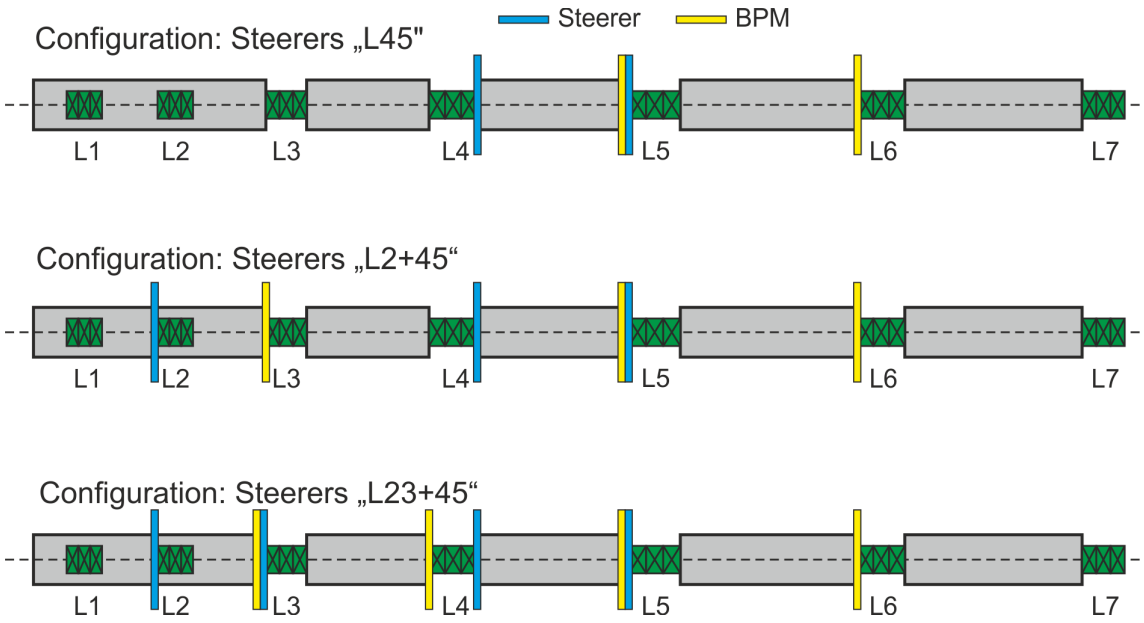

Figure 6.46: Steerer and BPM positions for the different steerer configurations.

Without steerers, the average transmission of the linac is 92.79 %. The results of the steering study show, that the last three sections can be safely operated with Steerers positioned only in the middle of the linac (blue line in Figure 6.47). Therefore no additional steerers in the second half of the linac are necessary. However, the overall average transmission for the "Steerers L45" case is still only 95.72 %. Accordingly, the first two cavities are more critical with respect to beam losses than the others. The placement of a steerer within the second internal lens of the first cavity can significantly reduce losses at the aperture of L3, while significant losses persist

in the following lens L4, leading to an average transmission of 98.30 %. Adding another steerer at L3, finally reduces the overall losses to 0.03 % and therefore a reasonable average transmission of 99.97 % even for the relatively loose tolerances defined by the "Safe values" setting. A transverse emittance growth distribution for the optimal case is shown in Figure 6.48. The additional emittance growth RMS value is $\Delta\epsilon_{\text{x-x',rms}} = 3.41\,\%$ and $\Delta\epsilon_{\text{y-y',rms}} = 3.49\,\%$ for this case. As shown in Figure 6.49, the average beam power lost in the cavity walls due to particle losses stays below 0.35 W for a duty cycle of 0.1 % (10 Hz, 100 µs pulse) in this case. Running the "Best case" scenario with this steerer combination results in average losses of only $1 \cdot 10^{-7}$. Therefore the safest layout will be the two steerer pairs at L2+L3 and L4+L5, which can even tolerate relatively large alignment errors without a big impact on performance.

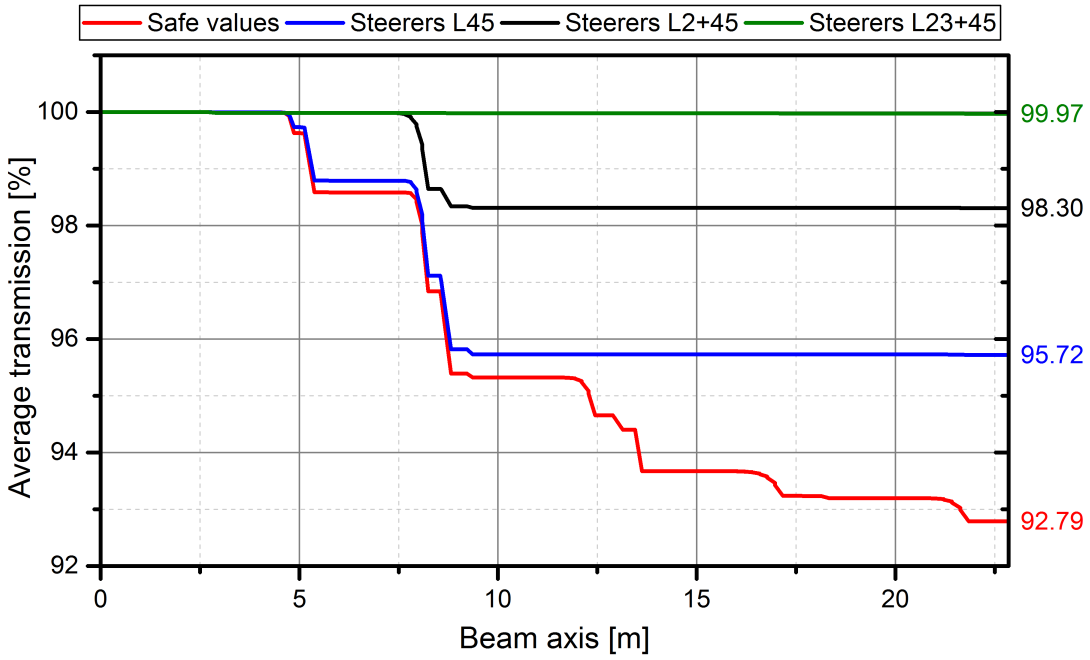

Figure 6.47: Average transmission for error studies using the "Safe values" setting and applying different steering strategies.

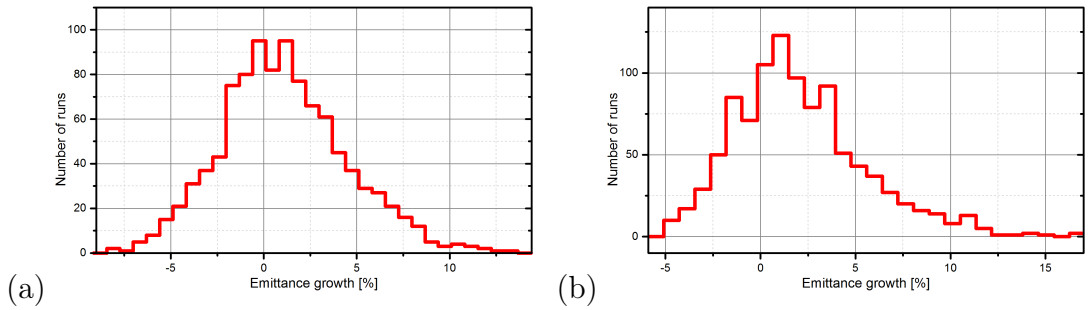

(a) (b)

Figure 6.48: Distribution of additional transverse emittance growth (a) in $x - x'$ (b) in $y - y'$ for the "Steerers L23+45" configuration and the "Safe Values" error setting.

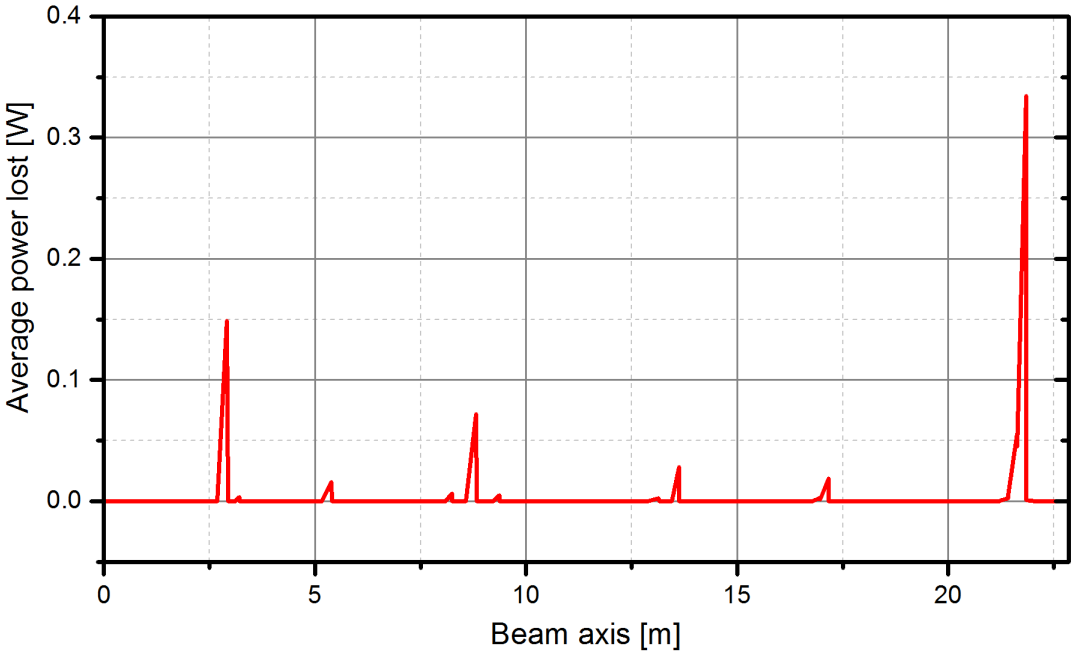

Figure 6.49: Residual power lost for the "Steerers L23+45" configuration with high error values from the "Safe values" setting for a duty factor of 0.1 %.

As a last step, additional errors at the injection are considered. A displacement of up to $\Delta xy = \pm 200\,\mu\text{m}$ and an angle offset of $\Delta x'y' = \pm 2\,\text{mrad}$ were set additional to the errors for the "Safe values" setting. Simulations were performed with and without the "L23+45" steerer configuration. Without steerers this new scenario results in significant average losses of 7.39 %. With the proposed steerer setup these losses can be reduced to 0.05 % (see Figure 6.50).

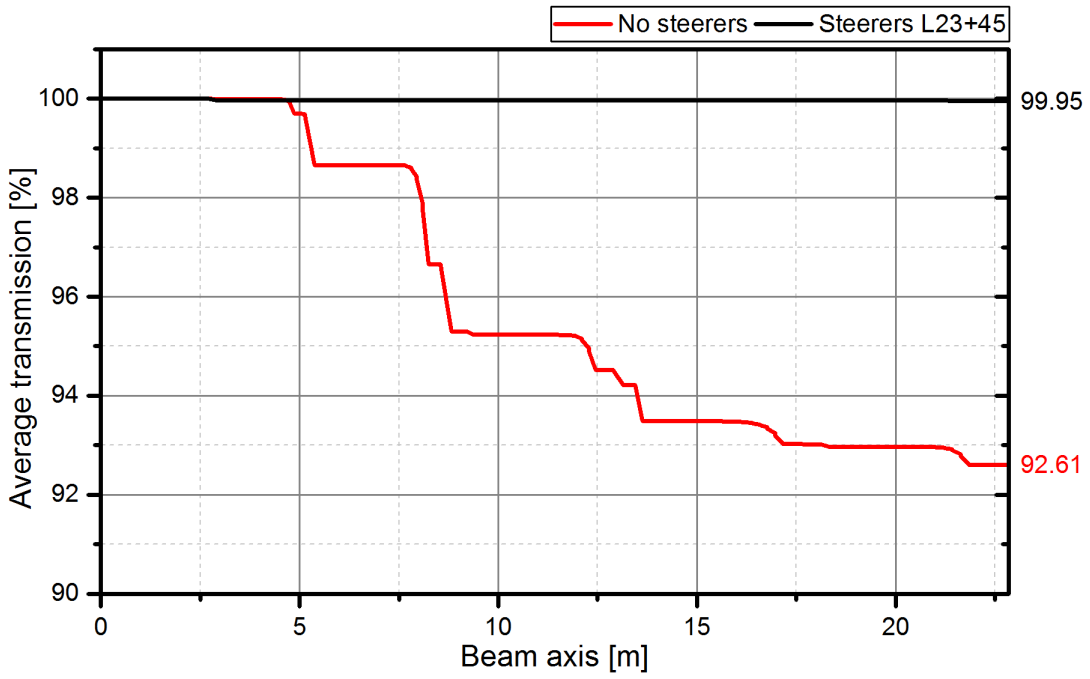

Figure 6.50: Average transmission for error studies using the "Safe value" setting with additional source errors of $\Delta xy = \pm 200\,\mu\text{m}$ and $\Delta x'y' = \pm 2\,\text{mrad}$ with and without the preferred steerer setup.

In summary, the design shows to be performing well for the two error settings "Adjusted Triplet" and "Best case" even without steerers. The "Safe values" setting, that was deduced from the single error contributions in section 6.3.2, shows to be too extreme for the linac without correcting steerers, resulting in average losses of over 7 %. This however, can be reduced with two steerer pairs located at Lenses L2+L3 and L4+L5, to an average particle loss of just 0.03 %. Additional source errors at the injection ($\Delta xy = \pm 200\,\mu\text{m}$ and $\Delta x'y' = \pm 2\,\text{mrad}$) have minimal effect in this scenario with steerers and average losses are only 0.05 %. This shows, that with a sufficient steering strategy even large errors in manufacturing or alignment can be compensated for the linac developed in this work. Therefore, if state of the art manufacturing and alignment tolerances are used in addition with the two steerer pairs steering strategy, stable and reliable operation of the linac is ensured as simulations confirm.

7 3D RF Simulations of Cavities

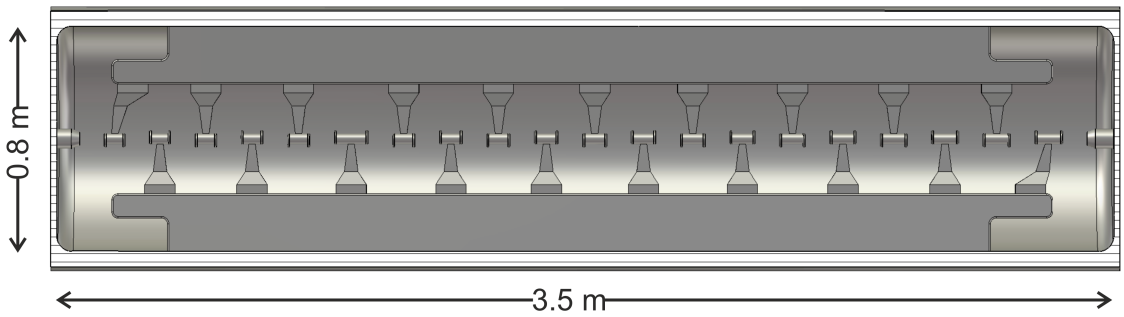

Figure 7.1: Cross section (xz-plane) of an IH-type cavity.

All five RF-cavities for the proposed linac layout from section 6.1 were designed as 3D models using CST Microwave Studio[1]. IH-type cavities were used for this linac (see Chapter 2.1). The benefits of these structures are the period length of $\beta\lambda/2$ and their high shunt impedance. Due to the $H_{11(0)}$ mode used in these cavities, they are also much smaller in diameter than a conventional Alvarez structure at the same operating frequency (about a factor of $0.4 - 0.5$). The general parameters of the cavities are summarized in Table 7.1. At an operating frequency of 108.408 MHz, the cavities have an inner diameter from 69 cm to 81 cm. In the following, the different design choices for the cavities are explained and the 3D RF simulation results including power requirements are presented.

Operating frequency	108.408 MHz
Cavity diameter	$69 - 81$ cm
Cavity length	$2.8 - 4.9$ m
Number of gaps	$19 - 39$

Table 7.1: Design parameters of the five IH-type cavities.

[1] https://www.cst.com/products/cstmws

7.1 Design of IH-Type Cavities

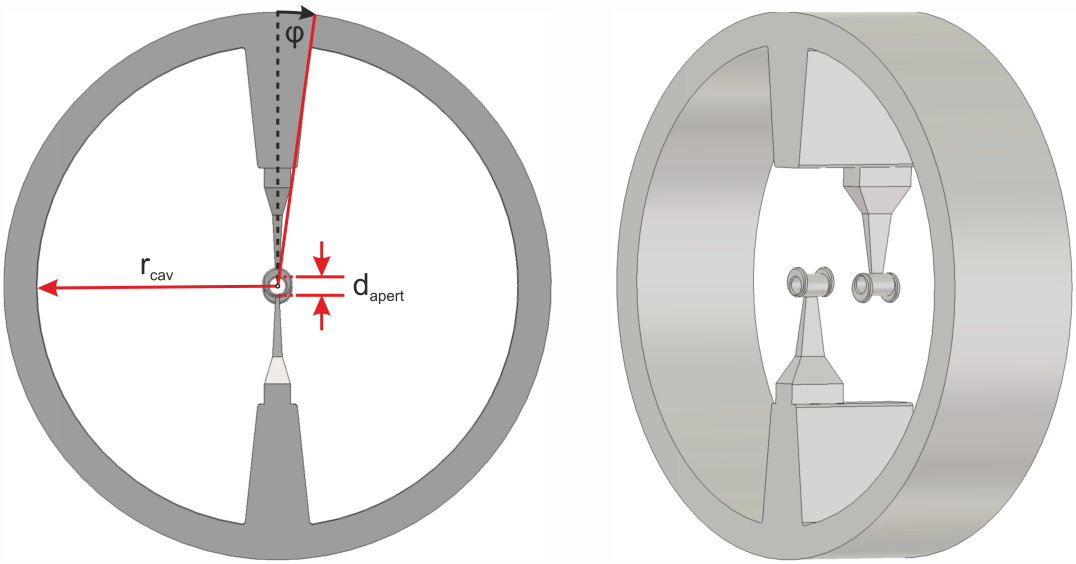

Figure 7.2: Cross section (xy-plane) of an IH-type cavity.

In Figures 7.1 and 7.2, the basic structure of an IH-type cavity is shown. In the cavity, the drift tubes are positioned by stems, that sit on two opposing girders. The drift tubes are connected alternately to the top and bottom girder to generate the accelerating fields between the tubes. This is caused by the opposing potentials of the neighboring drift tubes. A cavity cross section in Figure 7.2 shows the slim design of stems and drift tubes with their widths limited by a common angle ϕ. While the angle ϕ in theory has no influence on the resonance frequency, a smaller angle results in a higher shunt impedance [18]. Therefore, ϕ should be chosen as small as possible taking into consideration the mechanical stability of the stems and girder unit. The design of the IH-type cavities features girder undercuts, tilted stems and bulges for dipole field correction (see Figure 7.3). To enhance the magnetic flux at the ends of the cavity, the girders are cut out below the stems. These girder undercuts provide additional area for the magnetic field, resulting also in higher on axis E_Z-fields at the cavity ends. The undercuts are defined by the undercut length L_{uc} and the undercut height h_{uc}. Tilted stems allow the girders to be shorter and therefore also provide additional cross sectional area for the magnetic field. With the correct proportions, a flat voltage distribution can be achieved over the whole cavity.

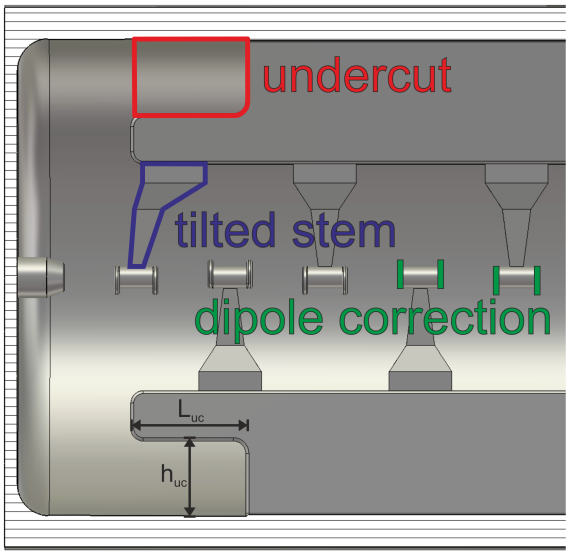

Figure 7.3: Design features of an IH-type cavity.

Typically the first and last gap voltages are $50 - 60\,\%$ of the maximum while all other gap voltages are almost identical at the maximum level. This mode is then called the $H_{11(0)}$-mode of the IH-cavity. The difference in voltage distribution between a cavity with and without girders is shown in Figure 7.4. Since the effective shunt impedance for both versions is very similar, the use of girders has no drawback and should be preferred for IH-type designs. A flat field distribution allows higher average accelerating gradients and is also preferred for stable beam dynamics.

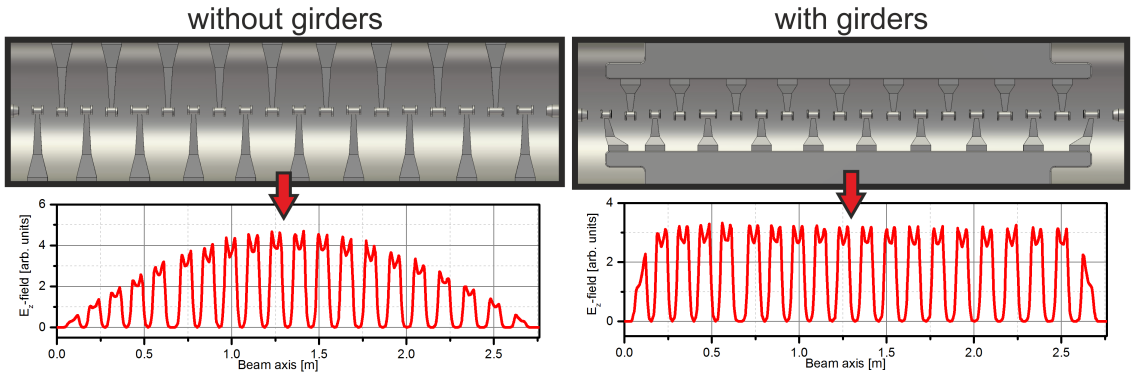

Figure 7.4: IH-type cavity without/with girders (left/right) and the corresponding onaxis E_Z-field.

7.1.1 Electromagnetic Fields

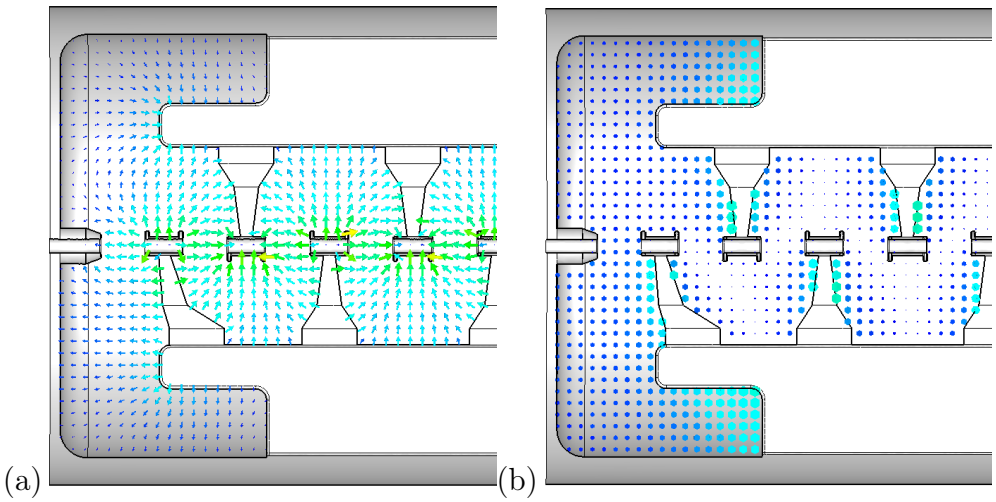

Figure 7.5: Electric and magnetic fields in the cross section plane at the beginning of an IH-type cavity. Electric field (a) and magnetic field (b).

In Figures 7.5 and 7.6, the distribution of the electric and magnetic fields in the accelerating mode of an IH-type linac cavity are shown. The electric field is concentrated between the girders and especially between the drift tubes. In the space between the drift tubes the electric field is almost entirely orientated in the direction of the beam axis ($E_z \gg E_x + E_y$).

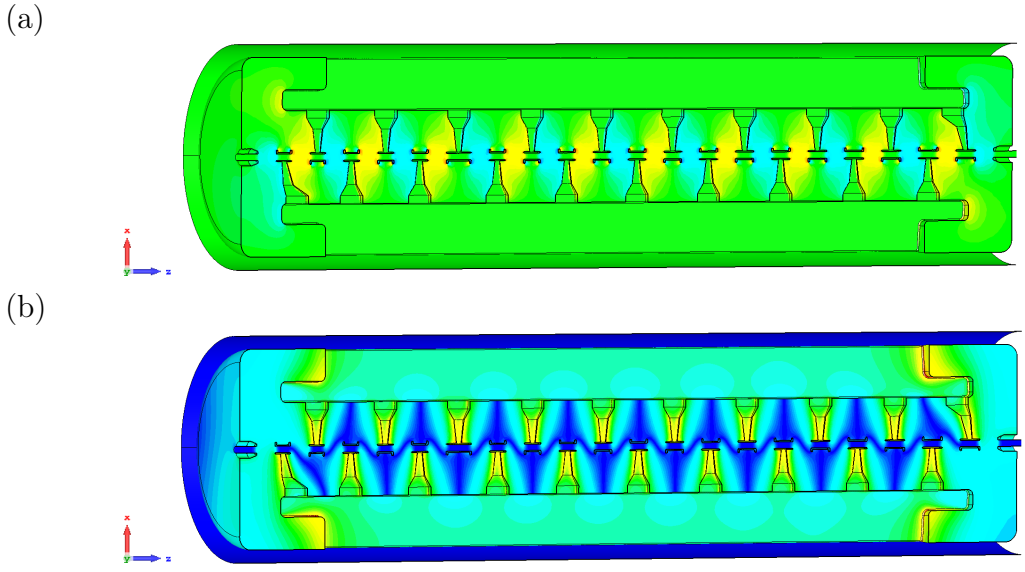

Figure 7.6: Contour plots of the E_z-field (a) and the absolute magnetic field (b) on the cross section of a whole IH-type cavity.

Remaining dipole components appear in the direction of the girders due to the opposing stem geometry. These dipole components can be compensated by bulges on the drift tubes (see following Chapter 7.1.2). Due to the $\beta\lambda/2$ structure of IH-type cavities, the electric field in two neighboring gaps is shifted by $\Delta\phi = 180°$. This polarity change is illustrated in Figure 7.6 (a) by the plotted projection of the E_z-field on the cross section of the cavity. The magnetic field concentrates around the stems, as can be seen in Figure 7.6 (b), where the projection of the absolute magnetic field on the cross section plane is shown. Here the huge impact of the girder undercuts can be seen, since the magnetic field is very high in the undercut areas.

7.1.2 Dipole Correction for IH-Type Cavities

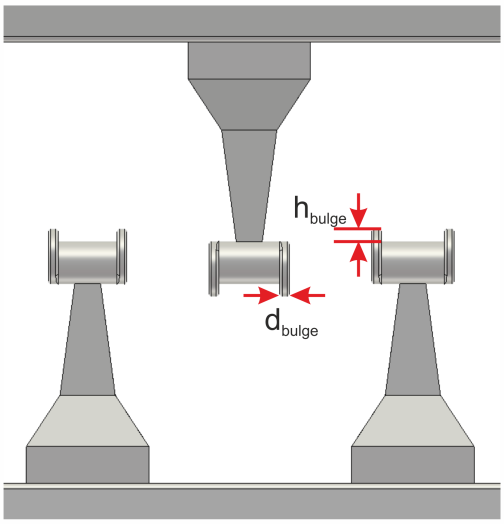

Figure 7.7: Dimensions of the bulges for dipole correction.

Due to its geometry with opposing stems on opposite potential, the electric field on the beam axis of an IH-type cavity always has a dipole component. This dipole component E_x can be as large as 10 % of E_z. Since the dipole field will deflect the beam in the x-direction, it should be minimized to get best beam transport. For cavities with flat field distribution, the effect is self compensating since the dipole component E_x changes its sign in each gap. Still the dipole field should be minimized to prevent large beam oscillations in the x-plane. To compensate the unwanted dipole field E_x in the gaps, bulges can be added to the drift tubes [18].

These bulges are positioned at both ends of each drift tube and are characterized by their thickness d_{bulge} and their height h_{bulge} (see Figure 7.7). The effect of the dipole correction is shown in Figure 7.8 where the electric field for two gaps is shown for a geometry without bulges and with bulges, respectively. A dipole component is obvious from the large angle of the field vectors between the gaps in Figure 7.8 (a). In Figure 7.8 (b) the dipole component is almost completely compensated in the whole area between the drift tubes.

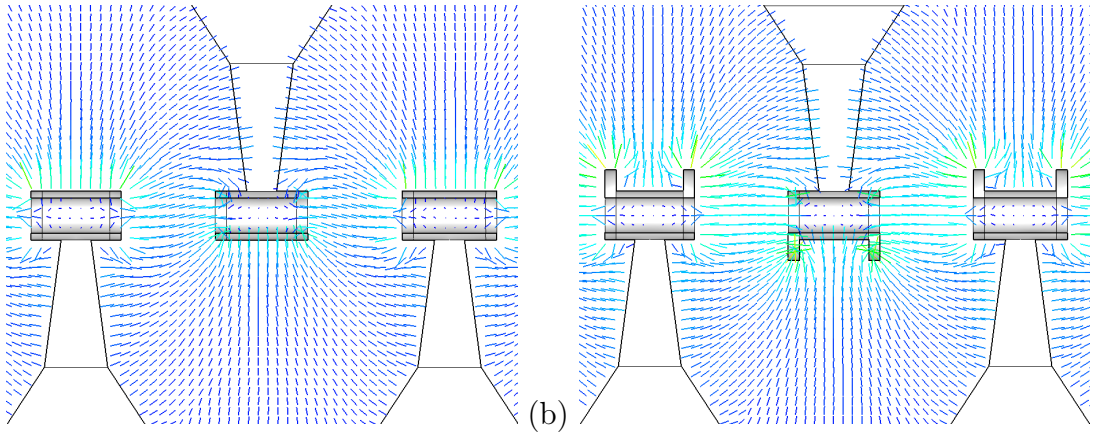

(a) (b)

Figure 7.8: Electric field vectors for a geometry without bulges (a) and with bulges (b) ($d_{bulge} = 8\,\text{mm}$, $h_{bulge} = 15\,\text{mm}$).

However, the addition of bulges to the drift tubes leads to a decrease in shunt impedance of the cavity and thus lower RF efficiency. Therefore, a trade off between the cavity power requirements and the amount of dipole correction has to be made. If the bulge height is $h_{\text{bulge}} \approx r_{\text{tube}}$ then the decrease in shunt impedance is typically in the order of $\frac{Z_{\text{eff},0} - Z_{\text{eff,dipc}}}{Z_{\text{deff},0}} > 10\,\%$. In Figure 7.9, the dependence of the dipole correction on the bulge height for a model of cavity two is shown.

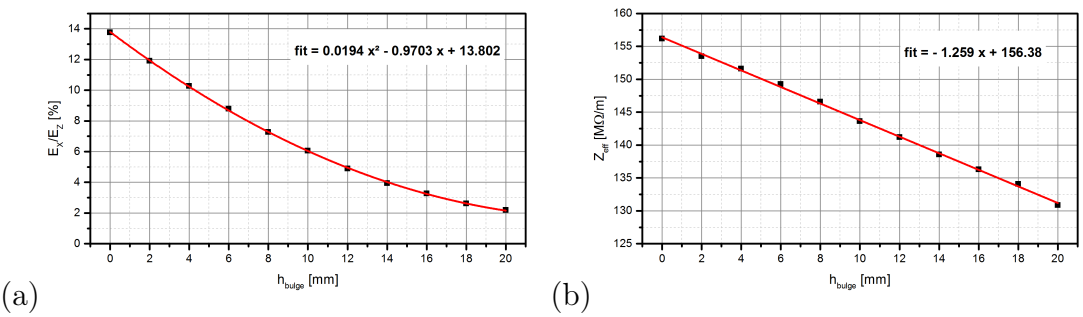

(a) (b)

Figure 7.9: Dipole ratio (a) and Effective shunt impedance (b) for different h_{bulge}.

The dipole ratio $\frac{E_x}{E_z}$ shows a strong dependency on the bulge height that can be fitted with a second order polynomial. However, the effective shunt impedance decreases linearly with increasing bulge height. While the dipole ratio is $\frac{E_x}{E_z} = 13.76\,\%$ without bulges, it can be reduced to less than half that value ($\frac{E_x}{E_z} = 6.05\,\%$) with a bulge height of $h_{\text{bulge}} = 10\,\text{mm}$. In that case, the resulting shunt impedance is $Z_{\text{eff},10\,\text{mm}} = 143.62\,\frac{\text{M}\Omega}{\text{m}}$, which is 8 % lower than the original value of $Z_{\text{eff},0\,\text{mm}} = 156.18\,\frac{\text{M}\Omega}{\text{m}}$.

7.2 First Cavity with Two Internal Lenses

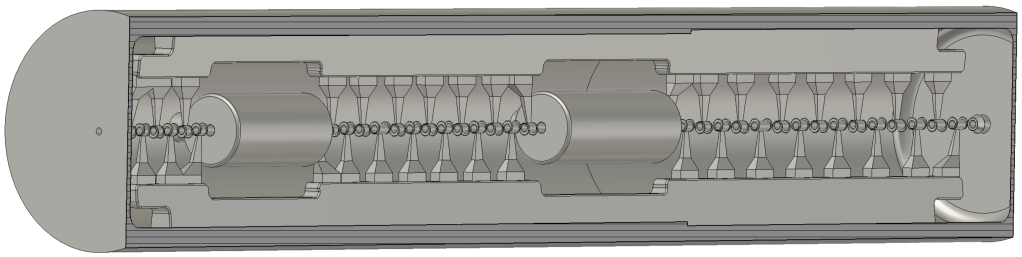

Figure 7.10: Cross section of the first cavity with two internal lenses.

The first cavity of the proposed poststripper linac from section 6.1 consists of three sections with two internal lenses in between. To provide stable beam dynamics at the lower velocity range from $\beta = 0.055$ to $\beta = 0.087$, the division into several short sections is necessary. For the first three sections an integrated lens design was chosen to make use of the available RF-power and to keep the drift lengths before and after lenses as short as possible (see Figure 7.10). To get the desired voltage distribution in the three sections of $V_{1-1} = 1.98\,\mathrm{MV}$, $V_{1-2} = 6.85\,\mathrm{MV}$ and $V_{1-3} = 10.79\,\mathrm{MV}$ the cavity was divided into two zones as shown in Figure 7.11. The undercut lengths at the cavity ends, as well as the cavities inner radius in the two zones were varied independently to get the correct voltage ratio of $\frac{V_{1-3}}{V_{1-1}+V_{1-2}} = 1.22$. This optimization showed, that the radius of the second zone r_2 has to be 12.5 mm larger than the first zone radius of $r_1 = 348\,\mathrm{mm}$. By changing the length of the undercut at the front of the cavity, the voltage ratio of the first two sections was then tuned to $\frac{V_{1-2}}{V_{1-1}} = 3.46$. The resulting field distribution satisfies the voltage ratios dictated by the beam dynamics design. For the H_{113}-mode of this cavity, the field and voltage distribution is shown in Figure 7.12. An $H_{11(0)}$-mode would also be an option for this cavity. For reasons of improved mechanical stability the lenses could also be attached to the girders instead of the cavity wall.

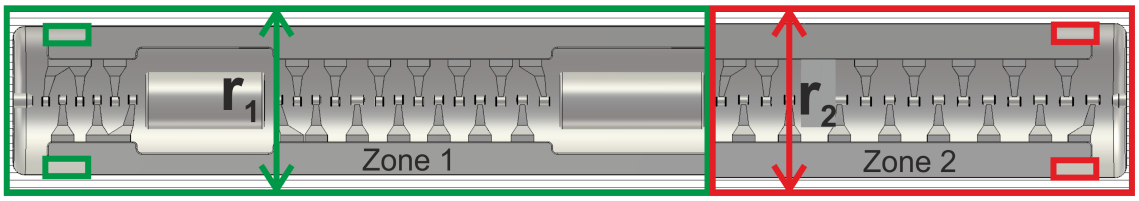

Figure 7.11: Distribution of the two zones for the first cavity. The undercuts are marked by the small rectangles in green (front) and red (end).

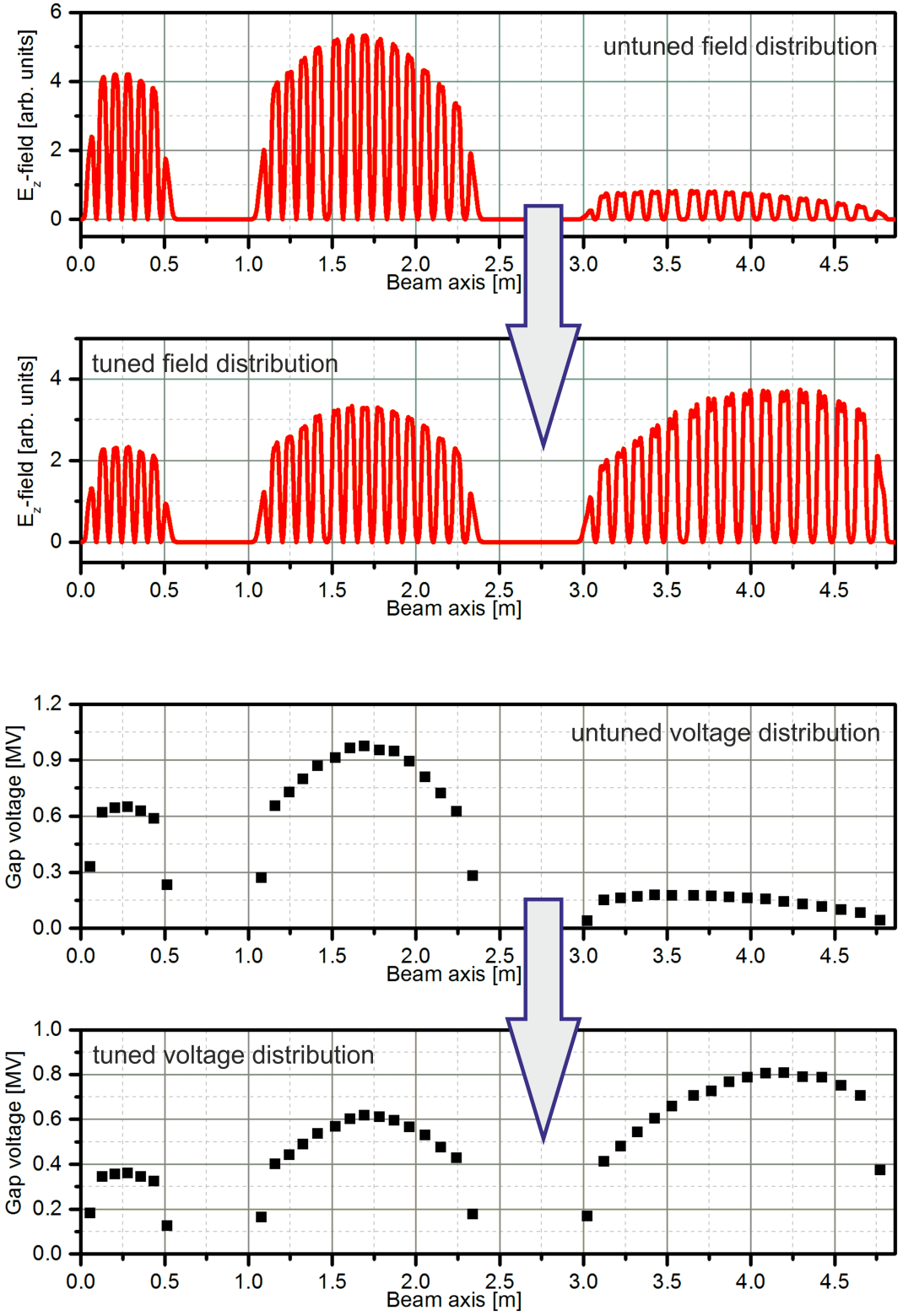

Figure 7.12: Field and voltage distribution for the first cavity before and after tuning.

The cavity power loss is calculated using a copper conductivity of $5.8 \cdot 10^7 \frac{\mathrm{S}}{\mathrm{m}}$ for the cavity in CST. Then the resulting value $P_{\mathrm{loss}}^{\mathrm{CST}}$ is the power loss of the cavity for a total stored energy of $W_{\mathrm{total}}^{\mathrm{CST}} = 1\,\mathrm{J}$ in the simulated volume. To calculate the power loss of the cavity under operating conditions, the calculated value has to be scaled to the correct total energy by using the scaling factor

$$\alpha = \frac{V_{\mathrm{eff}}^{\mathrm{CST}}}{V_{\mathrm{eff}}^{\mathrm{Design}}} \tag{7.1}$$

where $V_{\mathrm{eff}}^{\mathrm{CST}}$ is the sum of effective gap voltages calculated by CST Microwave Studio and $V_{\mathrm{eff}}^{\mathrm{Design}}$ is the desired effective cavity voltage dictated by the beam dynamics design. Additionally the resulting value is again scaled by a factor of $\frac{1}{0.9}$ to account for experimental results showing that for copper plated IH-type cavities the calculated power loss is usually 90 % of the actual measured value in the finished cavity. Therefore the cavity power loss is calculated by

$$P_{\mathrm{loss}} = \alpha^2 \cdot \frac{P_{\mathrm{loss}}^{\mathrm{CST}}}{0.9}. \tag{7.2}$$

To get the total power requirement of the cavity, the power required to accelerate the beam has to be considered as well. It is given by

$$P_{\mathrm{beam}}[\mathrm{kW}] = I_{\mathrm{beam}}[\mathrm{mA}] \cdot \frac{\Delta W_{\mathrm{beam}}[\mathrm{MeV}]}{N_q \cdot e} \tag{7.3}$$

with ΔW_{beam} being the energy gain of the beam acquired in the cavity, I_{beam} the average macro pulse current and N_q the ionization state. The total power requirement of the cavity is the sum of the cavity power loss and the beam power $P_{\mathrm{total}} = P_{\mathrm{loss}} + P_{\mathrm{beam}}$. Using this power loss value, the effective shunt impedance Z_{eff} is calculated. For the first cavity of the poststripper IH-DTL the calculated total power requirement for a 15 mA beam is $P_{\mathrm{total}} = 792\,\mathrm{kW}$. Therefore, this value is actually much lower than the design limit of 1.35 MW of the RF amplifier system at GSI UNILAC. This is mostly a result of the optimization of the beam dynamics, that favors shorter sections at the beginning of the linac. The inclusion of the fourth section (cavity 2, see following Chapter 7.3) into cavity one would, however substantially exceed the power limit. For this first cavity, the effective shunt impedance of the cavity is $Z_{\mathrm{eff}} = 151.97\,\frac{\mathrm{M\Omega}}{\mathrm{m}}$. A summary of the calculated RF properties of the first cavity is given in Table 7.2.

Table 7.2: Simulated RF properties of the first cavity.

Eigenmode frequency f_1	108.386 MHz
Inner radius r_1	34.8 cm
Inner radius r_2	36.04 cm
Inner length L_{cav}	4.86 m
Q-factor	$2.48 \cdot 10^4$
Power loss P_{loss}	521 kW
Beam power P_{beam}	271 kW
Cavity power requirement P_{total}	792 kW
Effective shunt impedance Z_{eff}	151.97 $\frac{\text{M}\Omega}{\text{m}}$

7.3 Cavities Without Internal Lenses

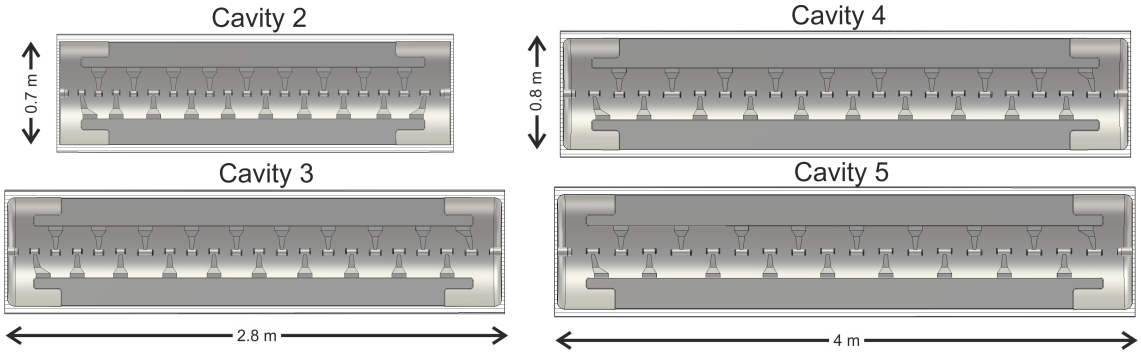

Figure 7.13: Cross sections of the remaining four cavities.

The remaining four cavities are all designed without internal lenses, since the transverse beam transport can be sufficiently managed with external triplets in the covered velocity range from $\beta = 0.087$ to $\beta = 0.155$. All four cavities are relatively similar. They differ in length and diameter, but share the same girder and stem geometry (see Figure 7.13). For each cavity, the resonance frequency was adjusted by changing the inner diameter of the cavities. The resulting inner diameters of the cavities range from $d_{\text{cav},2} = 73.54\,\text{cm}$ for cavity two to $d_{\text{cav},5} = 80.98\,\text{cm}$ for the last cavity (see also Table 7.3). Electric field flatness was adjusted by the length of the girder undercuts for each cavity individually. Since the thickness of the remaining part of the girder was kept constant, the height of the undercuts ranges from

$h_{\mathrm{uc},2} = 11\,\mathrm{cm}$ to $h_{\mathrm{uc},5} = 15\,\mathrm{cm}$. To get a flat field distribution, the undercut length at the end of the cavity has to be $3 - 5\,\%$ longer than that at the beginning of the cavity. Necessary undercut lengths are in the ranges of $L_{\mathrm{uc,initial}} = 19.5 - 20.2\,\mathrm{cm}$ and $L_{\mathrm{uc,final}} = 20.3 - 21\,\mathrm{cm}$. In Figure 7.14, the on axis E_z-field for the cavities is shown along with the corresponding gap voltages, that are scaled to the correct cavity sum voltage. The total power requirement of the four cavities ranges from $P_{\mathrm{total},2} = 981\,\mathrm{kW}$ to $P_{\mathrm{total},4} = 1101\,\mathrm{kW}$ with the other two cavities in between these values. So roughly speaking the cavities all are in the 1 MW power range leaving enough headroom, should the power requirement of the cavities be higher than expected.

Table 7.3: Simulated RF properties for cavities two to five.

	Cavity 2	Cavity 3	Cavity 4	Cavity 5
f_1	108.478 MHz	108.377 MHz	108.406 MHz	108.409 MHz
d_{cav}	73.54 cm	77.0 cm	79.34 cm	80.98 cm
L_{cav}	2.76 m	3.47 m	3.99 m	4.02 m
Q-factor	$2.44 \cdot 10^4$	$2.61 \cdot 10^4$	$2.72 \cdot 10^4$	$2.76 \cdot 10^4$
P_{loss}	741 kW	828 kW	837 kW	780 kW
P_{beam}	240 kW	262 kW	264 kW	240 kW
P_{total}	981 kW	1090 kW	1101 kW	1020 kW
Z_{eff}	$144.54\,\frac{\mathrm{M\Omega}}{\mathrm{m}}$	$121.54\,\frac{\mathrm{M\Omega}}{\mathrm{m}}$	$104.66\,\frac{\mathrm{M\Omega}}{\mathrm{m}}$	$90.35\,\frac{\mathrm{M\Omega}}{\mathrm{m}}$

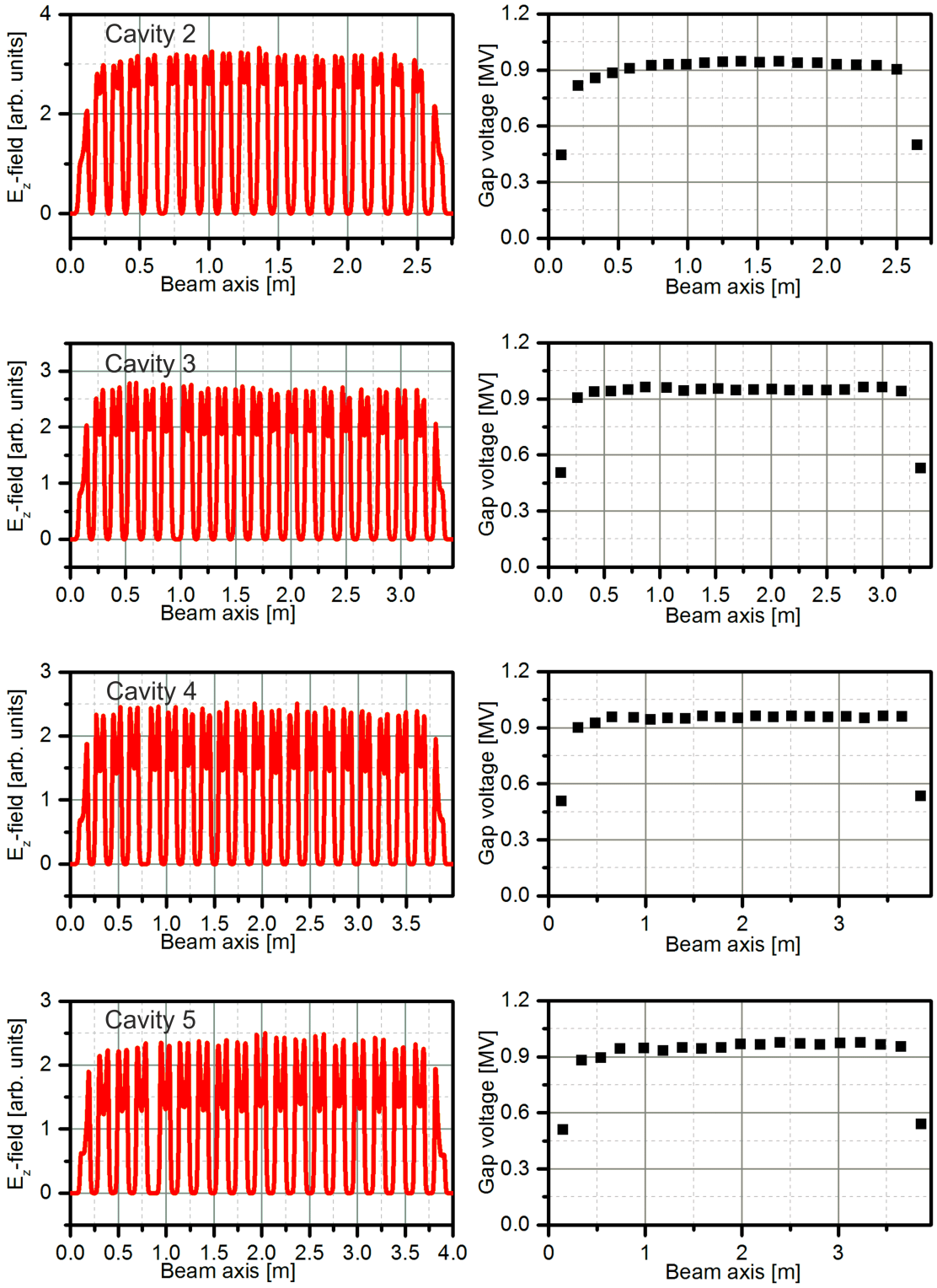

Figure 7.14: E_z-field distribution on the beam axis and resulting effective gap voltages for cavities two to five.

8 Summary and Outlook

The Universal Linear Accelerator UNILAC at GSI Darmstadt will serve as a dedicated ion injector for the new Facility for Antiproton and Ion Research FAIR. To deliver the required high particle intensities, the UNILAC has to be operated at 18 emA U^{4+} in the high current injector HSI and after stripping at 1.4 $\frac{\text{MeV}}{\text{u}}$, the poststripper linac has to accelerate a 15 emA U^{28+} beam to the SIS18 injection energy of 11.4 $\frac{\text{MeV}}{\text{u}}$. The main focus of this work was the development of efficient beam dynamics concepts to enable unprecedented high current operation at the GSI UNILAC.

As a first step, the performance of the existing matching section between the RFQ and the IH-type linac in the HSI was analyzed since significant losses were observed during operation. Simulations of the matching section and the following IH-DTL showed, that the matching section had become a bottleneck for high current operation due to the RFQ upgrade in 2009 [2]. High beam divergence behind the RFQ leads to losses in the order of 10 % for high current operation due to the small Superlens aperture. As a consequence of these worrying results, a completely new matching section was developed. The new matching section is based on two magnetic quadrupole triplet lenses with a 500 kV buncher in between [4]. This matching section was designed to provide optimal matching of the beam to the IH-DTL without losses. Due to the improved matching, even the losses in the IH-DTL were be eliminated. Overall, the new matching section provides more flexibility for operation of the HSI and significantly improves its high current operation capability. The magnet design and mechanical construction were developed in 2015/2016 t at GSI in cooperation with the author.

As a second step, a replacement option for the poststripper linac was developed. Replacing the existing poststripper Alvarez DTL is necessary for a number of reasons. Since the first two tanks of the Alvarez DTL were built in the 70s and tanks three and four in the 80s, age related issues occurred especially over the last decade. Failure rates of the quadrupole magnets due to water and/or vacuum leaks and

electrical shorts have increased significantly. In addition, the cooling channels inside the cavity walls and lens housings are corroded. Therefore, it is foreseeable that the existing poststripper linac will not be suited to provide reliable operation for FAIR. The high current capability of the existing Alvarez DTL is limited since its focusing lattice is based on DC quadrupole magnets that can not provide sufficient focusing for high current operation. As a consequence, a completely new poststripper linac concept was developed in this work. This new design makes use of the technological advances in accelerator technology. It is based on efficient IH-type cavities with magnetic triplet focusing and the KONUS beam dynamics concept. By the use of IH-Type cavities, the poststripper length was reduced from about 60 m to just 23 m while providing the same final energy. Power limits were chosen so that the proposed linac can be operated by the existing UNILAC RF amplifier structure [8, 42]. An optimization of the KONUS beam dynamics design was conducted to achieve low emittance growth at high beam current. For zero beam current, the matching requirements of KONUS sections were investigated systematically in this work. Low transverse emittance growth is achieved by transverse focusing based on an optimized constant phase advance scheme along the linac. The design and optimization of the beam dynamics were performed with the IAP Frankfurt in-house code LORASR. Additional cross-check calculations were performed with the widely used TraceWin code to confirm the beam dynamics design. To judge stability of the beam dynamics concept, extensive error studies were performed using TraceWin. These take into account alignment errors of the lenses, cavities and drift tubes, as well as field and phase errors of the RF signal. In addition, different beam steering strategies were investigated. In conclusion, the beam dynamics concept presented in this work provides optimal performance well within error limits achievable by current technology. Based on this beam dynamics layout, the five IH-type RF cavities were designed and simulated with CST Microwave Studio. Optimizations of the cavities were performed to achieve field flatness and a reduction of dipole fields in the accelerating gaps. Finally, the power requirements and RF properties of all cavities were calculated.

The beam dynamics and cavity designs that were developed in this work can be used for the improvement of the GSI UNILAC facility. A new MEBT section was developed, that provides an option to significantly improve the HSI performance without having to change the existing RFQ or IH-DTL. An efficient IH-type linac design was developed in this work as an option to replace the aging poststripper

DTL. Replacing the existing poststripper linac by this IH-DTL option instead of a redesigned Alvarez DTL will reduce the costs of the replacement by at least 35 %. Additionally, it will leave a lot of spare room in the UNILAC tunnel for future upgrades of the UNILAC and FAIR. A possible future energy upgrade of the UNILAC could reach about 50 $\frac{\mathrm{MeV}}{\mathrm{u}}$ for U^{28+} ions, using 324 MHz CH-type cavities within the available space. Such high gradient CH-type cavities are currently being developed at IAP Frankfurt [49, 22]. Moreover, due to the much smaller diameter of the proposed poststripper cavities, additional space will also be available alongside the poststripper IH-DTL. This can be used to house a superconducting cw linac for the continuation of experiments like the production of new super-heavy elements and material research [50, 51] at GSI.

9 Acknowledgments

I want to thank all colleagues at the Institute of Applied Physics that have supported me and my work during my doctoral studies (including those not explicitly mentioned).
I especially want to express my gratitude to my advisor Prof. Dr. Ulrich Ratzinger for his support during my thesis. He is always available for discussions and happy to share his invaluable knowledge in linac development from beam dynamics to the actual machine. Also, I want to thank Prof. Dr. Joachim Jacoby for being second examiner of my thesis.
For the fruitful discussions, I want to thank Dr. Rudolf Tiede. The discussions on beam dynamics, his help with the LORASR code, as well as his private and career advice were and continue to be very helpful.
I also want to thank Dr. Ali Almomani for his advice and helpful discussions.
I want to thank my brother Joshua for his support by meticulously proofreading my thesis and providing an outside perspective (still a physicist, but not in linacs). I also want to thank my parents for supporting me during my studies, financially and emotionally.
Finally I want to thank my wife Julia who has literally gone through the good and the bad times with me and has always supported me in my pursuit of a scientific career.

Bibliography

[1] "FAIR Baseline Technical Report Vol. 2," GSI Darmstadt, Tech. Rep., 2006.

[2] A. Kolomiets, S. Minaev, W. Barth, L. Dahl, H. Vormann, and S. Yaramyshev, "Upgrade of the UNILAC High Current Injector RFQ," in *Proceedings of LINAC2008*, Victoria, BC, Canada, 2008, pp. 136–138.

[3] U. Ratzinger and R. Tiede, "A New Matcher Type Between RFQ and IH-DTL for the GSI High Current Heavy Ion Prestripper Linac," in *Proceedings of LINAC1996*, Geneva, Switzerland, 1996, pp. 128–130.

[4] H. Hähnel, U. Ratzinger, and R. Tiede, "Proposal of a Conventional Matching Section as an Alternative to the Current Superlens at GSI UNILAC," in *Proceedings of LINAC2014*, Geneva, Switzerland, 2014, pp. 196–198.

[5] ——, "Efficient Heavy Ion Acceleration with IH-Type Cavities for High Current Machines in the Energy Range up to 11.4 MeV/u," in *Proceedings of LINAC2016*, East Lansing, MI, USA, 2016.

[6] U. Ratzinger, E. Nolte, R. Geier, N. Gärtner, and H. Morinaga, "The Upgraded Munich Linear Heavy Ion Postaccelerator," *Nuclear Instruments and Methods in Physics Research A*, vol. 263, pp. 261–270, 1988.

[7] U. Ratzinger, "The IH-Structure and its Capability to Accelerate High Current Beams," in *Proceedings of PAC1991*, San Francisco, CA, USA, 1991, pp. 567–571.

[8] B. Schlitt, G. Eichler, S. Hermann, M. Hoerr, M. Mueh, S. Petit, A. Schnase, G. Schreiber, W. Vinzenz, and J. Zappai, "Modernisation of the 108 MHz RF Systems at the GSI UNILAC," in *Proceedings of LINAC2016*, East Lansing, MI, USA, 2016.

[9] T. P. Wangler, *RF Linear Accelerators*. Wiley-VCH, 2008.

[10] P. D. M. Reiser, *Theory and Design of Charge Particle Beams*. Wiley-VCH, 2008.

[11] R. Wideröe, "Über ein neues Prinzip zur Herstellung hoher Spannungen," *Archiv f. Elektrotechnik*, vol. 21, no. 4, pp. 387–406, 1928.

[12] L. Alvarez, *Physical Review*, vol. 70, no. 799, 1946.

[13] L. W. Alvarez, H. Bradner, J. V. Franck, H. Gordon, J. D. Gow, L. C. Marshall, F. Oppenheimer, W. K. H. Panofsky, C. Richman, and J. R. Woodyard, "Berkeley Proton Linear Accelerator," *Review of Scientific Instruments*, vol. 26, no. 2, pp. 111–133, 1955.

[14] L. Smith and R. L. Gluckstern, "Focusing in Linear Ion Accelerators," *Review of Scientific Instruments*, vol. 26, no. 2, pp. 220–228, 1955.

[15] E. Nolte, G. Geschonke, K. Berdermann, R. Oberschmid, R. Zierl, M. Fell, A. Jahnke, M. Kress, and H. Morinaga, "The Munich Heavy Ion Postaccelerator," *Nuclear Instruments and Methods*, vol. 158, pp. 311–324, 1978.

[16] E. Nolte, R. Geier, W. Schollmeier, and S. Gustavson, "Improved Performance of the Munich Heavy Ion Postaccelerator," *Nuclear Instruments and Methods*, vol. 201, pp. 281–285, 1982.

[17] U. Ratzinger, "The new High Current Ion Accelerator at GSI and Perspectives for Linac Design Based on H-Mode Cavities," in *Proceedings of EPAC2000*, Vienna, Austria, 2000, pp. 98–102.

[18] ——, *Effiziente Hochfrequenz-Linearbeschleuniger für leichte und schwere Ionen*, Habilitation thesis, Goethe University, Frankfurt, 1998.

[19] Y. Lu, "Development of an IH-DTL Injector for the Heidelberg Cancer Therapy Project," Ph.D. dissertation, Goethe University, Frankfurt, 2005.

[20] U. Ratzinger, K. Kaspar, E. Malwitz, S. Minaev, and R. Tiede, "The GSI 36 MHz High-Current IH-Type RFQ and HIIF-Relevant Extensions," *Nuclear Instruments and Methods in Physics Research A*, vol. 415, pp. 281–286, 1998.

[21] R. Tiede, "Simulationswerkzeuge für die Berechnung hochintensiver Ionenbeschleuniger," Ph.D. dissertation, Goethe University Frankfurt, 2009.

[22] A. M. Almomani and U. Ratzinger, "Status and First Measurement Results for a High Gradient CH-Cavity," in *Proceedings of IPAC2015*, Richmond, VA, USA, 2015, pp. 3724–3726.

[23] R. Tiede, D. Mäder, N. Petry, H. Podlech, U. Ratzinger, and C. Zhang, "Improvements of the LORASR Code and their Impact on Current Beam Dynamics Designs," in *Proceedings of LINAC2014*, Geneva, Switzerland, 2014, pp. 569–571.

[24] I. M. Kapchinskij and V. V. Vladimirskij, "Limitations of Proton Beam Current in a Strong Focusing Linear Accelerator Associated with the Beam Space Charge," in *Proceedings of the International Conference on High Energy Accelerators and Instrumentation*, Geneva, Switzerland, 1959, pp. 274–288.

[25] G. Parisi, "Investigations on Particle Dynamics in a High Intensity Heavy Ion Linac for Inertial Fusion," Ph.D. dissertation, Goethe University, Frankfurt, 1999.

[26] A. Lombardi, E. Sargsyan, S. Lanzone, J.-b. Lallement, G. Bellodi, M. Baylac, R. Duperrier, and D. Uriot, "End-to-End Beam Dynamics for Cern Linac4," in *Proceedings of HB2006*, Tsukuba, Japan, 2006, pp. 79–83.

[27] U. Ratzinger and R. Tiede, "Teilchendynamische Untersuchungen an einer Kombinierten Null Grad Struktur KONUS mit Quadrupoltriplett-Fokussierung," GSI Darmstadt, Tech. Rep. ALG10077SI, 1997.

[28] S. Minaev, U. Ratzinger, and B. Schlitt, "APF or KONUS Drift Tube Structures for Medical Synchrotron Injectors - A Comparison," in *Proceedings of PAC1999*, New York, USA, 1999, pp. 3555–3557.

[29] M. Schwarz, M. Amberg, K. Aulenbacher, W. Barth, M. Basten, F. Dziuba, V. Gettmann, M. Heilmann, S. Mickat, A. Orzhekhovskaya, H. Podlech, U. Ratzinger, R. Tiede, and S. Yaramyshev, "Beam Dynamics for the SC CW Heavy Ion Linac at GSI," in *Proceedings of IPAC2015*, Richmond, VA, USA, 2015, pp. 3742–3744.

[30] S. Minaev, U. Ratzinger, H. Podlech, M. Busch, and W. Barth, "Superconducting, Energy Variable Heavy Ion Linac with Constant Beta, Multicell Cavities

of CH-Type," *Physical Review Special Topics - Accelerators and Beams*, vol. 12, no. 12, 2009.

[31] U. Ratzinger, "The New GSI Prestripper Linac for High Current Heavy Ion Beams," in *Proceedings of LINAC1996*, Geneva, Switzerland, 1996, pp. 288–292.

[32] R. Tiede, A. Almomani, M. Busch, F. Dziuba, and U. Ratzinger, "Improved Beam Dynamics and Cavity RF Design for the FAIR Proton Injector," in *Proceedings of LINAC2016*, East Lansing, MI, USA, 2016.

[33] U. Ratzinger, "Commissioning of the new GSI High Current Linac and HIF Related RF Linac Aspects," *Nuclear Instruments and Methods in Physics Research A*, vol. 464, no. 1-3, pp. 636–645, may 2001.

[34] W. Barth and P. Forck, "The New Gas Stripper and Charge State Separator of the GSI High Current Injector," in *Proceedings of LINAC2000*, Monterey, CA, USA, 2000, pp. 235–237.

[35] O. Kester, P. Spiller, F. Becker, O. Dolinskyy, L. Groening, K. Knie, H. Reich-Sprenger, W. Vinzenz, M. Winkler, and D. Prasuhn, "The Accelerator Facility of the Facility for Antiproton and Ion Research," in *Proceedings of IPAC2016*, Richmond, VA, USA, 2015, pp. 1343–1345.

[36] Y. El-Hayek, "Minimierung der Systematischen Anfangsverluste im SIS18," Ph.D. dissertation, Goethe University, Frankfurt, 2013.

[37] W. Barth, A. Adonin, C. E. Düllmann, M. Heilmann, R. Hollinger, E. Jäger, J. Khuyagbaatar, J. Krier, P. Scharrer, H. Vormann, and A. Yakushev, "U^{28+}-Intensity Record Applying a H_2-Gas Stripper Cell," *Physical Review Special Topics - Accelerators and Beams*, vol. 18, no. 4, pp. 1–9, 2015.

[38] A. Schempp, "Design of Compact RFQs," in *Proceedings of LINAC1996*, Geneva, Switzerland, 1996, pp. 53–55.

[39] R. Tiede, G. Clemente, H. Podlech, U. Ratzinger, A. Sauer, and S. Minaev, "Lorasr Code Development," in *Proceedings of EPAC2006*, Edinburgh, Scotland, 2006, pp. 2194–2196.

[40] R. Tiede, "HSI IH-DTL Acceptance Studies," in *Talk at UNILAC Upgrade Meeting*, January 2014.

[41] S. Mickat, "Refurbishment of the Existing Alvarez," in *Talk at Expert Review on the Alvarez Replacement*, October 2016.

[42] B. Schlitt, M. Hoerr, A. Schnase, G. Schreiber, and W. Vinzenz, "RF System Development for the new 108 MHz Heavy Ion High-Energy Linac at GSI," in *Proceedings of LINAC2014*, Geneva, Switzerland, 2014, pp. 556–558.

[43] J. Klabunde, "The High Charge State Injector for GSI," in *Proceedings of LINAC1992*, Ottawa, ON, Canada, 1992, pp. 570–574.

[44] A. Butenko, A. Kovalenko, H. Hoeltermann, H. Podlech, U. Ratzinger, A. Schempp, D. Liakin, B. V. Golovenskiy, V. Kobets, V. Monchinsky, D. E. Donets, K. Levterov, D. Lyuosev, and G. Trubnikov, "Commissioning of the New Heavy Ion Linac at the NICA Project," in *Proceedings of IPAC2017*, Copenhagen, Denmark, 2017.

[45] M. Droba, O. Meusel, and U. Ratzinger, "Simulation Study of Emittance Growth from Coulomb Explosion in a Charge Separator System after Stripping," in *Proceedings of IPAC2016*, Busan, Korea, 2016.

[46] Y. El-Hayek, U. Ratzinger, P. Spiller, D. Ondreka, M. Kirk, Y. E. Hayek, U. Ratzinger, P. Spiller, D. Ondreka, and M. Kirk, "Initial Beam Loss and Control of Dynamic Vacuum Effects in SIS18," in *Proceedings of IPAC2013*, Shanghai, China, 2013, pp. 300–302.

[47] N. Pichoff, J. M. Lagniel, and S. Nath, "Simulation Results with an Alternate 3D Space Charge Routine, PICNIC," in *Proceedings of LINAC1998*, Chicago, USA, 1998, pp. 141–143.

[48] M. Eshraqi, R. Miyamoto, E. Sargsyan, R. D. Prisco, and H. D. Thomsen, "Statistical Error Studies in the ESS Linac," in *Proceedings of IPAC2014*, Dresden, Germany, 2014, pp. 3323–3325.

[49] A. Almomani and U. Ratzinger, "A 325 MHz High Gradient CH-Test Cavity for $\beta = 0.16$," in *Proceedings of IPAC2014*, Dresden, Germany, 2014, pp. 3229–3231.

[50] F. Dziuba, M. Amberg, K. Aulenbacher, W. Barth, M. Basten, M. Busch, V. Gettmann, M. Heilmann, S. Mickat, H. Podlech, M. Schwarz, and S. Yaramyshev, "First Cold Test of the Superconducting CW Demonstrator at GSI," in *Proceedings of RuPAC2016*, St. Petersburg, Russia, 2016, pp. 83–85.

[51] M. Schwarz, M. Basten, M. Busch, F. Dziuba, H. Podlech, U. Ratzinger, R. Tiede, W. Barth, V. Gettmann, M. Heilmann, S. Mickat, and S. Yaramyshev, "Further Steps Towards the Superconducting CW-Linac for Heavy Ions at GSI," in *Proceedings of IPAC2016*, Busan, Korea, 2016.

List of Figures

List of Tables